Dense Colloidal Suspensions in Microchannel Flow

vorgelegt von
Master of Science

Philipp Kanehl

geboren in Stralsund

Von der Fakultät II - Mathematik und Naturwissenschaften
der Technischen Universität Berlin
zur Erlangung des akademischen Grades
Doktor der Naturwissenschaften (Dr. rer. nat.)

genehmigte Dissertation

Promotionsausschuss:

Vorsitzender:	Prof. Dr. Martin Schoen
Erster Gutachter:	Prof. Dr. Holger Stark
Zweiter Gutachter:	Prof. Dr. Roland Netz

Tag der wissenschaftlichen Aussprache: 7. Februar 2017

Berlin 2017

Zusammenfassung

Kolloidale Suspensionen im Scherrfluss migrieren in Richtung kleiner Scherrate. Suspensionen mit zwei verschiedenen Teilchengrößen entmischen sich im Zentrum eines Mikrokanals. Kolloide in Kanälen mit sehr hoher Packungsdichte können Staus bilden welche reguläre Oszillationen in der Flussgeschwindigkeit auslösen. Diese Geschwindigkeitsoszillationen werden von Verdünnungswellen in der Packungsdichte begleitet. Wird die Dichte noch weiter erhöht, treten die Oszillationen unregelmäßig auf.

Um ein theoretischen Verständniss dieser Effekte zu vertiefen, simulieren wir Kugeln im Fluss eines Kanals in zwei und drei Dimensionen. Dabei verwenden wir die mesosokopische Simulationsmethode der Vielteilchen-Stoßdynamik für die Modellierung der Flüssigkeit.

Um die hydrodynamische Segregation zu modellieren, formulieren wir eine phenomenologisches Model für den lateralen Teilchenfluß auf Basis der Arbeit von J. Phillips *et al.* [Phys. Fluids **4**, 30 (1992)]. Die neu formulierte Theorie trifft gute Vorhersagen für die simulierte Dichteverteilung entlang des Kanalquerschnitts. Wir präsentieren eine ausführliche Parameterstudie wie Suspensionen einer Teilchengröße sich in der Kanalmitte anreichern und Suspensionen zweier Teilchengrößen sich entmischen. Dabei finden wir stets eine stärkere Anreicherung der großen Teilchen im Zentrum.

Für die Simulation noch dichterer Systeme benutzen wir ein elastisches Kontaktmodell mit Reibung für die Kolloide. Mit deisem Modell ist es möglich die periodischen Geschwindigkeits- und Dichtepulse zu simulieren welche auch in den Experimenten von L. Isa *et al.* [Phys. Rev. Lett. **102**, 058302 (2009)] beobachtet wurden. Wir zeigen dass die Reibung zwischen Kolloiden und den Kanalwänden ein notwendiges Kriterium für die Formation der Pulse ist. Mit ansteigender Packungsdichte formieren sich die Pulse zuerst als einzelne Staus, welche bei höherer Dichte die Form eines periodischen Pulszuges annehmen. Bei der höhsten Packungsdichte findet man vereinzelte instabile Pulse. Wir formulieren ein neues phenomenologisches Kontinuummodell und zeigen dass die laufenden Pulse als periodische und homokline Orbits in den zugehörigen Differentialgleichungen verstanden werden können.

Abstract

Colloids in suspensions exhibit shear-induced migration towards regions of low viscous shear. In bidisperse suspensions under pressure driven flow large particles can segregate in the center of a microchannel and the suspension partially demixes. In channels containing very dense suspensions, colloids may jam and produce regular flow speed oscillations generated by density rarefaction waves. Increasing the density even further the oscillations become irregular.

To develop a theoretical understanding of these effects, we simulate spheres under pressure-driven channel flow in two and three dimensions using the mesoscale simulation technique of multi-particle collision dynamics.

To model hydrodynamic segregation, we formulate a phenomenological model for the particle currents based on the work of R. J. Phillips *et al.* [Phys. Fluids **4**, 30 (1992)]. Using a single fit parameter for the intrinsic diffusivity, our theory accurately reproduces the simulated density profiles across the channel. We present a detailed parameter study on how a monodisperse suspension is enriched in the channel center and quantitatively confirm the experimental observation that a binary mixture partially segregates into its two species. In particular, we always find a strong accumulation of large particles in the center.

For our simulations on jamming, the colloids are modeled as elastic and frictional disks. The model reproduces periodic velocity and density pulse trains, traveling upstream in the microchannel, which are found in experiments conducted by L. Isa *et al.* [Phys. Rev. Lett. **102**, 058302 (2009)]. We show that colloid-wall friction and the resultant force chains are crucial for the formation of these pulses. With increasing colloid density solitary jams occur, which become periodic pulse trains at intermediate densities and unstable solitary pulses at high densities. We formulate a phenomenological continuum model and show how these spatio-temporal flow and density profiles can be understood as homoclinic and periodic orbits in traveling-wave equations.

Danksagung

Es ist mir ein wichtiges Verlangen die Menschen hervorzuheben ohne die diese Arbeit nicht möglich gewesen wäre.

An erster Stelle gebührt mein Dank meinem Doktorvater Prof. Dr. Holger Stark, der mir diese Promotion ermöglicht hat. Er gab mir stets die Freiheit meine Ideen zu verwirklichen und stand mir mit konstruktiven Rat zur Seite. Die Gespräche und Kritiken stellen einen wertvollen Beitrag dieser Arbeit dar.

Mein besonderer Dank richtet sich auch an die ganze Arbeitsgruppe der AG Stark. Hervorheben möchte ich insbesondere Christopher Prohm und Maria Zeitz welche mir entweder mit Expertise oder tatkräftiger Unterstützung unter die Arme gegriffen haben. Außerdem bedanke ich mich bei Jan-Timm Kuhr, Felix Rühle, Shahajhan Sorathiya, Matthew Dennison, Peter Kalle, Josua Grawitter und Maximilian Seyrich, die mir beim Korrekturlesen geholfen haben.

Mein Dank gebührt auch der Deutsche Forschungsgemeinschaft, welche mich im Rahmen des Graduiertenkollegs GRK 1558 finanziell unterstützt hat.

Zu guter Letzt möchte ich mich bei meiner Familie bedanken, die mich immer gestützt hat und mir motivierend beiseite stand.

List of Publications

[A] P. Kanehl and H. Stark, *Hydrodynamic Segregation in a Bidisperse Colloidal Suspension in Microchannel Flow: A Theoretical Study*, J. Chem. Phys. **142**, 214901 (2015).

[B] P. Kanehl and H. Stark, *Self-Organized Velocity Pulses of Dense Colloidal Suspensions in Microchannel Flow*, arXiv preprint arXiv:1611.02773 (2016).

Contents

1 Introduction

Colloidal suspensions have gained widespread attention from about the 1970s for their rich static and dynamic properties as well as their role in commonplace objects like paints, cosmetics, detergents, food, and fuel [1–5]. Understanding the collective dynamics of colloids in viscous fluids is an ongoing challenge [6–12]. The complexity of collective phenomena contrasts with the simplicity of low-Reynolds-number flow, which is governed by the linear Stokes equation [13]. Dense colloidal suspensions in microfluidic flow pose fundamental questions about the interplay between confinement, structure, and flow behavior. In particular, the role of jamming and dynamical heterogeneities has come into focus [14, 15].

Research has shown that in moderately dense suspensions particle migrate towards regions of low shear rate. This migration finds applications in several industrial processes such as microfiltration [16], fluidized beds, and fractionation of particle suspensions [17]. After some initial work by Eckstein *et al.* [18] quantifying shear-induced diffusion, Leighton and Acrivos [19] described shear-induced migration. Leighton wanted to explain the unexpected decrease of shear viscosity of a colloidal suspension in a Couette cell [20]. He found that the polystyrene spheres migrated out of the high-shear region between the rotating cylinders. Since this work, shear-induced migration was reported in several experimental setups. Examples include circular Couette flow [21, 22], pressure driven Poiseuille flow between parallel plates [23], as well as microchannels, where the particles segregate in the center [24–27].

At small Reynolds numbers, such a segregation cannot be explained by pure hydrodynamic forces due to the kinematic reversibility of the governing Stokes equations. According to this symmetry, reversal of time should reverse the segregation towards, for example, a uniform initial state. However, also the direction of Poiseuille flow is simply reversed with time and both the original and time-reversed system should behave the same. Only physical features, which are not included in the Stokes equations, such as direct particle-particle contacts, thermal motion, or residual inertia [28–30] can break the kinematic reversibility and induce cross-streamline migration in dense suspensions.

Another branch of phenomena occurring in suspensions near random close packing density stems from particle jamming. Here, the colloidal flow in confinement is arrested due to the self-organized formation of force chains [31]. The colloidal system thus becomes solid, although fragile with respect to small perturbations. Since jamming occurs in such diverse systems as granular matter [32], pedestrian and traffic flow [33–

35], and very prominently, during shear thickening of corn starch [36, 37], Liu and Nagel [38] suggested it as a universal principle governing dense particle systems.

It is well known that hydrodynamic lubrication prevents direct contact during collisions of micron-sized colloids suspended in a viscous fluid [39]. However, over the past years research has found cues for the necessity of direct particle contacts to explain phenomena such as shear migration, discontinuous shear thickening [40, 41], and jamming [6]. For example, numerical studies by Seto *et al.* [42] and work by Heussinger [43] and Fernandez *et al.* [41] stressed the importance of implementing contact friction to successfully model discontinuous shear thickening.

Recent research showed that pressure driven flow of dense colloidal suspensions through microchannels produces regular [44] and irregular [45] oscillations in flow speed, that can be attributed to the formation of transient jams. Furthermore, Isa *et al.* [44] could indirectly verify the existence of rarefaction pulses traveling upstream and stressed the importance of shear thickening under confinement for explaining this observation [36].

The aim of this thesis is to obtain further insight into the underlying principles governing shear-induced segregation and colloidal jamming, in particular, in bidisperse suspensions under pressure-driven flow through a microchannel. With simulations, we first want to be able to capture and study the experimentally observed phenomena for a wide range of parameters. Secondly, by reducing the complex interplay of hydrodynamics, thermal motion and contact networks to key mechanisms, we propose or modify equations which produce the same phenomena to deepen our understanding further. Using simulation we have the significant advantage of fine-tuning every parameter individually and measuring quantities from our data directly. To accomplish this, the method of multi-particle collision dynamics (MPCD) is employed to solve the Navier-Stokes equation [46, 47]. MPCD is computationally fast, simple to implement, and capable of reproducing analytically known results [48–50]. MPCD has been successfully used to tackle diverse problems in soft matter physics [51, 52]. Recent examples are the collective dynamics of squirmers [53], a detailed modeling of the swimming mechanism of the African trypanosome [54], diffusion of star polymers [55], and the sedimentation of a red blood cell [56]. To simulate fluid flow, MPCD uses a sequence of streaming and collision steps of point-like effective fluid particles. In the streaming step the particles move forward ballistically. In the collision step the particles are grouped into cubic cells. All fluid particles within the same cell collide according to a specific collision rule keeping the mean velocity constant in order to conserve momentum. This procedure is sufficient to create a fluid flow field that solves the Navier-Stokes equations. In addition, thermal noise is incorporated due to the stochastic character of MPCD.

This thesis is organized as follows: Chapter 2 gives an overview on historical and recent research on colloidal particles in flow and highlights key insights. Some articles are presented in more detail, which had a great impact on this work for either encouraging simulations or suggesting analytical models.

In chapter 3 we present the physical foundations starting with the hydrodynamic equations of motion, followed by basic principles of the statistical physics of passive Brownian particles and kinetic gas theory of a canonical ensemble. The chapter concludes with an introduction to nonlinear dynamics and bifurcation theory.

Subsequently, in chapter 4 we outline the numerical method of multi-particle collision dynamics together with details on its implementation. Moreover, we introduce and motivate two methods for implementing the contact interactions between colloidal particles. The first uses event-driven molecular dynamics to resolve collisions between hard spheres instantaneously. The second generates repelling forces from linear springs

in normal and tangential direction to the contacts that obey Coulomb's law of friction".

In chapter 5 we present the results on shear induced size segregation in microchannels. On the one hand, we extend the phenomenological model of Phillips *et al.* [57] to bidisperse suspensions using scaling arguments for the involved particle radii and also formulate a more realistic expression for the collective diffusion tensor. On the other hand, we employ MPCD to efficiently solve the governing Navier-Stokes equations. We show results of our extensive two-dimensional simulations of pressure-driven colloidal flow in microchannels. By varying total area fraction, packing composition, and flow speed, we confirm the segregation of large particles in the channel center. A single fit parameter for the diffusivities is sufficient to obtain an accurate agreement between the simulated density profiles and the profiles from the phenomenological model. Three-dimensional simulations with hard spheres reveal only minor differences compared to two spatial dimensions. Simulations and the phenomenological model equations reproduce fine details in the experimental profiles of Ref. [58].

In chapter 6 we combine MPCD with a frictional contact model for particles [59], in order to thoroughly study jamming of dense colloidal suspensions in microchannels in two dimensions. With increasing colloid density, we identify solitary jams, regular pulse trains, and solitary pulses in the colloidal flow similar to experimental observations [44, 45]. We stress the importance of colloid-wall friction and the formation of force chains for inducing a transition between free and jammed flow. This is the origin for traveling rarefaction pulses to occur. A newly formulated nonlinear continuum model reproduces the flow instabilities from our simulation study.

Finally, in chapter 7 we summarize the results and give an outlook.

2 Review of the State of the Art

From the first experiments conducted on colloidal gold suspensions by Michael Faraday in 1857 [60] to the present day there have been several findings that have affected our understanding of how colloidal particles move and interact. As in all disciplines of physics, sometimes all it takes is an inexplicable experiment for new models to thrive, capable of explaining the new phenomenon. The objective of this chapter is to place the results of this thesis into the context with historical and recent experiments and their conclusions. We start by outlining the characteristics of colloidal particles in flow, which will be discussed in more depth and mathematically derived in chapter 3. We close by presenting some of the most important experimental and theoretical works in the field of dense colloidal suspensions. All of these deserve great credit in the creation of this thesis for either motivating simulations or inspiring analytical modeling.

2.1 Colloids: Physics on Small Length Scales

The name "colloid" comes from Greek and is composed of $\kappa\acute{o}\lambda\lambda\alpha$, kólla, "glue" and $\epsilon\tilde{\imath}\delta o\varsigma$, eidos, "look". All particles which bear the name share one common feature: they are very small. More specifically, their radii range from a few micro meters (10^{-6}m) down to a few nano meters (10^{-9}m). Furthermore, colloids are usually dispersed in a fluid. The fluid is composed of molecules, which are thermally driven, i.e. each molecule has an undirected movement with a mean kinetic energy proportional to $k_\mathrm{B}T$, where k_B denotes the Boltzmann constant and T the absolute temperature. The molecules erratically collide with the particle which is a few orders of magnitude larger than a molecule. These momentum exchanges become visible under a microscope as diffusive motion (Brownian motion) of the colloid and contributed to proving the molecular character of matter in 1905 by Albert Einstein [61].

The time scale τ_D for a colloid to diffuse the distance of its own radius is typically around $\tau_D \approx 10^0 - 10^1$s. In research this time scale is commonly compared to the convective time scale τ_v, i.e. the time required for the colloid to travel the distance of its own radius due to external flow. The ratio of both time scales is named Péclet number and defined as

$$\mathrm{Pe} = \frac{\tau_D}{\tau_v} = \frac{va}{D}, \tag{2.1}$$

where v is the flow speed, a the colloidal radius and D the diffusion constant. The Péclet number is an important dimensionless number characterizing flows in non-equilibrium.

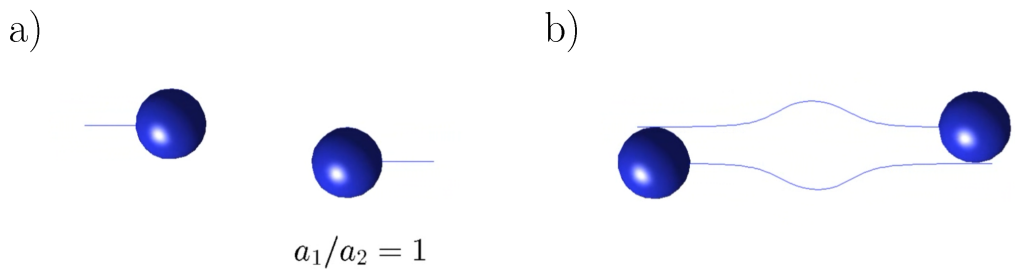

Figure 2.1: Trajectories of two spheres with radii $a_1 = a_2$ in unbounded shear flow calculated with the aid of Stokes equation before interaction a) and after interaction b).

Small Péclet numbers, $\mathrm{Pe} \ll 1$, correspond to flows where the transport is dominated by diffusion whereas flows at $\mathrm{Pe} \gg 1$ are dominated by convection. A more detailed and quantitative description of Brownian motion based on Einstein's theory follows in chapter 3.

The micro size of the colloids has yet another consequence because the corresponding Reynolds numbers are vanishingly small. The Reynolds number is a dimensionless number that determines the ratio of inertial forces to viscous forces in the fluid. It is defined by

$$\mathrm{Re} = \frac{va}{\nu}, \tag{2.2}$$

where again v is the flow speed, a a characteristic length scale, and ν the kinematic viscosity of the fluid.

For a colloidal particle dragged through water with a speed of $v = 10\mu\mathrm{ms}^{-1}$, the characteristic size a is the colloidal radius which ranges between 10^{-9} and 10^{-6}m. The kinematic viscosity of water at room temperature is $\nu \approx 1 \times 10^{-6}\mathrm{m}^2\mathrm{s}^{-1}$. With help of Eq. (2.2) we can calculate a Reynolds number of $\mathrm{Re} \approx 10^{-8} - 10^{-5}$. This has tremendous consequences for the swimming behavior of the colloid as inertia becomes insignificant. Whereas a submarine ($\mathrm{Re} \approx 10000000$) would continue to move under water for a long time after its engines had stopped, a colloidal particle would immediately be arrested by the viscous friction of the fluid. In other words, colloidal particles respond instantaneously to changes in flow. A mathematical implication of this is that a reversal of flow is equivalent with a reversal of time as pointed out by Stokes in 1851 [62].

The same is true for hydrodynamic interactions between colloidal particles. Two colloids in shear flow will be displaced by each other orthogonal to the flow as the stream lines get distorted by their own flow field, but they will return to the lateral position before the encounter as they gain distance, see Fig. 2.1. When the initial lateral distance in a setup like that in Fig. 2.1 is decreased, the colloids can come very close to each other when they pass. In 1973, Hocking [63] found that in the limit of the Stokes equation, which describes the flow at vanishing Reynolds numbers (see chapter 3), the lubrication force between two spheres or between a sphere and a wall is inversely proportional to the gap. Consequently, from a mathematical point of view it is impossible for a finite force to produce a physical contact. However, it needs to be stressed that the Stokes equation holds true only on length scales significantly larger than the fluid molecules.

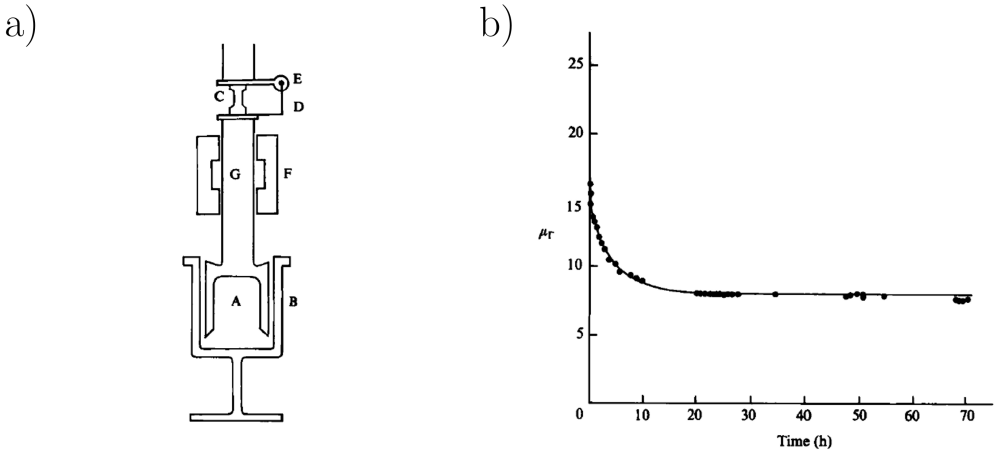

Figure 2.2: a) Schematic diagram of the R-17 Weissenberg Rheogoniometer torsion measurement apparatus. A: bob, B: cup, C: torsion bar, D: torsion arm, E: transducer, F: air bearing, G: torsion shaft. b) Relative viscosity of a suspension with $\phi = 0.45$ as a function of time. Polystyrene spheres, 40-50 μm in diameter in a mixture of silicone oils. Reprinted with permission from F. Gadala Maria and A. Acrivos [J. Rheol. **24**, 799 (1980)]. Copyright (1980), The Society of Rheology.

2.2 Shear-induced Cross-streamline Migration

Given the insights of lubrication and reversibility, until the beginning of the 1980's it was believed that colloids would not physically touch in a suspension and would not leave their streamlines except through thermal fluctuations. However, in the course of viscometric measurements of concentrated suspensions of colloids in Newtonian fluids using a Couette device, Gadala-Maria and his colleague Acrivos made a strange discovery [20]. Their observation was later linked to an underlying principle that violated the former belief of reversibility.

2.2.1 The Couette-flow dilemma

A Couette viscometer displayed in Fig. 2.2 a) shears a sample fluid in the gap between two cylinders by rotating the inner cylinder with a constant torque. The viscosity is then determined from the linear relation between applied torque and angular speed of the cylinder.

In 1980 Gadala-Maria and Acrivos reported the puzzling observation that, at very high colloidal volume fractions $\phi > 0.40$, the effective viscosity μ of the suspensions decreased slowly with prolonged shearing and eventually reached a steady-state value, which then remained constant as displayed in Fig. 2.2 b). The relative magnitude of this decrease was quite significant and strongly depends on the overall volume fraction ϕ of the colloidal particles. This phenomenon could easily be reproduced but was not reversible upon inverting the direction of rotation. The colloids were sufficiently large such that Brownian or electroviscous forces should not play a significant role. In their paper, Leighton and Acrivos [64] were able to reproduce the viscosity decrease and argued that the particles had migrated out of the gap into the reservoir, thus decreasing the packing fraction $\overline{\phi}$ inside the gap and therefore the effective viscosity. Gravity as a cause for the migration could be excluded because the particles were density matched with the fluid. Because inertial effects were insignificant due to a Reynolds number

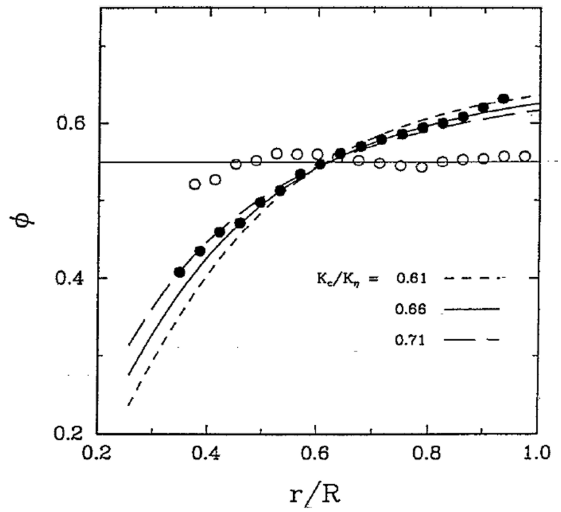

Figure 2.3: Initial (empty circles) versus steady-state (filled circles) density profile of suspension of 615 μm particles at a volume fraction of $\phi = 0.55$ in Couette flow. The lines correspond to steady-state solutions of the phenomenological theory for various fitting values K_c/K_η. Reprinted from R. J. Phillips *et al.* [Phys. Fluids **4**, 30 (1992)], with the permission of AIP Publishing.

of roughly Re $\approx 10^{-4}$, they concluded that the migration occurred due to a so far unknown mechanism. They developed an idea about the need for irreversible binary particle interactions to model shear migration. The frequency of interactions in a sheared suspension scales with $\propto \dot{\gamma}\phi$, where $\dot{\gamma}$ denotes the shear rate. They argued that each interaction leads to a permanent displacement orthogonal to the flow and proportional to the size a of the colliding particles. As a result, the suspension experiences a net migration velocity v_{mig} given by

$$v_{\text{mig}} \propto -a^2 \nabla |\dot{\gamma}| \phi, \tag{2.3}$$

with ∇ the gradient operator. Eq. (2.3) predicts a migration towards areas of low shear rate, which agrees with the experimental finding of particles migrating away from the sheared fluid between the cylinders into the quiescent reservoir.

The fact that colloidal interactions were leading to cross-streamline migration in dense suspensions contradicted the principle of reversibility in Stokes flow. Experimentalists looked for an answer and finally concluded that colloidal surface roughness could lead to physical contacts between particles in sheared dense suspensions [65, 66]. A recent experiment by Pine *et al.* [67] directly demonstrated the violation of kinematic reversibility for a particle suspension in an oscillating Couette device above a threshold value for density and amplitude.

2.2.2 Modeling of shear migration

Since the work of Leighton and Acrivos [64], shear-induced migration was reported in several experimental setups using stiff particles for instance in circular Couette flow [21, 22], and in pressure driven Poiseuille flow between parallel plates [23] as well as in microchannels, where the particles enrich the center [24–27]. In addition, deformable objects such as a semiflexible polymers [68–71], emulsion droplets [72, 73], and red blood cells [74–76] show cross-streamline migration.

Mainly two theoretical approaches have been used to describe particle migration towards regions of lower shear rate in monodisperse suspensions. Based on the ideas of Leighton and Acrivos [19], Phillips *et al.* formulated a phenomenological theory for the lateral particle current [22]. They compared their experimental data of particle migration in Couette flow to the predictions of their theory depending on fitting parameters K_c and K_η, shown in Fig. 2.3, and obtained good agreement. Later, the theory was complemented by a migration flux due to curvature in flow geometry [77]. More recently, it was applied to suspensions of Brownian particles [78].

The second approach, the suspension balance model, derives the lateral particle current from the continuity equations for mass and momentum averaged over the volume just occupied by the particle phase [79, 80]. This model was later refined to account for Brownian motion [25], to treat more complex channel geometries, and it is extensively studied in Ref. [81]. However, in a recent publication, Nott *et al.* [82] confirm an earlier conclusion of Lhuillier [83] that the suspension balance model does not properly distinguish between hydrodynamic and non-hydrodynamic stresses.

2.2.3 Size segregation in channel flow

Using a binary suspension, Husband *et al.* [84] were the first to note that in an initially well-mixed suspension larger particles migrate faster than the smaller ones, ultimately leading to size segregation. In Ref. [58], Semwogerere and Weeks presented a careful study of a binary mixture of 1.4 and 3.0μm Brownian particles in a pressure driven flow. Since Brownian motion limits the inhomogeneity of the fully developed concentration profiles they used flow speeds that correspond to a Péclet number of roughly Pe ≈ 100. The recorded concentration profiles confirmed that at equal volume fractions the larger species enriches the center, whereas the smaller species shows slight depletion. However, this effect reverses when the smaller species is in the majority with a volume fraction larger by a factor 2.5, as displayed in Fig. 2.4.

The very few theoretical approaches describing particle segregation in sheared binary suspensions adapt the models described above. However, they neglect or simplify how the smaller species effects the larger one [85, 86]. Shauly *et al.* [87] generalized the model of Phillips *et al.* to treat polydisperse suspensions. They used a simplified coupling between different particle species and included curvature in the flow geometry but neglected thermal diffusion. In contrast to the scope of this thesis, the authors focused on particle segregation in Couette flow. A very recent model uses a multi-fluid approach and introduces an effective temperature for the particle's osmotic pressure, which depends on the shear rate [88].

2.3 Colloidal Jamming

Jamming has gained considerable attention in the last decades, being present in our daily life, e.g., occurring in systems such as granular matter [32], pedestrian and traffic flow [33–35], and also colloidal suspensions [6]. Since jamming occurs in such diverse systems, Liu and Nagel [38] suggested that a universal principle must be responsible. During jamming a system is caught in a small region of the phase space due to an externally applied stress. In this state the system has properties akin to a solid body, thus being able to withstand heavy loads as long as the stress vector does not change its direction. However, as soon as the stress vector shifts out of its initial alignment, the system flows until the elements readapt to the new stress and jam once again.

Cates *et al.* [31] described these kind of systems as "fragile matter". In response to external stresses force chains based on physical contact between the individual elements

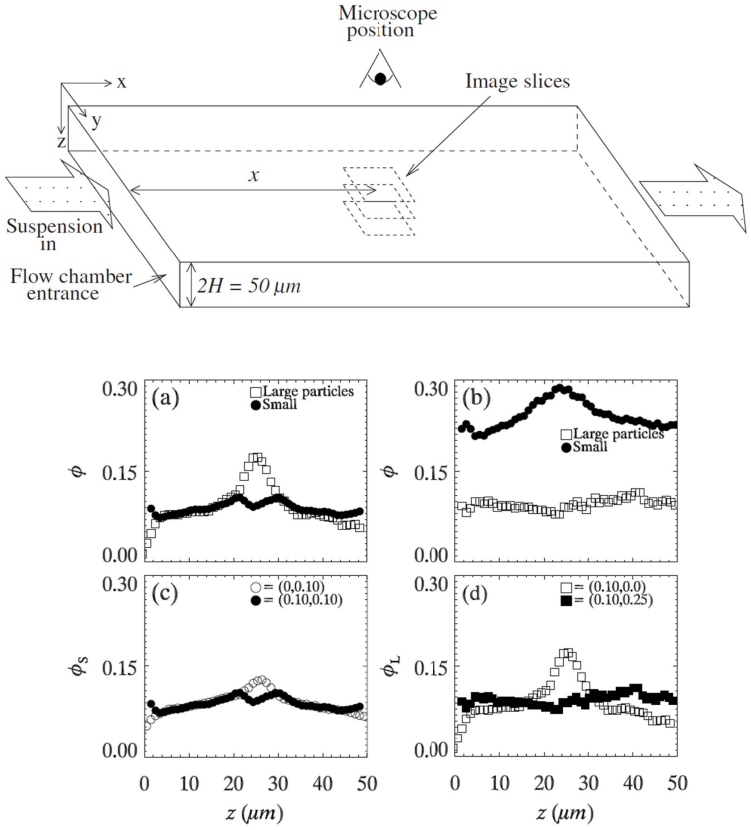

Figure 2.4: Top: Schematic representation of the rectangular-cross-section flow chamber showing the relative position of the microscope. Bottom: Concentration profiles along z showing enrichment of the channel center by large and small particles of a binary suspension.(a) Center enrichment by the large particles for $(\phi_\mathrm{l}, \phi_\mathrm{s}) = (0.1, 0.1)$, with $a_\mathrm{l}/a_\mathrm{s} \approx 2$. (b) Center enrichment by the small particles for $(\phi_\mathrm{l}, \phi_\mathrm{s}) = (0.1, 0.25)$. (c) Comparison of monodisperse suspension of $\phi_\mathrm{s} = 0.1$ with the small particles in binary suspension $(\phi_\mathrm{l}, \phi_\mathrm{s}) = (0.1, 0.1)$. (d) Comparison of monodisperse suspension of $\phi_\mathrm{l} = 0.1$ with the large particles in binary suspension $(\phi_\mathrm{l}, \phi_\mathrm{s}) = (0.1, 0.25)$. Reprinted from D. Semwogerere and E. R. Weeks [Phys. Fluids **20**, 043306 (2008)], with the permission of AIP Publishing.

of a granular system are formed. For hard particles such force chains are extremely sensitive to perturbations. A prominent example is a sand pile that maintains its shape under the influence of gravity due to jamming. As soon as the pile is externally vibrated its heaped structure would melt down.

In contrast to granular matter, colloidal suspensions are characterized by thermal noise and repelling lubrication forces which appear to hinder the formation of force chains. In the literature on colloidal suspensions, it is still hotly debated whether colloidal systems bear analogies to granular systems [39, 89].

2.3.1 Discontinuous Shear Thickening

Dense suspensions exhibit rich non-Newtonian rheology. At low to intermediate densities an applied shear stress can lead to shear thinning [90–92], i.e., a decrease in shear viscosity as the applied stress is increased. During shear thinning particles form bands parallel to the shear, which allows the layers to slip past each other with reduced fric-

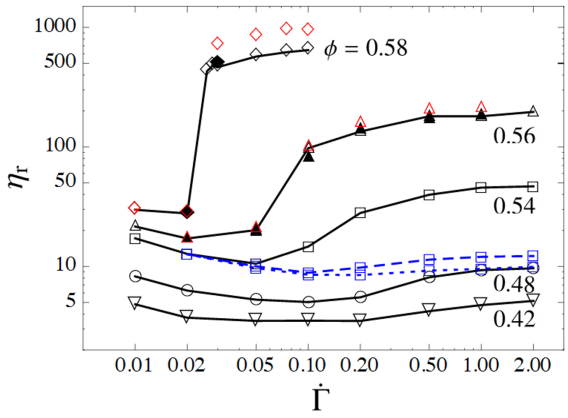

Figure 2.5: Shear rate $\dot{\Gamma}$ dependence of the relative viscosity η_r. The friction coefficient is $\mu = 1$ except for the dashed and dotted blue lines, for which $\mu = 0.1$ and 0, respectively. Red symbols show the results with 1.5 times stiffer particles. Reprinted figure with permission from R. Seto *et al.* [Phys. Rev. Lett. **111**, 218301 (2013)] Copyright (2013) by the American Physical Society.

tion. On the other hand, suspensions with high packing fractions experience shear thickening with the shear viscosity increasing with increased shear stress. A prominent example is the shear thickening of corn starch [36, 37], which enables a person to run over the liquid surface. Also, cases of discontinuous shear thickening were reported in both colloidal and non-Brownian suspensions [40, 93]. In discontinuous shear thickening the viscosity jumps at a critical shear stress with a constant volume fraction ϕ. Discontinuous shear thickening has been difficult to reproduce by numerical simulations although considerable effort has been put into understanding the underlying principles. In colloidal suspensions, so called "hydroclusters" have been proposed as possible mechanism for shear thickening [91, 94]. In this model the forces keeping particles apart like lubrication and thermal motion compete with forces imposed by the shear stress tending to push particles together. Although continuous shear thickening is captured, discontinuous shear thickening has never been reproduced by contact-free models.

Recently, Seto *et al.* [42] provided simulation results using frictional contacts between particles that successfully produced discontinuous shear thickening, see Fig. 2.5. The authors combined Stokesian dynamics simulations with a frictional contact model usually used for describing granular matter. The tangential forces F_t of the particles were subject to Coulomb's law of friction, which reads

$$F_t \leq \mu F_n, \tag{2.4}$$

with normal force F_n and the friction coefficient μ. Eq. (2.4) states that forces of static friction between colloids in contact cannot exceed a threshold μF_n. This results in particles, which stick if $F_t < \mu F_n$ and in frictional sliding if $F_t = \mu F_n$. A coefficient of $\mu = 0$ corresponds to frictionless sliding because $F_t = 0$ must hold independent of the normal force.

The blue dashed and dotted lines in Fig. 2.5 correspond to $\mu = 0.1$ and 0 at $\phi = 0.54$ and exhibit little to no shear thickening indicated by a roughly constant viscosity η_r along the shear rate $\dot{\Gamma}$. In contrast, if $\mu = 1$ (solid lines) discontinuous shear thickening is evident for a volume fraction of $\phi = 0.58$ indicated by the jump in friction around $\dot{\Gamma} = 0.02$.

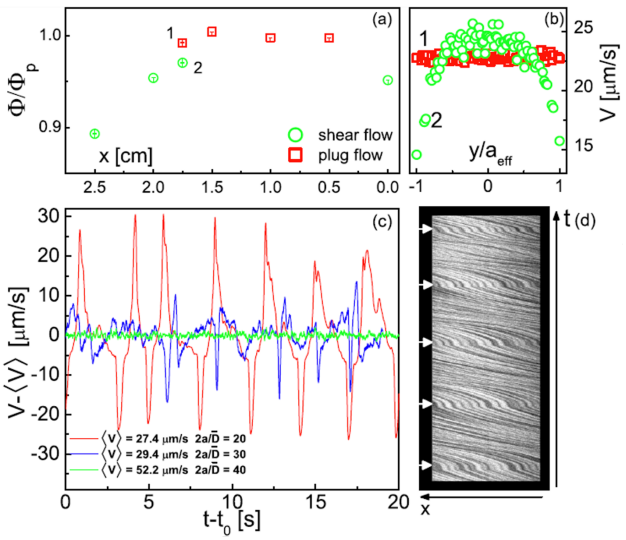

Figure 2.6: (a) Normalized particle volume fraction as a function of x (along the channel with the inlet at $x = 0$). (b) Velocity profiles along the width of the channel corresponding to points 1 and 2 in (a). (c) Velocity offset by the long-time average as a function of time for three different channel sizes. (d) Space-time (x-t) diagram of oscillating flow in $a = 20\overline{D}$ channel. The arrows highlight jamming events. Reprinted figure with permission from L. Isa *et al.* [Phys. Rev. Lett. **102**, 058302 (2009)] Copyright (2009) by the American Physical Society.

In the same year Heussinger [43] and also Fernandez *et al.* [41] provided evidence supporting the importance of implementing contact friction to model discontinuous shear thickening. These results strongly justify using tools from granular matter research to describe flow of dense colloidal suspensions.

2.3.2 Velocity Oscillations in Channel Flow

In their experiment on pressure driven flow of dense colloidal suspensions through microchannels, Isa *et al.* [44] verified regularly spaced oscillations in flow speed v. The authors used spheres of diameter $\overline{D} = 2.6 \pm 0.1\mu$m suspended in a density matched fluid with a volume fraction of $\phi \gtrsim 0.63$. Using confocal microscopy, the colloidal fluid was shown to alternate between plug like creeping flow and parabolic free flow, as displayed in Fig. 2.6 b). The oscillations have been attributed to the formation of transient jams for which the authors stressed the importance of shear thickening under confinement [36]. The oscillations are absent in wider channels as can be seen in Fig. 2.6 c). Strong oscillations are evident in a channel with width $20\overline{D}$, decrease with width $30\overline{D}$ and disappear for a width of $40\overline{D}$. As Brownian motion hinders the formation of jams, the oscillations only emerge at a mean flow speed threshold $\langle v \rangle_{\mathrm{thr}}$, that is when the corresponding Péclet number is large. Above this threshold the frequency follows the power-law $f \propto (\langle v \rangle - \langle v \rangle_{\mathrm{thr}})^{\beta}$, with exponent $\beta = 0.34 \pm 0.13$. Furthermore, the authors could indirectly verify the existence of density-rarefaction in pulses traveling upstream by measuring the gradient of the flow speed of tracer particles in the frame of the pulse.

In a different experiment Campbell and Haw [45] investigated the pressure-driven flow of concentrated colloidal suspensions into a converging channel geometry. Using optical microscopy, the authors imaged the flow speed in the entrance zone and found regular oscillations with long period above a volume fraction of $\phi = 0.505$ as displayed

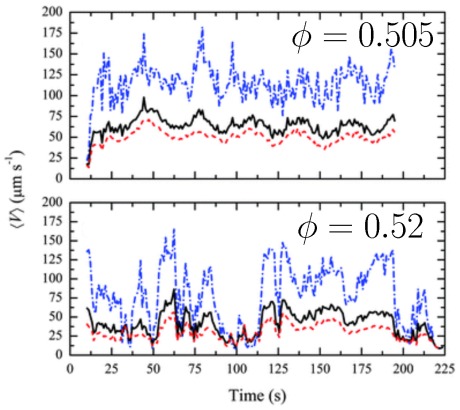

Figure 2.7: Mean flow rates $\langle V \rangle$ for dispersions drawn into the capillary using a pump over full image area (solid line), within the entrance zone (dashed-dotted line) and outside of the zone (dashed line). For $\phi = 0.505$, long period oscillations are clearly visible in the flow rate. For $\phi = 0.52$, the dispersion cycles through numerous flow-jam-flow states. Reproduced in part from A . I. Campbell and M. D. Haw [Soft Matter **6**, 4688 (2010)] with permission of The Royal Society of Chemistry.

in Fig. 2.7 top. They found that by slightly increasing the colloidal volume fraction to $\phi = 0.52$, the periodic oscillations in flow speed transformed into transient pulses separated by irregular long-lived jams, see Fig. 2.7, bottom. They argued that the observed phenomena are consistent with computer simulations of granular systems and linked the behavior to the concept of fragile matter [31].

3 Theoretical Foundations

As outlined in the previous chapter, colloidal particles interact via hydrodynamic flow-fields at vanishingly small Reynolds numbers. In this regime, inertial forces are dominated by viscous forces of the fluid. Consequently, passive particles only move when there is an active flow field. This chapter introduces the physical principles of creeping-flow hydrodynamics governed by the Stokes equation. Solutions for flow fields in channel geometries and around spheres are presented. Moreover, the physics of Brownian motion are discussed in more detail by presenting the fundamental fluctuation-dissipation theorem. Next, to understand the properties of our particle based simulation method, we derive the properties of an ideal gas and the Maxwell Boltzmann distribution from kinetic gas theory. Finally, we introduce mathematical tools to conduct a stability analysis and identify bifurcations in nonlinear differential equations.

Throughout this chapter and beyond the following notation is adopted using Einstein summation convention: Vectors are denoted by bold symbols $\mathbf{v} = v_i \mathbf{e}_i \in \mathbb{R}^d$ with basis vectors $\mathbf{e}_i$ and where d marks the spatial dimension. The tensor product between two vectors $\mathbf{v}$ and $\mathbf{u}$ results in a second rank tensor $\mathbf{T} = \mathbf{v} \otimes \mathbf{u} \coloneqq v_i u_j \mathbf{e}_i \otimes \mathbf{e}_j \in \mathbb{R}^d \times \mathbb{R}^d$. The transposed of a second-rank tensor is defined as $\mathbf{T}^\top = (T_{ij}\mathbf{e}_i \otimes \mathbf{e}_j)^\top \coloneqq T_{ji}\mathbf{e}_i \otimes \mathbf{e}_j$. The unit tensor is represented by $\mathbb{1} = \delta_{ij}\mathbf{e}_i \otimes \mathbf{e}_j$, where δ_{ij} is the Kronecker delta, which is 1 for $i = j$ and 0 otherwise. The scalar product between two vectors $\mathbf{v}$ and $\mathbf{u}$ is symbolized by $\mathbf{v} \cdot \mathbf{u} \coloneqq v_i u_i$. With the scalar product we can define the length of a vector as $|\mathbf{v}| = v \coloneqq \sqrt{\mathbf{v} \cdot \mathbf{v}}$. The time coordinate is denoted by t. Spatial coordinates are commonly represented by the position vector $\mathbf{r} = x_i \mathbf{e}_i$. In chapters 5 and 6 the vector components x_1, x_2 and x_3 are typically shortened to x, y and z. The nabla operator is defined as $\boldsymbol{\nabla} = \mathbf{e}_i \frac{\partial}{\partial x_i}$ and the Laplace operator as $\Delta \coloneqq \boldsymbol{\nabla} \cdot \boldsymbol{\nabla}$.

3.1 Hydrodynamics at Low Reynolds Number

On length scales much larger than the composing molecules, the fluid can be described as a continuum with fields of density $\rho(\mathbf{r}, t)$, velocity $\mathbf{v}(\mathbf{r}, t)$, stresses $\boldsymbol{\sigma}(\mathbf{r}, t)$, and temperature $T(\mathbf{r}, t)$. For simplicity, in the following we omit in the notation the dependence of the fields on point in space $\mathbf{r}$ and time t.

Given some initial conditions, the famous Navier-Stokes equations determine the flow field of a fluid. The equations were developed by Claude-Louis Navier and George Gabries Stokes in 1822 [95] based on the classical mechanics established by Newton. The

Navier-Stokes equations combine Newton's second law with a fluid stress due to viscous and pressure forces and forms a system of nonlinear partial differential equations. The nonlinearity causes turbulence and unpredictability, which makes it difficult to solve the equation analytically in most practical applications.

The Navier-Stokes equation can be derived from conservation laws applied to mass density and momentum of the fluid [96]. For the mass density ρ the continuity equation reads

$$\frac{\partial \rho}{\partial t} + \boldsymbol{\nabla} \cdot (\rho \mathbf{v}) = 0. \tag{3.1}$$

In most applications it is safe to assume that the flow is incompressible, i.e., ρ =const. This is especially true for low Reynoldsnumber flow at room temperature. Equation (3.1) then simplifies to

$$\boldsymbol{\nabla} \cdot \mathbf{v} = 0. \tag{3.2}$$

The conservation law for the momentum $\rho\mathbf{v}$ for an incompressible fluid reads

$$\rho \left(\frac{\partial \mathbf{v}}{\partial t} + \mathbf{v} \cdot \boldsymbol{\nabla} \otimes \mathbf{v} \right) = \boldsymbol{\nabla} \cdot \boldsymbol{\sigma} + \mathbf{f}, \tag{3.3}$$

where the right hand side are forces acting on the fluid due to both external forces $\mathbf{f}$ and divergence of stress $\boldsymbol{\sigma}$. The stress tensor $\boldsymbol{\sigma}$ is composed of normal volumetric stresses due to fluid pressure p and of shear stresses denoted by $\boldsymbol{\tau}$, such that

$$\boldsymbol{\sigma} = -p\mathbb{1} + \boldsymbol{\tau}. \tag{3.4}$$

For a Newtonian fluid the components of the shear stress $\boldsymbol{\tau}$ are proportional to the rate of deformation, i.e., the gradient of the flow field $\mathbf{v}$. The shear stress is defined as

$$\boldsymbol{\tau} = \eta \left(\boldsymbol{\nabla} \otimes \mathbf{v} + (\boldsymbol{\nabla} \otimes \mathbf{v})^{\top} \right), \tag{3.5}$$

where η is called the shear viscosity of the fluid, which is a measure of the resistance of the fluid to gradual deformation by shear stress.

Combining equations (3.3)-(3.5), the Navier-Stokes equation for an incompressible Newtonian fluid reads

$$\rho \left(\frac{\partial \mathbf{v}}{\partial t} + \mathbf{v} \cdot \boldsymbol{\nabla} \otimes \mathbf{v} \right) = -\boldsymbol{\nabla} p + \eta \Delta \mathbf{v} + \mathbf{f}. \tag{3.6}$$

To solve for the unknown fluid velocity field $\mathbf{v}$ and pressure field p, Eqs. (3.6) and (3.2) need to be integrated with respective boundary and initial conditions.

A major simplification of Eq. (3.6) results from restricting the investigated flow to small velocities and length scales. This eliminates the nonlinear term and makes the equations much easier to handle.

3.1.1 The Stokes equation

We rewrite Equation (3.6) in dimensionless units by introducing characteristic length a, characteristic time τ and characteristic flow velocity v. Rescaled dimensionless variables

are denoted by a prime $(...)'$, so that

$$\mathbf{x}' = \mathbf{x}/a, \tag{3.7}$$
$$\mathbf{v}' = \mathbf{v}/v, \tag{3.8}$$
$$t' = t/\tau, \tag{3.9}$$
$$\boldsymbol{\nabla}' = a\boldsymbol{\nabla}, \tag{3.10}$$
$$\Delta' = a^2\Delta, \tag{3.11}$$
$$p' = p/\frac{v\eta}{a}, \tag{3.12}$$
$$\mathbf{f}' = \mathbf{f}/\frac{v\eta}{a^2}. \tag{3.13}$$

With the rescaled variables Eq. (3.6) reads

$$\frac{a^2\rho}{\eta\tau}\frac{\partial \mathbf{v}'}{\partial t'} + \mathrm{Re}\,\mathbf{v}'\cdot\boldsymbol{\nabla}'\otimes\mathbf{v}' = -\boldsymbol{\nabla}'p' + \Delta'\mathbf{v}' + \mathbf{f}'. \tag{3.14}$$

The dimensionless number Re is called Reynolds number and has already been introduced in chapter 2. With the dynamic viscosity η the Reynolds number is defined as

$$\mathrm{Re} = \frac{\rho v a}{\eta}. \tag{3.15}$$

The kinematic viscosity ν is related to the dynamic viscosity η by the relation $\eta = \rho\nu$, so that an equivalent representation of the Reynolds number is $\mathrm{Re} = va/\nu$.

Now, if the Reynolds number is small ($\mathrm{Re} \ll 1$) the force terms on the right-hand side of Eq. (3.14) become important. The nonlinear convective term on the left side of Eq. (3.14) becomes insignificant. Consequently, for problems with small Reynolds numbers, e.g., in creeping flow, swimming bacteria and colloidal dynamics, the nonlinear term $\mathbf{v}'\cdot\boldsymbol{\nabla}'\otimes\mathbf{v}'$ is typically omitted. As a result, one obtains the time-dependent Stokes equation [97]:

$$\rho\frac{\partial \mathbf{v}}{\partial t} = -\boldsymbol{\nabla}p + \eta\Delta\mathbf{v} + \mathbf{f}. \tag{3.16}$$

The flow described by Eq. (3.16) is laminar and free of turbulence. Moreover, since it is linear the superposition of solutions of Eq. (3.16) are also valid solutions.

In most applications the left-hand side of Eq. (3.14) can be omitted completely as characteristic time scales τ of interest are typically much larger than the viscous time scale $\tau_\eta = a^2\rho/\eta$, which appears as a factor of the time derivative in Eq. (3.14). For example, for a passive Brownian particle of radius a and density ρ the relaxation time is typically small $a^2\rho/\eta \approx 1\mathrm{ns} - 100\mathrm{ns}$. In this the case, Eq. (3.16) simplifies to the famous Stokes equations

$$\boldsymbol{\nabla}p - \eta\Delta\mathbf{v} = \mathbf{f} \quad \text{and} \quad \boldsymbol{\nabla}\cdot\mathbf{v} = 0. \tag{3.17}$$

The Stokes equations do not depend on time explicitly. As a result, the flow field adapts instantaneously to time variations of acting forces or moving boundaries. Furthermore, from the invariance of Eq. (3.17) to the transformation $t \to -t$ it becomes evident that processes described by the Stokes equation are time reversible when the external forces $\mathbf{f}$ are reversed.

Because the Stokes equation is linear, it can be solved with the aid of the Green function [98]. The flow field generated by a point force $\mathbf{g}_0$ located at the origin poses a fundamental solution of the Stokes equation and is called stokeslet. The force field is given by $\mathbf{g}(\mathbf{r}) = \mathbf{g}_0\delta(\mathbf{r})$, where $\delta(\mathbf{r})$ is the Dirac delta function defined as

$$\delta(\mathbf{r}) = \begin{cases} +\infty & \text{if } \mathbf{r} = 0 \\ 0 & \text{if } \mathbf{r} \neq 0 \end{cases}, \tag{3.18}$$

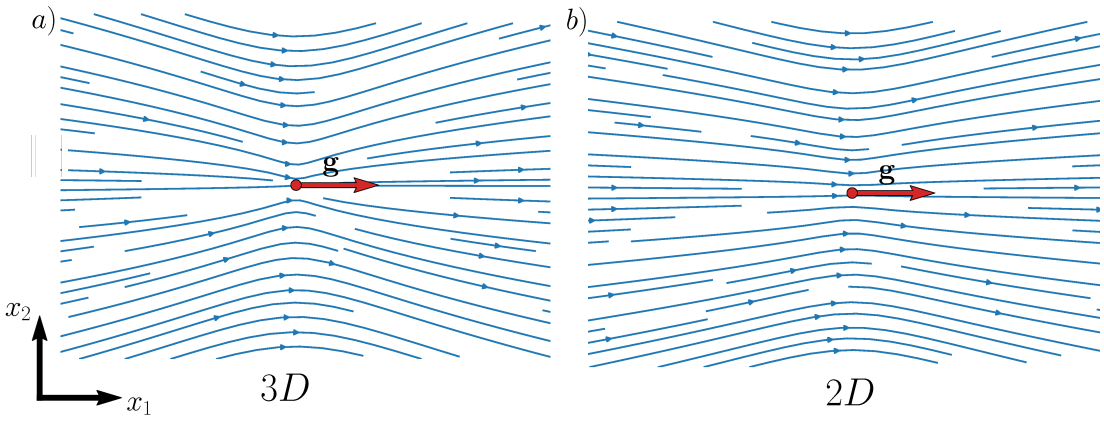

Figure 3.1: The fundamental solution of the Stokes equation showing a flow field around a point force $\mathbf{g}_0$. a) For 3 dimensions calculated from Eq. (3.20). b) For 2 dimensions calculated from Eq. (3.21)

and which satisfies $\int_{-\infty}^{\infty} \delta(\mathbf{r}) \mathrm{d}^d r = 1$.

The stokeslet is then calculated from [99]

$$\mathbf{v}(\mathbf{r}) = \mathbf{G}(\mathbf{r}) \cdot \mathbf{g}_0, \tag{3.19}$$

where the second rank tensor $\mathbf{G}$, commonly referred to as Oseen tensor, has been introduced. In three dimensions it is defined by

$$\mathbf{G}^{3\mathrm{D}}(\mathbf{r}) = \frac{1}{8\pi\eta} \left(\frac{\mathbb{1}}{r} + \frac{\mathbf{r} \otimes \mathbf{r}}{r^3} \right). \tag{3.20}$$

On the other hand, the Green tensor for two dimensional flow reads

$$\mathbf{G}^{2\mathrm{D}}(\mathbf{r}) = \frac{1}{4\pi\eta} \left(-\mathbb{1} \ln r + \frac{\mathbf{r} \otimes \mathbf{r}}{r^2} \right). \tag{3.21}$$

In Fig. 3.1 we plot the flow field of a point force in x_1 direction for two and three dimensions. From Eq. (3.20) it can be seen that the flow field far away from the point force decays as $1/r$. The next higher-order term is the stresslet generated by a force dipole, which decays as $\propto 1/r^2$ with growing distance to the dipole. In the case of two dimensions the flow generated by a force monopole looks qualitatively the same. Note that the flow strength decays more slowly with growing distance than its three-dimensional counter part, i.e., logarithmically, $|\mathbf{v}(r)| \propto -\ln r$. Due to the linearity of the Eqs. (3.17),for a continuous force density $\mathbf{g}(\mathbf{r})$, the flow is a superposition of fields generated by forces acting on each point of the fluid. Equation (3.19) can then be written as the volume integral

$$\mathbf{v}(\mathbf{r}) = \int \mathbf{G}(\mathbf{r}) \cdot \mathbf{g}(\mathbf{r}) \mathrm{d}V. \tag{3.22}$$

3.1.2 No-slip boundary condition

In most practical applications, flow with confining boundaries is considered. Due to attractive interaction between fluid molecules and rigid boundaries, e.g., walls and surfaces of suspended particles, the slip close to the wall does not exceed that of the mean free path of the fluid molecules [100]. On length scales much larger than the mean free

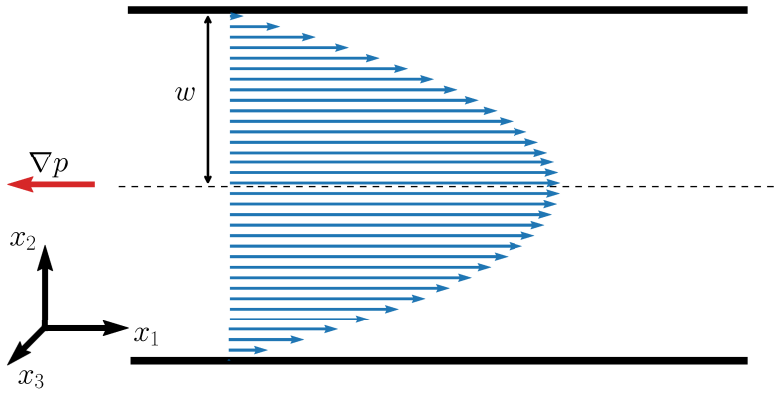

Figure 3.2: View of the Poiseuille flow profile inside a channel of width $2w$ in the x_1, x_2-plane calculated from Eq. (3.26).

path the fluid is assumed to "stick" to the surface. As a result, throughout this thesis we assume a no-slip boundary condition [101] which reads

$$\mathbf{v}(\mathbf{r})|_{\mathbf{r}\in\partial\Omega} = 0, \tag{3.23}$$

where $\partial\Omega$ is the surface of an object defined by Ω. For a rigid body suspended in the fluid that can freely translate with velocity $\mathbf{u}$ and rotate with angular velocity $\boldsymbol{\omega}$, the no-slip boundary condition reads

$$\mathbf{v}(\mathbf{r})|_{\mathbf{r}\in\partial\Omega} = \mathbf{u} + \boldsymbol{\omega} \times (\mathbf{r} - \mathbf{r}_\mathrm{c}), \tag{3.24}$$

where $\mathbf{r}_\mathrm{c}$ denotes the center of mass of the rigid body.

3.1.3 Poiseuille flow

Analytic solutions of the Navier-Stokes equations (3.6) as well as the Stokes equations (3.17) only exist in rare cases. The pressure-driven flow in channel geometries represents one of such cases and is of practical relevance in microfluidics and biophysics [102, 103]. The corresponding solution of Eq. (3.17) is called Poiseuille flow. The particular solution presented here is that of flow between two infinite parallel plates [104]. This geometry induces flow, which is effectively two-dimensional and of great relevance for this thesis as most simulation were conducted in two dimensions. For simplicity, we consider infinite parallel walls in the x_1, x_3-plane, which are separated by a distance $2w$, so that one wall is located at $x_2 = -w$ and the other at $x_2 = w$. A constant pressure gradient $\boldsymbol{\nabla} p = -g\mathbf{e}_1$ is applied and drives the Newtonian fluid along x_1. External forces $\mathbf{f}$ are neglected.

We assume a no-slip boundary condition. Consequently, at the walls the boundary condition $\mathbf{v}(-w) = 0$ and $\mathbf{v}(w) = 0$ holds. Furthermore, due to symmetry, the flow orthogonal to the pressure gradient is zero, i.e. $\mathbf{v} \cdot \mathbf{e}_2 \equiv 0$ and $\mathbf{v} \cdot \mathbf{e}_3 \equiv 0$ as are the gradients of the flow in direction parallel to the wall, i.e. $\frac{\partial}{\partial x_1}\mathbf{v} = 0$ and $\frac{\partial}{\partial x_3}\mathbf{v} = 0$. Equation (3.17) then reads

$$-g\mathbf{e}_1 - \eta \frac{\partial^2 v}{\partial x_2^2}\mathbf{e}_1 = 0, \tag{3.25}$$

where we can omit the unit vectors. Eq. (3.25) can be easily integrated and after using the no-slip boundary condition the flow field is found to be

$$v(x_2) = \frac{g}{2\eta}(w^2 - x_2^2). \tag{3.26}$$

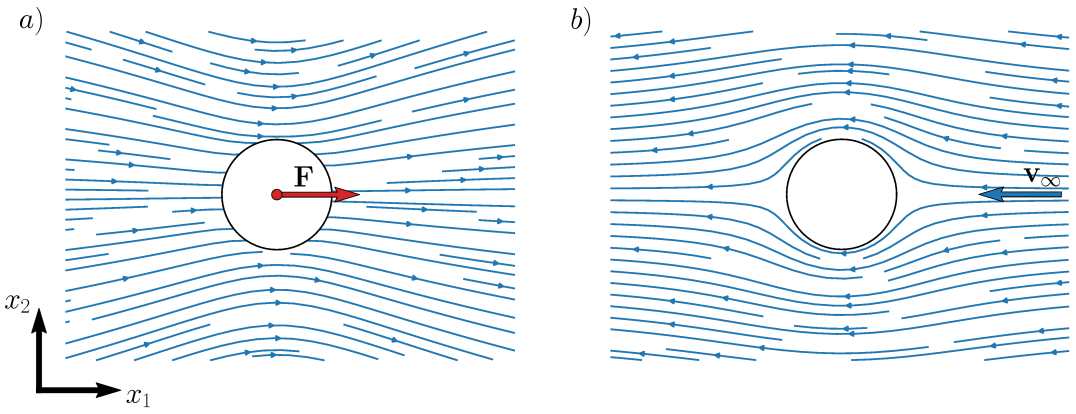

Figure 3.3: Stream line plot of flow past a sphere in the x_1, x_2-plane calculated from Eq. (3.28) for: a) In the frame of a quiescent observer. b) In the frame of the moving sphere.

The flow is displayed in Fig. 3.2 in the x_1, x_2-plane, showing a parabolic flow profile with zero velocity at the walls and maximum velocity in the center of the channel. The value of the latter can be calculated from setting $x_2 = 0$:

$$v_{\max} = \frac{gw^2}{2\eta}. \tag{3.27}$$

3.1.4 Flow past a sphere

In the following, we deal with the flow past a sphere of radius a. Two approaches to obtain the flow field prove to be equivalent. One can either drag the sphere with a constant force $\mathbf{F} = F\mathbf{e}_1$ through the liquid or imagine the sphere put at rest in a constant flow field $\mathbf{v}(\mathbf{r}, t) = v_\infty \mathbf{e}_1$. In the frame of an observer at rest, the flow field can be expressed as [99]

$$\mathbf{v}(\mathbf{r}) = \mathbf{S}(\mathbf{r}) \cdot \mathbf{v}_\infty, \tag{3.28}$$

where

$$\mathbf{S}(\mathbf{r}) = \frac{3}{4}\frac{a}{r}\left(\mathbb{1} + \frac{\mathbf{r}\otimes\mathbf{r}}{r^2}\right) + \frac{1}{4}\frac{a^3}{r^3}\left(\mathbb{1} - 3\frac{\mathbf{r}\otimes\mathbf{r}}{r^2}\right), \tag{3.29}$$

which can be calculated from Eq. (3.22) using the multi-pole expansion of the Oseen tensor (3.20) to fit the boundary conditions represented by Eq. (3.24) for zero angular velocity $\boldsymbol{\omega}$ and for drag velocity $\mathbf{v}_\infty$ [99]. In Fig. 3.3 a) we show the flow field in the frame of a resting observer generated by Eq. (3.28) and (3.29). The flow field far from the sphere reminds of that generated by a stokeslet in Fig. 3.1. And indeed, at large distances to leading order the tensors $\mathbf{G}$ and $\mathbf{S}$ behave identical, since $\mathbf{S}$ is dominated by the force monopole. Figure 3.3 b) shows the same flow field but placed in the frame of the moving sphere. Mathematically, both flow fields are merely shifted by the constant vector $\mathbf{v}_\infty$.

The force $\mathbf{F}$ required to drag the sphere with velocity $\mathbf{v}_\infty$ or the drag force $\mathbf{F}$ exerted on a resting sphere by an external flow field $\mathbf{v}_\infty$, can be calculated using the surface integral

$$\mathbf{F} = \int_{\partial\Omega} \boldsymbol{\sigma} \cdot \mathbf{n} \mathrm{d}S. \tag{3.30}$$

The drag force $\mathbf{F}$ for a spherical particle then becomes

$$\mathbf{F} = 6\pi\eta a \mathbf{u}_\infty = \zeta^{\mathrm{3D}}_{\mathrm{drag}} \mathbf{u}_\infty, \tag{3.31}$$

where

$$\zeta_{\text{drag}}^{\text{3D}} = 6\pi\eta a \tag{3.32}$$

is the translational friction constant [99].

Equation (3.32) is commonly known as the Stokes formula for a sphere dragged through a viscous fluid. By changing the boundary conditions to that of a stationary ($\mathbf{v}_\infty = 0$) rotating sphere with angular velocity $\boldsymbol{\omega}$, the rotational friction constant becomes [99]

$$\zeta_{\text{rot}}^{\text{3D}} = 8\pi\eta a^3. \tag{3.33}$$

3.1.5 Stokes paradox and flow past a cylinder

The Stokes equation (3.17) as presented in section 3.1.1 does not have a solution for unbounded flow past a circular cylinder. This problem is known as the Stokes paradox [105, 106]. The reason for this can be found in the decay rate of the flow strength of the stokeslet at infinity. Whereas in three dimensions the flow field converges to zero at large distances with $1/r$, it does not in two dimensions, where the flow field decays proportional to $-\ln r$. The paradox itself results from the failure to balance the viscous forces at infinity, however small the Reynolds number of the given problem.

Oseen elucidated the paradox and solved it by introducing an approximate inertial term into the Stokes equation that properly accounts for the singular nature of the limit $\text{Re} \to 0$ [107]. For a constant background flow $\mathbf{v}_\infty = v_\infty \mathbf{e}_1$ in the direction of x_1, the approximate inertial term reads

$$\mathbf{v} \cdot \boldsymbol{\nabla} \otimes \mathbf{v} \approx \mathbf{v}_\infty \cdot \boldsymbol{\nabla} \otimes \mathbf{v} = v_\infty \frac{\partial \mathbf{v}}{\partial x_1}. \tag{3.34}$$

The so-called Oseen equations then read

$$\rho v_\infty \frac{\partial \mathbf{v}}{\partial x_1} + \boldsymbol{\nabla} p - \eta \Delta \mathbf{v} = \mathbf{f} \quad \text{and} \quad \boldsymbol{\nabla} \cdot \mathbf{v} = 0. \tag{3.35}$$

With Eq. (3.35) the boundary conditions at infinity can be met and the friction coefficient for a cylinder of radius a and nonzero Reynolds number becomes [108]

$$\zeta_{\text{drag}}^{\text{2D}} = \frac{4\pi\eta}{\frac{1}{2} - \gamma - \log(8\text{Re})}. \tag{3.36}$$

Here, $\gamma \approx 0.577$ denotes Euler's constant and the Reynolds number corresponds to $\text{Re} = \rho a v_\infty / \eta$. In accordance with the three dimensional case, the friction is proportional to the fluid viscosity η. However, in two dimensions the particle size a enters weakly inside the logarithm of the Reynolds number in the denominator instead of linearly in Eq. (3.32).

The rotational friction of a cylinder in two dimensions is exactly described by Faxén's law and reads [109]:

$$\zeta_{\text{rot}}^{\text{2D}} = 4\pi\eta a^2. \tag{3.37}$$

By comparing Eq. (3.37) with Eq. (3.33) it becomes evident that the rotational drag also scales differently with particle size a for different dimensions, i.e., square versus cubic dependence.

The dependence of the drag coefficients on the spatial dimension will be addressed in chapter 5 by direct comparison of two and three dimensional simulations as well as within the formulation of a phenomenological theory.

Figure 3.4: Random walk process of three particles generated by the simulation method multi-particle collision dynamics.

3.2 Statistical Physics of Passive Particles

The hydrodynamic forces and flow fields derived in the previous section are perfectly deterministic. Based on Newton's classical mechanics, given initial and boundary conditions, the flow field can therefore be determined for all times in the future. This conflicts with the observations of Scottish botanist Robert Brown during the examination of grains of pollen suspended in water under the microscope in 1827. He found that the amyloplasts and spherosomes, which were emitted by the pollen, to undergo erratic movements (see Fig. 3.4). The origin of this motion was attributed much later to the thermally driven collisions of the surrounding fluid molecules with the particles [61, 110]. This stochastic motion, commonly known as Brownian motion, is a characteristic property of micron sized objects. Collisions with the fluid molecules become visible as Brownian motion when the object is not significant larger than the fluid molecules, whereas suspended macroscopic objects average over a huge number of collisions with fluid molecules. Consequently, while the deterministic hydrodynamic equations suffice to treat the dynamics of macroscopic bodies suspended in fluid, for mesoscopic particles the fluid needs to be treated as a source of noise that causes random motion.

3.2.1 The Langevin equation

A single particle of mass m suspended in a fluid obeys Newton's equation of motion. The force acting on the particle is composed of external forces $\mathbf{f}_{\text{ext}}$ and translational friction. For the latter, in the limit of the Stokes equation, a linear relation between drag force and swimming velocity with constant of proportionality ζ is found (see Section 3.1.4). Moreover, to account for the thermal noise a stochastic force $\mathbf{\Gamma}(t)$ needs to be added. The equation of motion then reads

$$m\frac{\mathrm{d}\mathbf{v}}{\mathrm{d}t} = -\zeta\mathbf{v} + \mathbf{\Gamma}(t) + \mathbf{f}_{\text{ext}}. \tag{3.38}$$

Eq. (3.38) is known as the Langevin equation [111]. It can be formally solved as a first-order inhomogeneous differential equation, to yield

$$\mathbf{v}(t) = \mathbf{v}(0)\exp\left(-t/\tau_{\text{r}}\right) + \frac{1}{m}\int_0^t \mathrm{d}t' \exp\left(-(t-t')/\tau_{\text{r}}\right)\mathbf{\Gamma}(t'), \tag{3.39}$$

where the relaxation time $\tau_{\text{r}} = m/\zeta$ is a measure for the time required for the inertial movement of the particle to decay due to viscous friction. Due to the stochastic character

of $\mathbf{\Gamma}(t)$, Eq. (3.40) cannot be solved explicitly. Instead, ensemble averages denoted by the operator $\langle ... \rangle$, are applied to describe the dynamics of the stochastic differential equations for a large number of possible realizations.

On time scales well above the relaxation time of the particle $t \gg \tau_\mathrm{r}$, the Langevin Eq. (3.38) reduces to the overdamped Langevin equation

$$\zeta \frac{\mathrm{d}\mathbf{r}}{\mathrm{d}t} = \mathbf{\Gamma}(t) + \mathbf{f}_\mathrm{ext}. \tag{3.40}$$

3.2.2 Fluctuation-dissipation theorem

For further calculations we need to define the properties of the noise term $\mathbf{\Gamma}(t)$. For simplicity we assume no external force, $\mathbf{f}_\mathrm{ext} = 0$. As the random force has no preferred direction, the ensemble average vanishes

$$\langle \mathbf{\Gamma}(t) \rangle = 0. \tag{3.41}$$

Because the relaxation time τ_r of the particle is much larger than the inverse collision frequency of fluid molecules with the particle, it is plausible to assume a delta, correlated random force in time,

$$\langle \mathbf{\Gamma}(t) \otimes \mathbf{\Gamma}(t') \rangle = c\delta(t - t')\mathbb{1}. \tag{3.42}$$

Here, c is a constant which describes the strength of fluctuations. With aid of Eq. (3.39), the mean kinetic energy of translation of the particle yields

$$\frac{1}{2}m\langle v^2 \rangle = \frac{1}{2}mv^2(0)\exp\left(-2t/\tau_\mathrm{r}\right) + \frac{1}{2m}\int_0^t \int_0^t \mathrm{d}t'\mathrm{d}t'' \exp\left(-(2t - t' - t'')/\tau_\mathrm{r}\right) \langle \mathbf{\Gamma}(t') \cdot \mathbf{\Gamma}(t'') \rangle, \tag{3.43}$$

where we used Eq. (3.41). Equation (3.43) can be integrated utilizing Eq. (3.42) and we obtain

$$\frac{1}{2}m\langle v^2 \rangle = \frac{1}{2}mv^2(0)\exp\left(-2t/\tau_\mathrm{r}\right) + \frac{\tau_\mathrm{r}}{4m}c \overset{t \gg \tau_\mathrm{r}}{=} \frac{\tau_\mathrm{r}}{4m}c. \tag{3.44}$$

In the last step the mean kinetic energy is written at times when the initial velocity has completely decayed.

From the equipartition theorem it is known that on average and in equilibrium each degree of freedom of a system obtains the thermal energy $k_\mathrm{B}T/2$ [112]. For a rigid particle in d dimensions the translational kinetic energy reads

$$\frac{1}{2}m\langle v^2 \rangle = \frac{d}{2}k_\mathrm{B}T, \tag{3.45}$$

where k_B is the Boltzman constant and T the absolute temperature. Comparing Eq. (3.44) with (3.45) leads to

$$\langle \mathbf{\Gamma}(t) \cdot \mathbf{\Gamma}(t') \rangle = 2dk_\mathrm{B}T\zeta\delta(t - t'). \tag{3.46}$$

The relation (3.46) is referred to as the fluctuation-dissipation theorem of thermodynamics [113, 114]. The theorem states that if drag dissipates kinetic energy into heat there is a reverse process that causes thermal motion, i.e., heat translated into kinetic energy caused by the collisions of the fluid molecules.

3.2.3 Mean square displacement and Einstein relation

A key property in describing stochastic motion is the coefficient of diffusion D. It is a measure of the strength of the thermal motion of a particle. It is formally defined by

$$2dD = \lim_{t \to \infty} \frac{\mathrm{d}}{\mathrm{d}t} \langle (\mathbf{r}(t) - \mathbf{r}(0))^2 \rangle. \tag{3.47}$$

The term $\langle(\mathbf{r}(t)-\mathbf{r}(0))^2\rangle$ on the right hand side of Eq. (3.47) is called mean square displacement. It is a convenient measure describing stochastic dynamics due to its easy accessibility in experiments and simulation. The distance $\mathbf{r}(t)-\mathbf{r}(0)$ can be represented by the integral

$$\mathbf{r}(t)-\mathbf{r}(0)=\int_0^t \mathrm{d}t'\mathbf{v}(t'). \tag{3.48}$$

Using Eq. (3.48), the mean square displacement can be written as

$$\langle(\mathbf{r}(t)-\mathbf{r}(0))^2\rangle=\int_0^t \mathrm{d}t'\int_0^t \mathrm{d}t''\langle\mathbf{v}(t')\cdot\mathbf{v}(t'')\rangle=2\int_0^t \mathrm{d}t'\int_0^{t'} \mathrm{d}t''\langle\mathbf{v}(t')\cdot\mathbf{v}(t'')\rangle. \tag{3.49}$$

In the last step of Eq. (3.49) the symmetry of $\langle\mathbf{v}(t')\cdot\mathbf{v}(t'')\rangle$ was used to half the integration domain of the second integral. Taking the derivative with respect to time t as well as the limit of large times on both sides of Eq. (3.49), yields

$$\lim_{t\to\infty}\frac{\mathrm{d}}{\mathrm{d}t}\langle(\mathbf{r}(t)-\mathbf{r}(0))^2\rangle=\lim_{t'\to\infty}2\int_0^{t'} \mathrm{d}t''\langle\mathbf{v}(t')\cdot\mathbf{v}(t'')\rangle, \tag{3.50}$$

where we eliminated one of the integrals on the right hand side. If the system behaves ergodic, i.e., the ensemble average behaves as the time average, one can exploit the translational invariance in time. It states that the ensemble average of the product of velocities at different times t' and t'' only depends on the difference $t'-t''$. We can write

$$\langle\mathbf{v}(t')\cdot\mathbf{v}(t'')\rangle=\langle\mathbf{v}(t'-t'')\cdot\mathbf{v}(0)\rangle, \tag{3.51}$$

where the time was shifted by $t\to t-t''$.

Finally, by denoting $\tau=t'-t''$ Eq. (3.50) and Eq. (3.47) give the Green-Kubo formula for the diffusion constant [99, 115]:

$$D=\frac{1}{d}\int_0^\infty \mathrm{d}\tau\langle\mathbf{v}(\tau)\cdot\mathbf{v}(0)\rangle. \tag{3.52}$$

The right-hand side of Eq. (3.52) is called velocity autocorrelation function.

In the limit of small Reynolds numbers the velocity of a diffusing particle is provided by the overdamped Langevin equation (3.40). Using Eq. (3.40) together with the fluctuation-dissipation theorem Eq. (3.46), the right hand side of Eq. (3.52) can be integrated. Eq. (3.52) then shortens to

$$D=\frac{k_\mathrm{B}T}{\zeta}. \tag{3.53}$$

This is the famous Einstein relation (also known as Einstein-Smoluchowski relation) that connects the diffusion constant to the friction constant of a suspended object [61].

3.2.4 The Smoluchowski equation and Fick's law

Instead of following the evolution of a single trajectory $\mathbf{r}(t)$ determined by a unique realization of $\mathbf{\Gamma}(t)$ of the Langevin equation, the evolution of the probability density $\varphi(\mathbf{r},t)$ can be calculated. The probability of finding the particle in an infinitesimal small volume $\mathrm{d}V$ at time t is then simply $\varphi(\mathbf{r},t)\mathrm{d}V$. It can be shown that the overdamped Langevin equation (3.40) corresponds to the so-called Smoluchowski equation [116] (see Fig. 3.5)

$$\frac{\partial\varphi}{\partial t}=-\boldsymbol{\nabla}\cdot\left(\mathbf{u}_\mathrm{drift}\varphi-K\boldsymbol{\nabla}\varphi\right). \tag{3.54}$$

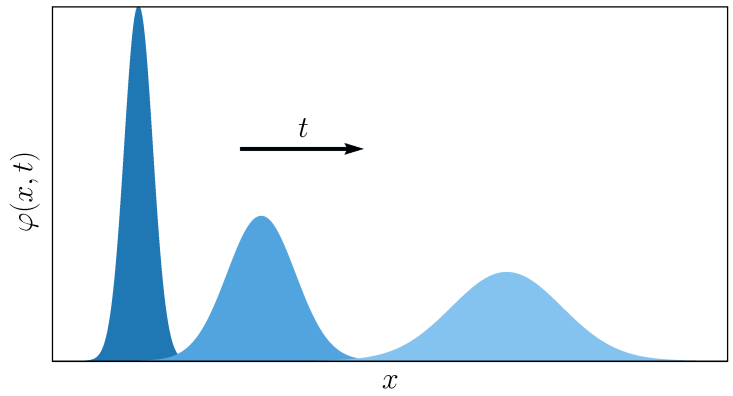

Figure 3.5: Illustrative solution of the Smoluchowski equation in one dimension with constant drift velocity u_{drift} and diffusion coefficient D.

Eq. (3.54) is a transport equation of probability density φ with the current $\mathbf{J} = \mathbf{u}_{\text{drift}}\varphi - D\boldsymbol{\nabla}\varphi$. The current consists of the deterministic drift $\mathbf{u}_{\text{drift}}\varphi$ and the diffusive current $-D\boldsymbol{\nabla}\varphi$ with diffusion coefficient D. The latter current is commonly referred to as Fick's first law

$$J_{\text{diff}} = -D\boldsymbol{\nabla}\varphi. \tag{3.55}$$

In order to show that Eq. (3.54) actually reproduces the well-known diffusive behavior of particles, we link it to the equilibrium properties presented in the previous section. In the following we therefore assume equilibrium, i.e. $\mathbf{u}_{\text{drift}} = 0$, as well as a constant diffusion coefficient D. The mean square displacement of a single particle can then be written with aid of the solution of Eq. (3.54) in the following way

$$\langle(\mathbf{r}(t) - \mathbf{r}(0))^2\rangle = \int_{-\infty}^{\infty} \mathrm{d}V(\mathbf{r}(t) - \mathbf{r}(0))^2\varphi. \tag{3.56}$$

Multiplying Eq. (3.54) with $(\mathbf{r}(t) - \mathbf{r}(0))^2$ and integrating yields

$$\frac{\mathrm{d}}{\mathrm{d}t}\langle(\mathbf{r}(t) - \mathbf{r}(0))^2\rangle = D\int_{-\infty}^{\infty} \mathrm{d}V(\mathbf{r}(t) - \mathbf{r}(0))^2\Delta\varphi, \tag{3.57}$$

where the identity (3.56) has been applied to the left hand side. Green's theorem for two functions g and h reads

$$\int_{-\infty}^{\infty} \mathrm{d}V\,(g\Delta h - h\Delta g) = \int_{-\infty}^{\infty} \mathrm{d}S\,(g\boldsymbol{\nabla}h - h\boldsymbol{\nabla}g)\cdot\mathbf{n}. \tag{3.58}$$

for an infinite volume. Considering the fact that φ must vanish at infinity, Eq. (3.57) results in

$$\frac{\mathrm{d}}{\mathrm{d}t}\langle(\mathbf{r}(t) - \mathbf{r}(0))^2\rangle = D\int_{-\infty}^{\infty} \mathrm{d}V\varphi\Delta(\mathbf{r}(t) - \mathbf{r}(0))^2. \tag{3.59}$$

With the identity $\Delta(\mathbf{r}(t) - \mathbf{r}(0))^2 = 2d$, the equation becomes

$$\frac{\mathrm{d}}{\mathrm{d}t}\langle(\mathbf{r}(t) - \mathbf{r}(0))^2\rangle = 2dD\int_{-\infty}^{\infty} \mathrm{d}V\varphi. \tag{3.60}$$

After using the fact that φ is normalized, we finally arrive at

$$\frac{\mathrm{d}}{\mathrm{d}t}\langle(\mathbf{r}(t) - \mathbf{r}(0))^2\rangle = 2dD. \tag{3.61}$$

We can conclude that the Smoluchowski Eq. (3.54) yields identical behavior as the overdamped Langevin Eq. (3.40) by comparing Eq. (3.61) with Eq. (3.47) at large times. Here, we can identify D with the diffusion coefficient defined by the Einstein relation (3.53).

3.3 Kinetic Gas Theory

The subject of this thesis is the investigation of processes on length scales where molecular movement is important. Having said this, finding the solution of a dynamical system described by a Hamiltonian featuring 10^{24} fluid molecules per gram of liquid is impossible and fortunately not necessary. As in the previous section, ensemble averages suffice to calculate important observables such as pressure and temperature from microscopic properties. The relations derived here become important in the next chapter when the mesoscopic simulation method multi-particle collision dynamics is introduced, which behaves as an ideal viscous gas.

3.3.1 The canonical ensemble

Imagine a closed system of N particles enclosed in a volume V. If the total energy E in the system is conserved, the number of microscopic states accessible for the system is denoted by $\Omega(E, V, N)$. The quantity $\Omega(E, V, N)$ is called partition function of the microcanonical ensemble and can be explicitly written as [112]

$$\Omega(E, V, N) = \frac{1}{N! h^{dN}} \int_V \mathrm{d}^{dN} q \int_{-\infty}^{\infty} \mathrm{d}^{dN} p \delta\left(E - H(q, p)\right), \tag{3.62}$$

where $q \in \mathbb{R}^{Nd}$ and $p \in \mathbb{R}^{Nd}$ denote generalized coordinates and momenta of the particles. The Planck constant h comes from the semi-classical approach and quantizes the phase space. The $N!$ in the denominator ensures that particles are indistinguishable. Moreover, the function $H(q, p)$ denotes the Hamiltonian energy function of the system. The partition function Ω is an important quantity in statistical physics as it allows for direct calculation of the thermodynamic variables such as temperature, entropy and pressure.

Because many processes in nature allow for an energy transport across boundaries due to heat diffusion, a different representation of Ω is desired as in Eq. (3.62). In the following we consider the situation displayed in Fig. 3.6. Both volumes V_1 and V_2 are fixed and are allowed to exchange heat across the boundaries but no particles. Both systems together are perfectly isolated so that the total energy $E = E_1 + E_2$ is conserved. The total number of accessible states of the coupled system is calculated by

$$\Omega(N, E) = \sum_{E_1} \Omega_1(N_1, E_1) \Omega_2(N, E - E_1), \tag{3.63}$$

The probability $P(E_1)$ of finding the small system in a state of energy E_1 is therefore

$$P(E_1) = \frac{\Omega_1(N_1, E_1) \Omega_2(N, E - E_1)}{\Omega(N, E)}. \tag{3.64}$$

In equilibrium, the probability density of a system consisting of many particles has a sharply peaked maximum. Consequently, it can be expected that E_1 assumes the most likely value. This value is obtained by differentiating with respect to E_1:

$$\frac{\partial \left(\Omega_1(N_1, E_1) \Omega_2(N_2, E - E_1)\right)}{\partial E_1} = 0. \tag{3.65}$$

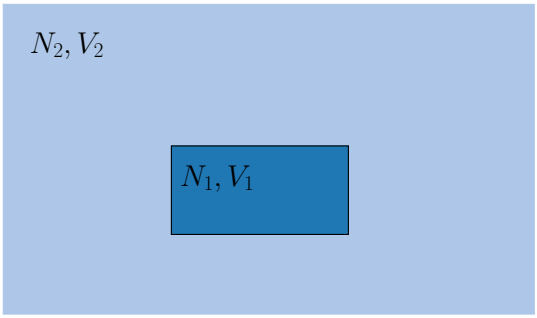

Figure 3.6: Small system (N_1, V_1) inside a heat bath (large system with N_2 and V_2). Energy can be exchanged via the walls. The entire system is isolated.

Using the product rule of derivatives yields

$$\frac{\partial \Omega_1(N_1, E_1)}{\partial E_1} \Omega_2(N_2, E - E_1) = \Omega_1(N_1, E_1) \left. \frac{\partial \Omega_2(N_2, E_2)}{\partial E_2} \right|_{E_2 = E - E_1} . \tag{3.66}$$

Finally, by exploiting the identity $\frac{1}{y}\frac{\partial y}{\partial x} = \frac{\partial \ln y}{\partial x}$, we write

$$\frac{\partial \ln \Omega_1(N_1, E_1)}{\partial E_1} = \left. \frac{\partial \ln \Omega_2(N_2, E_2)}{\partial E_2} \right|_{E_2 = E - E_1} . \tag{3.67}$$

Consequently, For two systems in thermal equilibrium there exists a quantity which is equal in both. This quantity is the temperature T. In statistical physics it is defined by

$$\frac{1}{k_\mathrm{B} T} = \frac{\partial \ln \Omega(N, E)}{\partial E} . \tag{3.68}$$

Now, if the system N_1, V_1 is much smaller than N_2, V_2 it is safe to assume that $E_1 \ll E$. Rewriting Eq. (3.64), so that

$$P(E_1) = \frac{\Omega_1(N_1, E_1)}{\Omega(N, E)} \exp\left(\ln \Omega_2(N_2, E - E_1)\right) , \tag{3.69}$$

and expanding the exponent around E for small E_1 in a Taylor series, yields

$$P(E_1) \approx \frac{\Omega_1(N_1, E_1)}{\Omega(N, E)} \exp\left(\ln \Omega_2(N_2, E) - E_1 \frac{\partial \ln \Omega_2(N_2, E)}{\partial E}\right) , \tag{3.70}$$

$$= \frac{\Omega_1(N_1, E_1)}{\Omega(N, E)} \exp\left(\ln \Omega_2(N_2, E) - \frac{E_1}{k_\mathrm{B} T}\right) , \tag{3.71}$$

where we used Eq. (3.68) in the second step. We can eliminate the logarithm by writing

$$P(E_1) = \frac{\Omega_2(N_2, E)}{\Omega(N, E)} \Omega_1(N_1, E_1) e^{-\frac{E_1}{k_\mathrm{B} T}} . \tag{3.72}$$

Next, we introduce $Z_1 = \Omega(N, E)/\Omega_2(N_2, E)$, which denotes the canonical partition function for the system 1 and which normalizes the probability P. By omitting the subscripts we write the Boltzmann distribution

$$P(E) = \frac{\Omega(N, E)}{Z} e^{-\frac{E}{k_\mathrm{B} T}} , \tag{3.73}$$

with the canonical partition function

$$Z(N,T) = \int \mathrm{d}E\, \Omega(N,E) e^{-\frac{E}{k_\mathrm{B}T}}. \tag{3.74}$$

The factor $e^{-\frac{E}{k_\mathrm{B}T}}$ is called Boltzmann factor.

3.3.2 Properties of an ideal gas

The ideal gas is the simplest model to study equilibrium thermodynamics. It consists of N point like particles with mass m. Steric interactions between the particles can be neglected. The corresponding Hamiltonian can be written as

$$H(\mathbf{v},\mathbf{r}) = \Theta(\mathbf{r}_1,...,\mathbf{r}_N) + \sum_{i=1}^{N} \frac{m v_i^2}{2}, \tag{3.75}$$

where Θ is the potential energy. Combining the equations (3.75), (3.74) and (3.62) yields the canonical partition function

$$Z = \frac{m^{dN}}{N! h^{dN}} \int_V \mathrm{d}^{dN} r\, e^{-\frac{1}{k_\mathrm{B}T}\Theta(\mathbf{r}_1,...,\mathbf{r}_N)} \int_{-\infty}^{\infty} \mathrm{d}^{dN} v\, e^{-\frac{1}{k_\mathrm{B}T}\sum_{i=1}^{N}\frac{m v_i^2}{2}}. \tag{3.76}$$

We assume a potential Θ decomposable to the potential of individual particles such that $\Theta(\mathbf{r}_1,...,\mathbf{r}_N) = \Theta(\mathbf{r}_1) + \Theta(\mathbf{r}_2) + \cdots + \Theta(\mathbf{r}_N)$, and with

$$\Theta(\mathbf{r_i}) = \begin{cases} 0 & \text{if } \mathbf{r_i} \in V \\ \infty & \text{else} \end{cases}. \tag{3.77}$$

Both integrals can then easily be evaluated so that we obtain

$$Z = \frac{1}{N!}\left(\frac{V}{\lambda^d}\right)^N, \tag{3.78}$$

where the relation $\int_{-\infty}^{\infty} \exp(-x^2)\mathrm{d}x = \sqrt{\pi}$ has been used. The quantity $\lambda = h/\sqrt{2\pi m k_\mathrm{B} T}$ corresponds to the de Broglie wavelength of a particle with the energy $k_\mathrm{B}T/\sqrt{\pi}$.

The free energy F can be calculated from the relation [117]

$$F = -k_\mathrm{B}T \ln Z \approx -k_\mathrm{B}TN\left(\ln\frac{V}{N} + \frac{d}{2}\ln\frac{2\pi m k_\mathrm{B}T}{h^2} + 1\right), \tag{3.79}$$

where the Stirling approximation $\ln N! \approx N\ln N - N$ for large N has been used. Finally, expressions for entropy S, internal energy U and pressure p can be found. They are derived as follows [117]:

$$S = -\frac{\partial F}{\partial T} = k_\mathrm{B}\left(\ln\frac{V}{N} + \frac{d}{2}\ln\frac{2\pi m k_\mathrm{B}T}{h^2} + \frac{2+d}{2}\right), \tag{3.80}$$

$$U = F + TS = \frac{d}{2}N k_\mathrm{B}T, \tag{3.81}$$

$$p = -\frac{\partial F}{\partial V} = k_\mathrm{B}T\frac{N}{V}. \tag{3.82}$$

Equation (3.81) expresses the energy contained within the system. The Eq. (3.82) is called the equation of state for an ideal gas. It relates the state variables T, V and p to each other, which cannot be chosen independently.

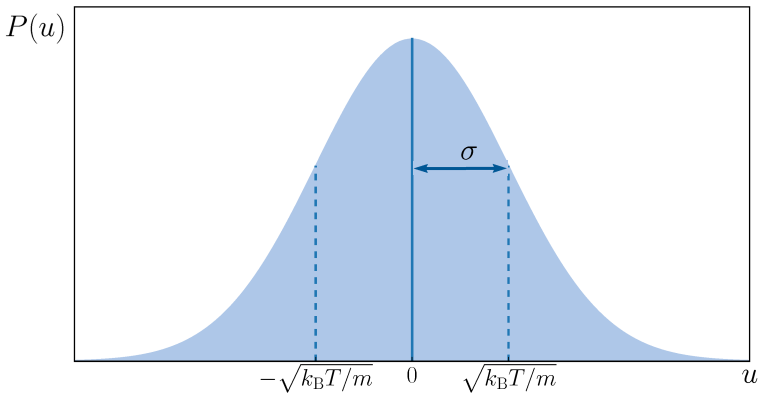

Figure 3.7: Maxwell-Boltzmann distribution for a single velocity component of a particle part of an ideal gas in a canonical ensemble with standard deviation $\sigma = \sqrt{\mathrm{Var}} = \sqrt{k_\mathrm{B}T/m}$.

From the equation of state (3.82) several useful relations can be derived, which will help to understand the properties of the fluid generated by the numerical method multi-particle collision dynamics presented in the next chapter. The isothermal compressibility β is a measure of the relative volume change in response to a pressure change. It is defined as

$$\beta = -\frac{1}{V}\frac{\partial V}{\partial p} = \frac{1}{\rho k_\mathrm{B}T}, \tag{3.83}$$

where the density $\rho = N/V$ has been substituted.

Perturbations of pressure and density propagate adiabatically with the speed of sound c. It is calculated by

$$c = \sqrt{\left.\frac{\partial p}{\partial \rho}\right|_S} = \sqrt{\frac{d+2}{d}\frac{k_\mathrm{B}T}{m}}. \tag{3.84}$$

3.3.3 Maxwell-Boltzmann distribution

Finally, we are interested in the probability of finding the velocity of a randomly picked particle to be between v and $v + \mathrm{d}v$. The probability can be calculated from the Boltzmann Eq. (3.73) for a single particle, by finding $P(\mathbf{v}) = P(E{=}mv^2/2)$. In three dimensions the partition function Ω is proportional to the volume of the spherical shell defined by the vector $\mathbf{v}$ between radius v and $v + \mathrm{d}v$. Consequently, we find $\Omega \propto 4\pi v^2 \mathrm{d}v$. The probability then reads

$$P(\mathbf{v}) \propto 4\pi v^2 e^{-\frac{mv^2}{2k_\mathrm{B}T}} \mathrm{d}v. \tag{3.85}$$

After normalization, we can write for the probability density

$$P(\mathbf{v}) = \sqrt{\frac{2}{\pi}} \left(\frac{m}{k_\mathrm{B}T}\right)^{\frac{3}{2}} v^2 e^{-\frac{mv^2}{2k_\mathrm{B}T}}, \tag{3.86}$$

which is the famous Maxwell-Boltzmann distribution. For a single velocity component u of the vector $\mathbf{v}$, the normalized probability density reads

$$P(u) = \sqrt{\frac{m}{2\pi k_\mathrm{B}T}} e^{-\frac{mu^2}{2k_\mathrm{B}T}}. \tag{3.87}$$

The distribution function is displayed in Fig. 3.7. It is a normal distribution with variance $\mathrm{Var}(u) = k_\mathrm{B}T/m$. Note that the distribution in Eq. (3.87) is valid for every Hamiltonian of the form (3.75).

3.4 Nonlinear Dynamics

To close this chapter, we introduce some useful tools which tackle nonlinear differential equations that will arise during our analytical modeling. Finding the governing differential equations of a complex system holds great predictive power. However, in most cases the equations cannot simply be solved analytically. The theory of nonlinear dynamics allows to decipher the behavior of a system of nonlinear differential equation of many degrees of freedom. We restrict this chapter to the study of two-dimensional nonlinear systems in the variables x_1 and x_2. Firstly, some general properties will be considered. Afterwards, fixed points will be defined and characterized building on our knowledge of linear systems. The section concludes with a discussion of bifurcations, which change the qualitative properties of a nonlinear system drastically by changing a single variable called the bifurcation parameter.

3.4.1 The phase portrait

The general form of an arbitrary vector field in the phase plane x_1, x_2 is

$$\begin{aligned} \frac{\mathrm{d}x_1}{\mathrm{d}z} &= f_1(x_1, x_2), \\ \frac{\mathrm{d}x_2}{\mathrm{d}z} &= f_2(x_1, x_2), \end{aligned} \tag{3.88}$$

where f_1 and f_2 are given functions. A more compact but equivalent notation is

$$\frac{\mathrm{d}\mathbf{x}}{\mathrm{d}z} = \mathbf{f}(\mathbf{x}). \tag{3.89}$$

The vector $\mathbf{x}$ represents a point in the phase plane, whereas $\mathbf{f}(\mathbf{x})$ defines a vector along changes of the variable z. Note that typically z stands for time. However, in chapter 6 we treat an example, where z becomes a space variable.

The integration of Eqs. (3.88) for a specified starting value traces out a solution $\mathbf{x}(z)$ in the phase plane. Because every point can serve as the starting value it becomes obvious that the entire phase plane is filled with trajectories. When the function $\mathbf{f}$ is nonlinear in $\mathbf{x}$, there is typically no analytical solution available. Solutions must then be found numerically using a solver for ordinary differential equations, e.g., the Runge-Kutta method [118]. Since there exist infinitely many trajectories, a complete analysis is impossible but luckily not necessary. Fixed points $\mathbf{x}_0$ of the system (3.89) can be found without great effort simply by solving $\mathbf{f}(\mathbf{x}) = 0$. Moreover, the lines defined by $f_1(x_1, x_2) = 0$ and $f_2(x_1, x_2) = 0$ correspond to zero growth lines of the respective variables. They are commonly called nullclines. These information suffice to obtain a good idea of how trajectories behave in the phase plane as displayed in Fig. 3.8 a). The presented plot is called phase portrait and a powerful tool for analyzing two dimensional nonlinear systems. In Fig. 3.8 b) some trajectories have been plotted with the aid of a Runge-Kutte integration scheme. In the following we outline some of the properties of a phase portrait. According to the existence and uniqueness theorem it can be shown that there exists a unique solution if $\mathbf{f}$ is continuously differentiable [119]. An important consequence from the existence and uniqueness theorem is that different trajectories never intersect. If several trajectories were to intersect at a point that would mean that

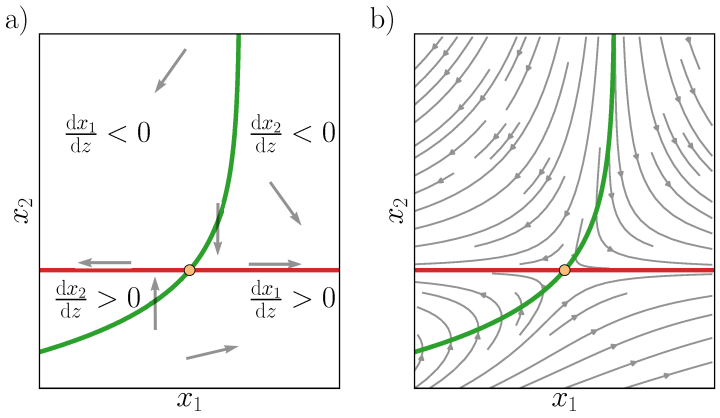

Figure 3.8: Plot of the nonlinear system $\frac{dx_1}{dz} = x_1 + e^{-x_2}$ and $\frac{dx_2}{dz} = -x_2$. The green and the red line denote the respective nullclines $\frac{dx_1}{dz} = 0$ and $\frac{dx_2}{dz} = 0$. a) Sketch of the phase portrait using only analytical considerations. The arrows indicate the flow direction. b) Plot of a few selected trajectories of the phase portrait with the aid of a numerical ODE-solver.

this point has multiple solutions, which contradicts the theorem. In two dimensions this inherits topological consequences. A trajectory starting at a point enclosed by a periodic orbit (see Sec. 3.4.3) will have to converge towards the periodic orbit at $z \to \pm\infty$ and towards a fixed point inside the orbit at $z \to \mp\infty$ as proven by the Poincaré-Bendixson theorem [120].

3.4.2 Linear stability analysis

A very useful tool to characterize fixed points of a nonlinear system is the linear stability analysis. The main idea is to approximate the nonlinear system close to the fixed points with the corresponding linear system. The system of Eqs. (3.89) can be linearized around fixed points $\mathbf{x}_0$ for which $\mathbf{f}(\mathbf{x}_0) = 0$,

$$\frac{\mathrm{d}\delta\mathbf{x}}{\mathrm{d}z} = \mathbf{A} \cdot \delta\mathbf{x} + \mathbf{O}(\delta\mathbf{x}^2), \tag{3.90}$$

where $\delta\mathbf{x} = \mathbf{x} - \mathbf{x}_0$ denotes small deviations from the fixed points. The second-rank tensor $\mathbf{A}$ is called the Jacobian matrix and defined by

$$\mathbf{A} = \left(\begin{array}{cc} \frac{\partial f_1}{\partial x_1} & \frac{\partial f_1}{\partial x_2} \\ \frac{\partial f_2}{\partial x_1} & \frac{\partial f_2}{\partial x_2} \end{array} \right) \Bigg|_{\mathbf{x}_0}. \tag{3.91}$$

Since $\delta\mathbf{x}$ is small, $\mathbf{O}(\delta\mathbf{x}^2)$ is very small and can be omitted. Equation (3.90) is a linear system, which has a general solution of the form $\mathbf{x}(z) = \mathbf{x}_0 + e^{\lambda z}\mathbf{e}$, where λ are the eigenvalues and $\mathbf{e}$ the eigenvectors of $\mathbf{A}$. In general, the eigenvalues of a matrix $\mathbf{A}$ are given by the solution of the characteristic equation $\det(\mathbf{A} - \lambda\mathbb{1}) = 0$, where "det" denotes the determinate. For a matrix $\mathbf{A} \in \mathbb{R}^2 \times \mathbb{R}^2$, the characteristic equation reduces to

$$\lambda^2 - \mathrm{trace}(\mathbf{A})\lambda + \det(\mathbf{A}) = 0. \tag{3.92}$$

The eigenvalues can then be calculated from

$$\lambda_{1/2} = \frac{\mathrm{trace}(\mathbf{A}) \pm \sqrt{\mathrm{trace}(\mathbf{A})^2 - 4\det(\mathbf{A})}}{2}. \tag{3.93}$$

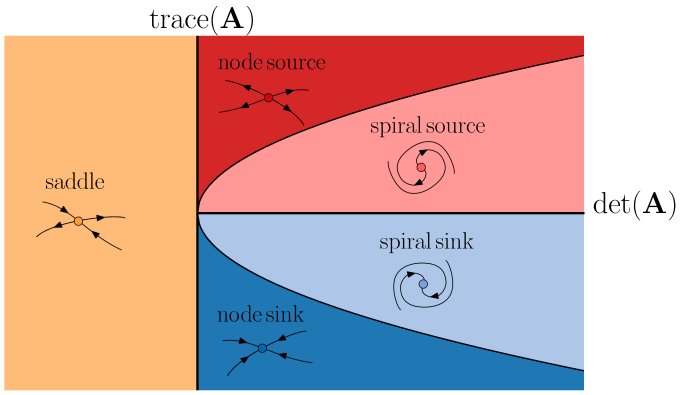

Figure 3.9: Characterization of the fixed points with respect to the trace($\mathbf{A}$) and determinate det($\mathbf{A}$). The separation line corresponds to the parabola defined by trace$(\mathbf{A})^2 - 4\text{det}(\mathbf{A}) = 0$.

From Eq. (3.93) we note that different configurations of λ_1 and λ_2 are possible. To arrive at Fig. 3.9 we make the following observations:

det($\mathbf{A}$) < 0**:** Both eigenvalues are real and have opposite signs. As a result there exist trajectories entering the fixed point as a consequence of the negative eigenvalue as well as trajectories leaving the fixed point due to the positive eigenvalue. The fixed point is then called saddle.

det($\mathbf{A}$) > 0**:** The real part of both eigenvalues are either positive for trace > 0 or negative for trace < 0. The corresponding fixed point is a node which acts as a source or a sink for the trajectories. If trace$(\mathbf{A})^2 < 4\text{det}(\mathbf{A})$, the eigenvalues are complex $\lambda \in \mathbb{C}$ and the fixed points either a spiral source or a spiral sink.

det($\mathbf{A}$) $= 0$**:** In this case at least one of the eigenvalues is zero. In the phase portrait this borderline case appears as an one-dimensional fixed point.

3.4.3 Bifurcations and limit cycles

If the dynamical system defined in Eq. (3.89) depends on additional parameters so that $\mathbf{f}(\mathbf{x}, \alpha)$, it is possible that the qualitative picture of the phase portrait changes as α is varied. In particular, fixed points can emerge, dissolve or change stability. Moreover limit cycles may appear and collide with fixed points. These qualitative changes in the behavior of the dynamic system are called bifurcations and α the corresponding bifurcation parameter.

The so called saddle-node bifurcation is the basic process during which fixed points are created or destroyed. Consider the prototypical one-dimensional system [119]

$$\frac{\mathrm{d}x}{\mathrm{d}z} = \alpha + x^2, \tag{3.94}$$

with $\alpha \in \mathbb{R}$ the bifurcation parameter. It can easily be shown that there exist two fixed points for $\alpha < 0$ and zero fixed points for $\alpha > 0$ (see Fig. 3.10). In the first case it can be tested with linear stability analysis that the fixed point in the negative half space of x is a sink whereas the other one is a source node. As α approaches 0 from the negative, the two fixed points approach each other and eventually merge at a single saddle point

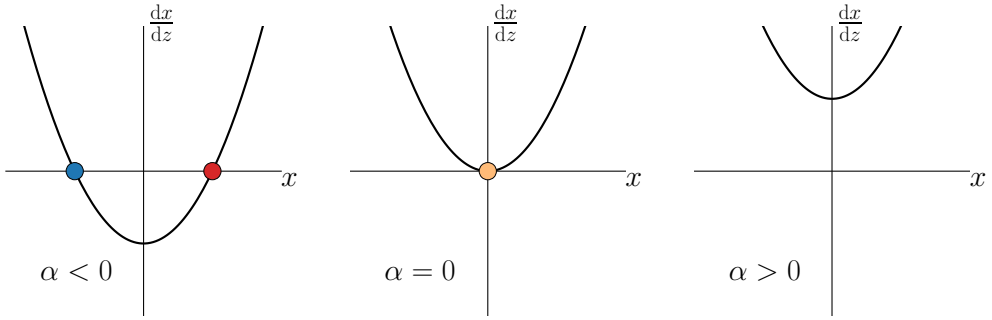

Figure 3.10: Saddle-node bifurcation of the system Eq. (3.94). The color scheme of the fixed points is the same as in Fig. 3.9.

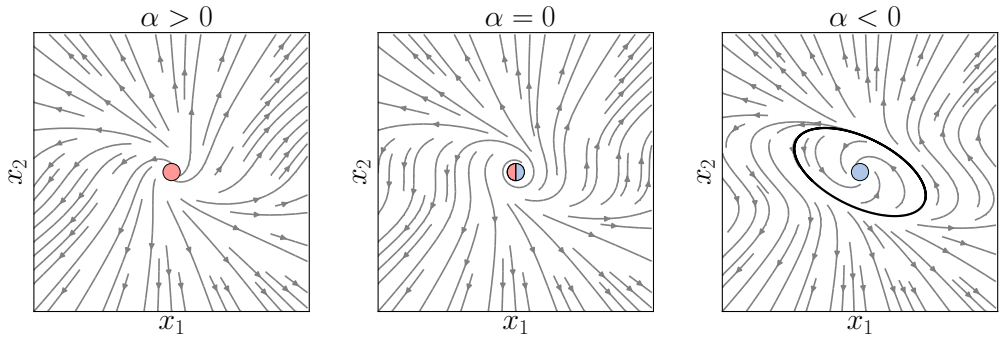

Figure 3.11: Example of a subcritical Hopf bifurcation given by the equations $\frac{dx_1}{dz} = \alpha x_1 - x_2 + x_1 x_2^2$ and $\frac{dx_2}{dz} = x_1 + \alpha x_2 + x_2^3$. At $\alpha = 0$ there is a subcritical Hopf bifurcation that leads to a growing limit cycle (black line) for $\alpha < 0$. The color scheme of the fixed points is the same as in Fig. 3.9.

as $\alpha = 0$, which vanishes as soon as $\alpha > 0$. The saddle-node bifurcation therefore occurs at $\alpha = 0$, which corresponds to crossing the line $\text{trace}(\mathbf{A}) = 0$ in Fig. 3.9.

A second way for a fixed point to switch stability by varying a bifurcation parameter α is by crossing the line $\text{trace}(\mathbf{A}) = 0$ for $\det(\mathbf{A}) > 0$ in Fig. 3.9. Please note that this is only possible when the fixed point is a spiral. Upon crossing the real parts of both eigenvalues λ change sign. This is commonly known as a Hopf bifurcation [119]. During a Hopf bifurcation a small amplitude limit cycle is either created or destroyed. A limit cycle is a closed trajectory in the phase space that corresponds to a periodic solution of a dynamic system. Limit cycles can arise in different situations.

Supercritical Hopf bifurcation: In terms of the flow in phase space, a supercritical Hopf bifurcation occurs when a spiral sink changes into a spiral source surrounded by a small amplitude limit cycle. Consequently, trajectories emerging from the fixed point approach the limit cycle.

Subcritical Hopf bifurcation: A subcritical Hopf bifurcation on the other hand occurs when a spiral source changes into a spiral sink surrounded by a small amplitude limit cycle, see Fig. 3.11. In contrast to the supercritical Hopf bifurcation, trajectories inside the limit cycle converge towards the fixed point.

The bifurcations presented so far are localized around fixed points and the qualitative changes in the phase space effect manly the neighborhood of those fixed points.

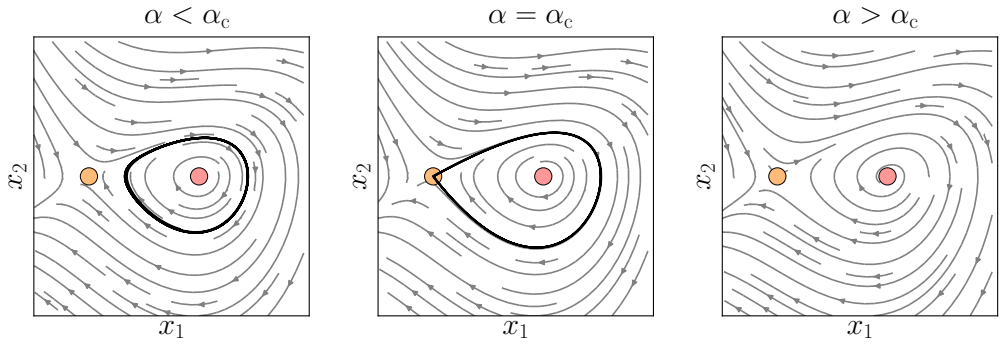

Figure 3.12: Example of a homoclinic bifurcation given by the equations $\frac{\mathrm{d}x_1}{\mathrm{d}z} = x_2$ and $\frac{\mathrm{d}x_2}{\mathrm{d}z} = \alpha x_2 + x_1 - x_1^2 + x_1 x_2$. At $\alpha_c \approx -0.8645$ the limit cycle (black line) collides with the saddle point resulting in a homoclinic orbit [119]. The color scheme of the fixed points is the same as in Fig. 3.12.

Those bifurcations are classified as local bifurcations. On the other hand, there exist also bifurcations that involve larger regions of the phase plane called global bifurcations. Given the variety of such global bifurcations we restrict this section to homoclinic bifurcation which will play a role in Chapter 6.

Homoclinic bifurcation: During a homoclinic bifurcation, a part of a limit cycle moves closer to a saddle point. At the bifurcation ($\alpha = \alpha_c$) the cycle touches the saddle point and becomes a so called homoclinic orbit (see Fig. 3.12). A homoclinic orbit has an infinite period as the trajectory approaches the saddle point at $z \to \pm\infty$. Beyond the global bifurcation ($\alpha > \alpha_c$), the limit cycle is destroyed.

4

Multi-Particle Collision Dynamics

Numerical methods arose in the second half of the last century as an indispensable tool for tackling problems too complex for analytical treatment. Nonlinear partial differential equations describe most phenomena occurring in nature and can only be solved analytically in rare cases. Instead, many numerical methods aim at discretizing the geometry and space and generate approximations of derivatives by, e.g. finite differences [121], finite elements [122, 123]. The equations can then be integrated and solutions generated at discrete points in time.

Computers can be further utilized as powerful random number generators to feed stochastic ensembles. The Monte Carlo method arose as one of the first tools using random numbers to solve deterministic problems [124]. In physics-related fields this method excels at problems having a probabilistic interpretation and with a high number of coupled degrees of freedom [125]. In the field of soft matter physics particle based simulation techniques became popular with the introduction of cellular automaton [126]. The basic algorithm is formed of particles jumping between nodes of a lattice at discrete time intervals. If two particles jump onto the same node, collision rules apply imposing mass and momentum conservation. The lattice-Boltzmann method is a generalization of this technique and solves the Boltzmann equation on a lattice by following the evolution of the single-particle probability distribution at each node [126, 127].

A lattice-free particle-based mesoscopic simulation method was introduced by Malevants and Kapral [46, 47] and named multi-particle collision dynamics (MPCD). It solves the Navier-Stokes equation on a coarse-grained level and naturally includes thermal fluctuations. MPCD is computationally fast, simple to implement, and capable of reproducing analytically known results. This includes for example the friction coefficient for a particle approaching a plane wall at distances as small as 5 % of the particle diameter [48], the flow field around a passive sphere [49], as well as the swimming velocity of a model swimmer called squirmer [50] and the torque acting on it in front of a plane wall at distances, where lubrication theory has to be applied [128]. In recent years the method has been applied to diverse problems of soft matter physics as reviewed in Refs. [51, 52]. Examples include the modeling of the flow field around passive particles [29, 55, 129] or active swimmers [53, 130–132].

The theory and implementation of MPCD for a microchannel as well as the inclusion of colloidal particles with no-slip boundary conditions will be the main task of this chapter. Moreover, two contact models between colloidal particles will be presented

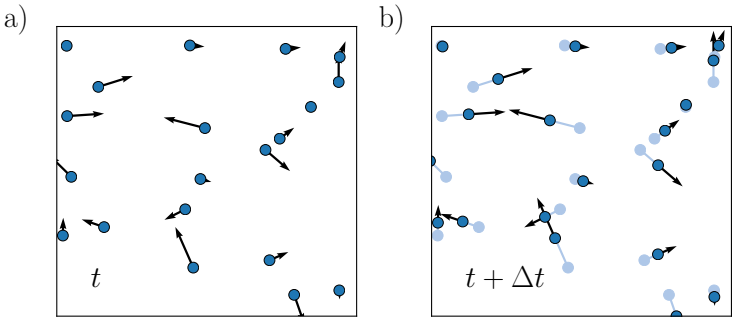

Figure 4.1: Illustrative streaming step. a) Positions before streaming. b) Updated positions after the time Δt.

and discussed. Finally, the MPCD system is mapped onto a physical system and the transport coefficients are computed for the parameters mainly used throughout this work.

4.1 Basics

A characteristic feature of some soft matter systems is the typical mesoscopic length scale, ranging from nano to micrometer. As the foregoing chapters show, thermal fluctuations becomes visible as Brownian motion on these length scales. This is mainly because the characteristic energies become comparable to the thermal energy $k_{\mathrm{B}}T$. However, length scales are still well above that of the atomic level so that quantum effects can be ignored and classical mechanics based on Newtons equations suffice to describe the system. The main difficulty in describing those systems numerically is to resolve the interplay between the molecular fluctuations and hydrodynamic forces in a fast and an efficient manner. Additionally, it is desirable that complex boundaries are easily incorporated and the implementation engineered in a way that allows for parallel execution using multiple processors. All this can be achieved by the particle based simulation method MPCD [46, 47]. A particle based approach seems rather intuitive as a real fluid does actually consist of molecules. The microscopic interactions between the molecules collectively emerge as conservations laws of mass and momentum known as Navier-Stokes equations on a macroscopic level. However, a detailed simulation along the lines of molecular dynamics proves impractical because one gram of water consists of approximately 3.3×10^{22} H_2O-molecules. This goes beyond the memory and capability of any supercomputer. Instead, in MPCD simulations typically $10^6 - 10^8$ fluid particles are used. This coarse-graining usually leads to larger thermal fluctuations, which can be interpreted as either high temperature or small characteristic length scales when mapped on a real physical system. Bearing this in mind, MPCD coarse-grains over all length and time scales. For example, the ratio of flow velocity to the speed of sound in real system is usually $\sim 10^{-9}$, whereas in MPCD the ratio is typically only $\sim 10^{-1}$. However, as long as the different time scales in the system are clearly separated the correct physics should still emerge [49].

4.1.1 The streaming step

The MPCD method makes use of point-like fluid particles of mass m, which move in a continuous space with a continuous distribution of velocities. We denote the position of

the i-th particle by $\mathbf{r}_i$ and its velocity by $\mathbf{v}_i$. Moreover, let us suppose that the particles are subject to an external force $\mathbf{F}_{\text{ext}}(\mathbf{r}, t)$. After a time interval Δt the position of the particles can be computed with the velocity Verlet algorithm [133], so that

$$\mathbf{r}_i(t + \Delta t) = \mathbf{r}_i(t) + \mathbf{v}_i(t)\Delta t + \frac{1}{2m}\mathbf{F}_{\text{ext}}(\mathbf{r}_i, t)\Delta t^2, \tag{4.1}$$

$$\mathbf{v}_i(t + \Delta t) = \mathbf{v}_i(t) + \frac{1}{2m}\left(\mathbf{F}_{\text{ext}}(\mathbf{r}_i(t), t) + \mathbf{F}_{\text{ext}}(\mathbf{r}_i(t + \Delta t), t + \Delta t)\right)\Delta t. \tag{4.2}$$

This explicit integration scheme of Newton's equation of motion provides numerical stability to second order $\mathcal{O}(\Delta t^2)$ and is frequently used in molecular dynamics simulations [134, 135].

In this thesis we only consider spatially and temporally constant external forces $\mathbf{F}_{\text{ext}}$ as generated by, e.g., a constant pressure gradient ∇p. The Eq. (4.2) then reduce to

$$\mathbf{r}_i(t + \Delta t) = \mathbf{r}_i(t) + \mathbf{v}_i(t)\Delta t + \frac{1}{2m}\mathbf{F}_{\text{ext}}\Delta t^2, \tag{4.3}$$

$$\mathbf{v}_i(t + \Delta t) = \mathbf{v}_i(t) + \frac{1}{m}\mathbf{F}_{\text{ext}}\Delta t. \tag{4.4}$$

Please note that Eq. (4.3) and (4.4) are exact, rendering the integration scheme unconditionally stable. During the streaming step the positions of all particles are updated according to Eq. (4.3) and (4.4) and as illustrated in Fig. 4.1. Interactions between particles are not considered within the streaming step, which makes it very fast.

4.1.2 The collision step

The novelty of MPCD stems from its collision step. A collision between particles occurs at discretely spaced time steps Δt. The fluid particles do not sterically collide. Instead, particles are grouped in boxes with edge length b similar to that shown in Fig. 4.2 a). Only particles assigned to the same box interact and exchange momenta.

Various mechanisms have been proposed to execute the collision step [136–139], most notably stochastic rotation dynamics [46] and Anderson thermostat [136, 137]. The former is characterized by random rotations of the relative velocities $\delta\mathbf{v}_i = \mathbf{v}_i - \mathbf{u}$, where $\mathbf{u}$ is the mean velocity of all the particles in one box. The latter samples random velocities from a Gaussian distribution and assigns them to each fluid particle after the collision. The requirements for the collision rule in both realizations are the same: collisions must conserve momentum and be statistically independent for different boxes and at different times. We use the implementation of the Anderson thermostat, which updates the velocities of a fluid particle according to [137]

$$\mathbf{v}_i' = \mathbf{u} + \mathbf{v}_i^{\text{ran}} - \frac{1}{N_{\text{b}}}\sum_{j\in\text{box}}\mathbf{v}_j^{\text{ran}}, \tag{4.5}$$

where $\mathbf{v}'$ denotes the velocity after the collision (see Fig. 4.2). The sum on the right hand side is over all particles N_{b} inside the same box and ensures that the total momentum of the box does not change. The mean velocity inside a box is computed from $\mathbf{u} = \sum_{j\in\text{box}}\mathbf{v}_j/N_{\text{b}}$. The random velocities $\mathbf{v}^{\text{ran}}$ are sampled from a Maxwell-Boltzmann distribution with variance $k_{\text{B}}T/m$ (compare Section 3.3.3), which acts as a thermostat and classifies the simulations as performed in a canonical ensemble [136]. In our implementation the random numbers are generated by a Ziggurat algorithm [140].

Normally, Eq. (4.5) produces a shift of the angular momentum that is computed from

$$\Delta\mathbf{L} = m\sum_{i\in\text{box}}\mathbf{r}_i \times (\mathbf{v}_i' - \mathbf{v}_i). \tag{4.6}$$

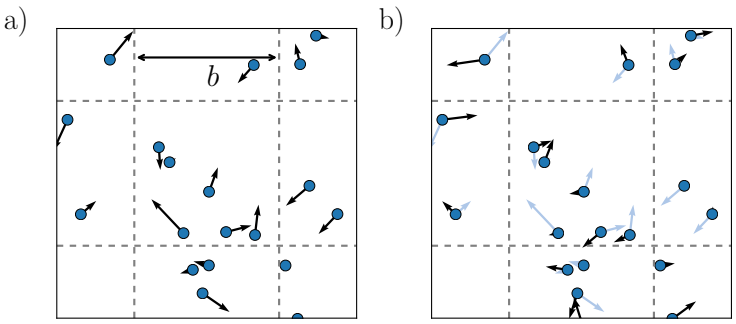

Figure 4.2: Illustrative collision step. a) Discretization of the domain in equally spaced boxes with width b, which assign fluid particles to collision groups. b) After the execution of the collision step the velocities are updated and momentum is conserved.

Angular momentum conservation can be added by imposing constraints on the new relative velocities [137, 141]. Adding a correction velocity $\mathbf{v}'' = \mathbf{v}' + \mathbf{v}_i^{\mathrm{cor}}$ to each particle and demanding

$$\Delta\mathbf{L} + m \sum_{i \in \mathrm{box}} \mathbf{r}_i \times \mathbf{v}_i^{\mathrm{cor}} = 0, \tag{4.7}$$

angular momentum can be restored. With the relations

$$\mathbf{v}_i^{\mathrm{cor}} = \boldsymbol{\omega}^{\mathrm{cor}} \times (\mathbf{r}_i - \mathbf{r}_c) \tag{4.8}$$

and

$$\Delta\mathbf{L} = \mathbf{I} \cdot \boldsymbol{\omega}^{\mathrm{cor}}, \tag{4.9}$$

where $\mathbf{r}_{\mathrm{c}} = \sum_{j \in \mathrm{box}} \mathbf{r}_j / N_{\mathrm{b}}$ denote the box's center of mass and

$$\mathbf{I} = m \sum_{j \in \mathrm{box}} \left((\mathbf{r}_i - \mathbf{r}_{\mathrm{c}})^2 - (\mathbf{r}_i - \mathbf{r}_{\mathrm{c}}) \otimes (\mathbf{r}_i - \mathbf{r}_{\mathrm{c}}) \right), \tag{4.10}$$

the moment of inertia tensor, the post collision velocities finally read

$$\mathbf{v}_i'' = \mathbf{v}_i' + m\mathbf{I}^{-1} \cdot \sum_{j \in \mathrm{box}} \left[(\mathbf{r}_j - \mathbf{r}_{\mathrm{c}}) \times (\mathbf{v}_j - \mathbf{v}_j^{\mathrm{ran}}) \right] \times (\mathbf{r}_j - \mathbf{r}_{\mathrm{c}}). \tag{4.11}$$

The velocities $\mathbf{v}''$ generated by Eq. (4.11) now successfully conserve translational and angular momentum within the boxes.

If the parameters are chosen such that $\langle |\mathbf{v}| \rangle \Delta t \ll b$, usually due to low temperatures or small time steps, the particles interact repeatedly with the same collision partners inside the same box before diffusing the distance b. This poses a problem as the algorithm in this form is not Galilean invariant [142]. In other words, if particles interact with the same collision partners over multiple collision steps, their velocities are correlated and retain information of previous encounters. In a homogeneously imposed flow field V, where $V\Delta t \simeq b$, these correlations are absent.

It was shown that the Galilean invariance can be remedied by performing a random shift of the box grid before each collision [142, 143]. With $\mathbf{x}_{\mathrm{b}}$ the origin of the box grid, the grid shift is implemented by performing $\mathbf{x}_{\mathrm{b}} + \delta\mathbf{x}$, where the components of $\delta\mathbf{x}$ are generated from the uniform distribution in the interval $[-b/2, b/2]$. The implementation of the grid shift ensures that independent of homogeneously imposed flow, constantly new groups of collision partners are formed.

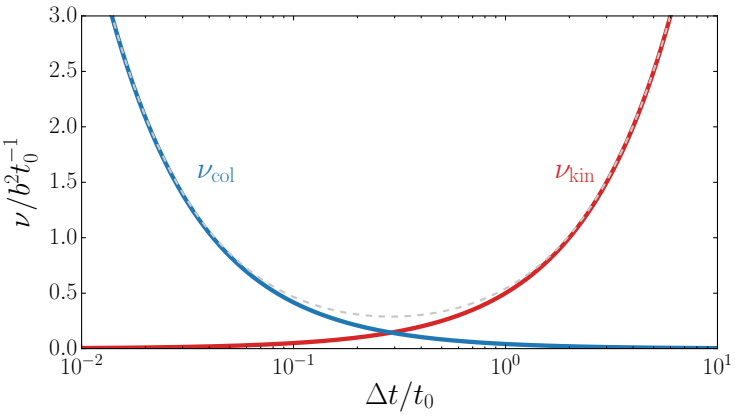

Figure 4.3: Analytical predictions of the contributions to the net viscosity generated by a MPCD simulation for large n, with angular momentum conservation and $t_0 = \sqrt{m/k_{\mathrm{B}}Tb}$. The dashed grey line denotes the sum $\nu_\nu = \mathrm{kin} + \nu_{\mathrm{col}}$.

4.1.3 Static and dynamic properties

The link between microscopic dynamics and macroscopic properties was shown in section 3.3 for an ideal gas in a canonical ensemble. For large numbers of particles N, the streaming step in MPCD with Maxwell-Boltzmann distributed velocities clearly generates a kinetic contribution to the pressure that obeys the same equation of state as Eq. (3.82), namely

$$p = k_{\mathrm{B}}T\frac{n}{b^d}, \tag{4.12}$$

where n denotes the average number of fluid particles per box. We saw that properties like speed of sound c [Eq. (3.84)], as well as isothermal compressibility β [Eq. (3.83)], can be derived from the equation of state. These properties play an important role when choosing the parameters for the simulation. In contrast to a Newtonian fluid, the fluid produced by MPCD is compressible, so it is crucial that density fluctuations travel much faster than the fluid itself.

The collision step does not contribute to the hydrostatic pressure but generates shear stress. With the assumption of molecular chaos and for large enough n, it can be shown that the streaming and collision step account for the following contributions of the kinematic shear viscosity [144, 145]

$$\nu_{\mathrm{kin}} = \frac{k_{\mathrm{B}}T\Delta t}{m}\left(\frac{n}{n-(d+2)/4} - \frac{1}{2}\right) \quad \text{and} \tag{4.13}$$

$$\nu_{\mathrm{col}} = \frac{b^2}{24\Delta t}\left(\frac{n-7/5}{n}\right). \tag{4.14}$$

Figure 4.3 plots the kinematic and collisional viscosity for various step sizes Δt. The figure shows that high viscosities can be produced for either very large or small time steps Δt. From the perspective of numerical efficiency, large time steps are desirable. However, this implies that the dynamics are dominated by kinematic effects, i.e., the streaming step. In consequence, when using large time steps the MPCD fluid behaves more like a gas than a liquid because the corresponding mean free streaming step $\lambda = \Delta t\sqrt{k_{\mathrm{B}}T/m}$ of the particles is large. Instead and in order to avoid the local minimum in Fig. 4.3, usually small time steps $\Delta t/t_0 \sim 10^{-2} - 10^{-1}$ are chosen, where $t_0 = \sqrt{m/k_{\mathrm{B}}Tb}$, so that collisions dominate the momentum exchange [49].

In conclusion, the method conserves momentum and generates hydrostatic and shear stress. On length scales larger than both, the box size b and the mean free path λ of the fluid particles as well as on time scales larger than the collision time Δt the method successfully solves the Navier-Stokes equation (3.6) [51]. Moreover, thermal fluctuations are included by implication, which makes the solver a powerful tool in understanding mesoscopic phenomena, where hydrodynamics and diffusion are important.

4.2 Implementation of Passive Particles and the Channel

The previous section introduced the MPCD method, which simulates a Newtonian fluid. For most real applications it is necessary for the fluid to interact with swimming and stationary objects. The fluid should not penetrate suspended objects and interact in a way such that the no-slip boundary condition is recovered (see Sect. 3.1.2). Moreover, in Chapter 2 we presented experiments and simulations from literature, which put forward the claim that colloidal particles in dense suspensions do come in contact with each other despite the repulsive lubrication. We introduce here two models of implementing passive particles, which were utilized to simulate frictional contacts between colloids as well as between colloids and walls.

4.2.1 Implementation of the no-slip boundary condition

In the following the implementation of impenetrable, solid bodies into the MPCD fluid is presented. As discussed in Sect. 3.1.2, the fluid assumes the velocity of the body directly at its surface. In order to achieve this, both the streaming and the collision step must be adapted accordingly.

During the streaming step it must be checked whether a particle has penetrated the surface of a solid body [see Fig. 4.4 a)]. If so, the bounce-back rule is applied in order to enforce the no-slip boundary condition [146]. We restrict the discussion to movable spherical objects of mass M and radius R. The rules for collisions with walls can be derived accordingly. For the fluid particle, the bounce back rule reads

$$\mathbf{v}_i' + \mathbf{v}_i = 2\left(\mathbf{u} + \boldsymbol{\omega} \times (\mathbf{r}_i - \mathbf{r}_\mathrm{c})\right), \tag{4.15}$$

where $\mathbf{v}_i'$ is the updated velocity of the fluid particle after the collision and $\mathbf{u}$ and $\boldsymbol{\omega}$ denote translational and angular velocity of the sphere with $\mathbf{r}_\mathrm{c}$ its center of mass. After the collision the change of momentum $\Delta\mathbf{p}_i = m(\mathbf{v}_i - \mathbf{v}_i')$ is transfered to the sphere to conserve momentum and angular momentum such that

$$\mathbf{u}' = \mathbf{u} - \frac{1}{M}\Delta\mathbf{p}_i, \tag{4.16}$$

$$\boldsymbol{\omega}' = \boldsymbol{\omega} - \frac{1}{I}\left(\mathbf{r}_i - \mathbf{r}_\mathrm{c}\right) \times \Delta\mathbf{p}_i, \tag{4.17}$$

where I is the moment of inertia of the sphere. In three dimensions it takes the value $I^{3\mathrm{D}} = \frac{2}{5}MR^2$ and in two dimensions $I^{2\mathrm{D}} = \frac{1}{2}MR^2$, respectively. Note that the kinetic energy after the collision is only conserved in the limit $m \ll M$, which can be accepted due to the use of a thermostat in the collision step (see Sect. 4.1.2).

To accurately resolve when, where and in what order fluid particles collide with objects is numerically expensive. The following alternative was proposed by Padding *et al.* [147]. All particles are moved according to Eq. (4.3) and (4.4) during the time step Δt. Secondly, all particles, which penetrated solid objects are moved backwards for a half time step $\Delta t/2$ and then placed closest on the surface of the object. To effectively retrieve such penetrating particles, neighbor lists are used, which greatly improve performance

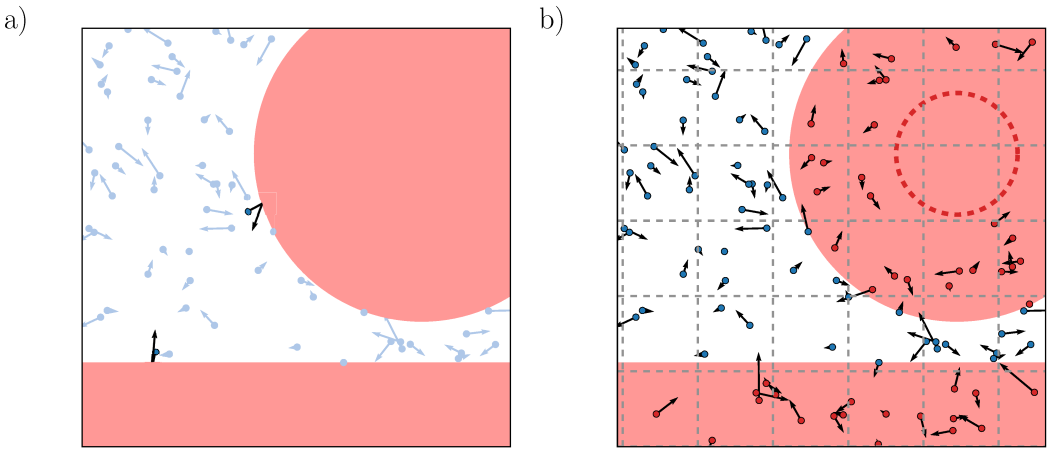

Figure 4.4: Schematic example of solid objects immersed in the MPCD fluid. a) During the streaming step, particle collisions with objects are checked and velocities redirected according to Eq. (4.15). b) During the collision step ghost particles (red) are generated inside the solid objects, which undergo collisions among themselves as well as with real MPCD particles in the solvent.

[148]. The velocity of the fluid particle is then updated according to Eq. (4.15) and the particle propagated forward for the time $\Delta t/2$. In our implementation it is possible for a fluid particle to undergo multiple collisions during one streaming step, e.g., when located inside a narrow gap between two spheres. Those collisions are then identically resolved each time the particle penetrates into a boundary but with a halved time step $\Delta t/2^i$, where i denotes the i-th collision.

During the collision step, the collision cells can overlap with the spheres as in Fig. 4.4 b). So called "ghost" particles have been proposed to deal with this issue [29, 146, 149]. Ghost particles are generated at equal density n at the end of each streaming step and participate in the collision step and also exchange momentum. The implementation of ghost particles has various benefits. They ensure that hydrostatic and hydrodynamic properties close to solid objects are conserved on the box level because the average number n of fluid particles inside overlapping boxes is recovered. In addition, ghost particles enforce the no-slip boundary condition by having the same mean velocity as the solid. Ghost particles are generated with the velocity

$$\mathbf{v}_\mathrm{g} = \mathbf{u} + \boldsymbol{\omega} \times (\mathbf{r}_\mathrm{g} - \mathbf{r}_\mathrm{c}) + \mathbf{v}^\mathrm{ran}. \tag{4.18}$$

Here, $\mathbf{v}^\mathrm{ran}$ is again drawn from a Maxwell-Boltzmann distribution [Eq. (3.87)] and $\mathbf{r}_\mathrm{g}$ is the randomly assigned location of the ghost particle inside the solid. Please note that the ghost particles need only be generated up to a depth of $b\sqrt{d}$ into the solid to be able to interact with real fluid particles as indicated in Fig. 4.4 b). After the collision, the momentum changes of the ghost particles are conveyed to the spheres according to Eq. (4.16)-(4.17).

4.2.2 Event-driven molecular dynamics

One of the method to resolve the contact interactions between hard and elastic spheres is event-driven molecular dynamics. The name stems from the integration scheme, which jumps forward in time until an event, i.e., a collision with another object occurs and

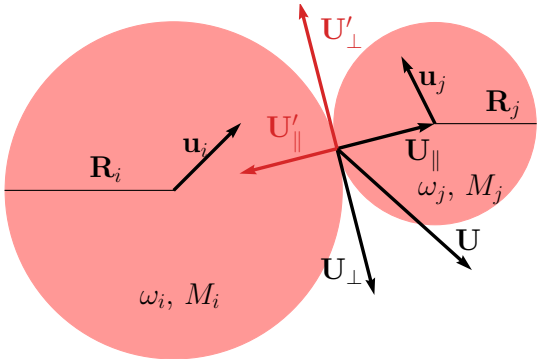

Figure 4.5: Schematic view of the collision of two unequal spheres i and j with relative velocity $\mathbf{U}$ at the point of contact. Upon collision $\mathbf{U} \to \mathbf{U}'$ the parallel part $\mathbf{U}_\parallel$ and perpendicular part $\mathbf{U}_\perp$ reverse in order to prevent slip.

resolves momentum exchanges instantaneously before jumping to the next event. Thus, our main challenge is to determine the ordered sequence of sphere collisions.

During the streaming step the spheres move ballistically with their current velocities to a new location given by

$$\mathbf{r}_i(t + \Delta t_{\mathrm{MD}}) = \mathbf{r}_i(t) + \mathbf{u}_i(t)\Delta t_{\mathrm{MD}}, \tag{4.19}$$

where $\Delta t_{MD} \leq \Delta t$ is the molecular dynamics time step, which denotes the time until the next collision between two spheres and $\mathbf{r}_i$ is the center of mass of the i-th sphere. Let a pair of spheres be denoted by (i,j) and let us define

$$R_{ij} = R_i + R_j, \tag{4.20}$$
$$\Delta\mathbf{r}_{ij} = \mathbf{r}_c^i - \mathbf{r}_c^j, \tag{4.21}$$
$$\Delta\mathbf{u}_{ij} = \mathbf{u}_i - \mathbf{u}_j, \tag{4.22}$$
$$b_{ij} = \Delta\mathbf{r}_{ij} \cdot \Delta\mathbf{u}_{ij}, \tag{4.23}$$
$$k_{ij} = b_{ij}^2 - \Delta u_{ij}^2(\Delta r_{ij}^2 - R_{ij}^2). \tag{4.24}$$

For the pairs (i,j) that fulfill $b_{ij} < 0$, i.e., pairs that move towards each other, as well as $k_{ij} > 0$, i.e., pairs that come within collision range $r_{ij} < R_{ij}$ of each other, the time Δt_{MD} until the next collision is calculated from [150]

$$\Delta t_{\mathrm{MD}} = \min\left(-b_{ij} - \frac{\sqrt{k_{ij}}}{\Delta u_{ij}^2}\right)_{\forall i,j,i\neq j}. \tag{4.25}$$

Equation (4.25) can be used to build a priority queue of future events ordered by time. For numerical efficiency the implementation of Eq. (4.25) also uses neighbor lists [148].

Upon collision the relative velocity at the point of contact is calculated from

$$\mathbf{U} = \Delta\mathbf{u}_{ij} - \frac{1}{R_{ij}}\left(\boldsymbol{\omega}_i R_i + \boldsymbol{\omega}_j R_j\right) \times \Delta\mathbf{r}_{ij}, \tag{4.26}$$

which can be decomposed in a parallel part $\mathbf{U}_\parallel = (\mathbf{U}\cdot\mathbf{n})\mathbf{n}$ and perpendicular part $\mathbf{U}_\perp = \mathbf{U} - \mathbf{U}_\parallel$, with $\mathbf{n} = \Delta\mathbf{r}_{ij}/R_{ij}$ as displayed in Fig. 4.5. Assuming no losses due to friction, the parallel component $\mathbf{U}_\parallel$ reverses. When modeling the no-slip boundary

condition, the perpendicular component $\mathbf{U}_\perp$ must reverse as well. With momentum, angular momentum, and energy conservation, the momentum exchange $\Delta\mathbf{p}$ is computed from

$$\Delta\mathbf{p} = -2M_{ij}\left(\mathbf{U}_\parallel + \frac{\mathbf{U}_\perp}{1 + M_{ij}/I_{ij}}\right), \tag{4.27}$$

with reduced mass and reduced moment of inertia

$$M_{ij} = \frac{M_i M_j}{M_i + M_j} \quad \text{and} \tag{4.28}$$

$$I_{ij} = \frac{I_i I_j}{R_i^2 I_j + R_j^2 I_i}. \tag{4.29}$$

Finally, the velocities and angular velocities of the spheres can be updated according to

$$\mathbf{u}_i' = \mathbf{u}_i + \frac{1}{M_i}\Delta\mathbf{p}, \tag{4.30}$$

$$\mathbf{u}_j' = \mathbf{u}_j - \frac{1}{M_j}\Delta\mathbf{p}, \tag{4.31}$$

$$\boldsymbol{\omega}_i' = \boldsymbol{\omega}_i - \frac{R_i}{R_{ij} I_i}\Delta\mathbf{r}_{ij} \times \Delta\mathbf{p}, \tag{4.32}$$

$$\boldsymbol{\omega}_j' = \boldsymbol{\omega}_j - \frac{R_j}{R_{ij} I_j}\Delta\mathbf{r}_{ij} \times \Delta\mathbf{p}. \tag{4.33}$$

As spheres collide and change their direction, some events scheduled on the priority queue become invalidated. As a result, collisions involving the spheres i and j must be updated and inserted onto the priority queue. Eqs. (4.25)-(4.19) are executed consecutively until the time Δt has passed and the MPCD collision step is performed. During the collision and streaming step momentum exchanges with the fluid are transfered to the spheres so that Eq. (4.25) must be reinitialized every time before the next event driven molecular dynamics step.

4.2.3 Linear spring model with friction

The second model we will use to resolve the interactions between the spheres is the linear spring model. A direct consequence of this is that spheres and walls become "soft", i.e., can be penetrated by other spheres. The degree of softness is determined by a repulsion potential, which needs to be steep enough to model nearly hard spheres. This scheme excels in very dense sphere packings, where many collisions occur and when compared to the event-driven molecular dynamics, where the priority queue must be constantly initialized and updated. Moreover, the spring model is easily parallelized whereas the event driven model can only be executed chronologically. Another difference is that with the linear spring model several contacts between spheres are simultaneous possible, which allows the occurrence of force chains and jamming.

In contrast to event driven molecular dynamics, this method discretizes the time in equidistant time steps $\Delta t_{\mathrm{MD}} \leq \Delta t$ and integrates the positions and velocities between the MPCD collision steps using the Euler method. Consequently, instead of instantaneously resolved momentum exchanges, this scheme uses forces $\mathbf{F}$ and torques $\mathbf{T}$ that describe the steric repulsion between the spheres and the momentum exchange with the fluid. The latter is generated by adding together interactions from the MPCD streaming

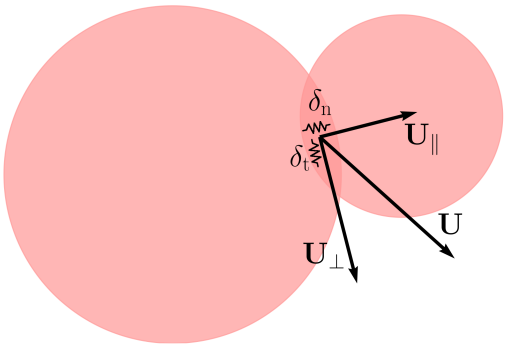

Figure 4.6: Schematic view of two spheres in contact with relative velocity $\mathbf{U}$ at the point of contact. The springs denote tangential $\boldsymbol{\delta}_\mathrm{t}$ and normal spring $\boldsymbol{\delta}_\mathrm{t}$.

and collision step with the i-th colloid and reads

$$\mathbf{F}_i^\mathrm{hyd} = -\frac{1}{\Delta t}\left(\sum_\mathrm{stream.} \Delta\mathbf{p}_j + \sum_\mathrm{coll.} \Delta\mathbf{p}_j\right), \tag{4.34}$$

$$\mathbf{T}_i^\mathrm{hyd} = -\frac{1}{\Delta t}\left(\sum_\mathrm{stream.} (\mathbf{r}_j - \mathbf{r}_i)\times\Delta\mathbf{p}_j + \sum_\mathrm{coll.} (\mathbf{r}_j - \mathbf{r}_i)\times\Delta\mathbf{p}_j\right). \tag{4.35}$$

The integration of positions and velocities of the spheres is then conducted by computing

$$\mathbf{r}_i(t+\Delta t) = \mathbf{r}_i(t) + \mathbf{u}_i(t)\Delta t, \tag{4.36}$$

$$\mathbf{u}_i(t+\Delta t) = \mathbf{u}_i(t) + \frac{\Delta t_\mathrm{MD}}{M_i}\left(\mathbf{F}_i^\mathrm{hyd} + \mathbf{F}_i(t)\right), \tag{4.37}$$

$$\boldsymbol{\omega}_i(t+\Delta t) = \boldsymbol{\omega}_i(t) + \frac{\Delta t_\mathrm{MD}}{I_i}\left(\mathbf{T}_i^\mathrm{hyd} + \mathbf{T}_i(t)\right). \tag{4.38}$$

The forces $\mathbf{F}_i(t) = \sum_{j\neq i}^{N} \mathbf{F}_{ij}(\mathbf{r}_i(t), \mathbf{r}_j(t))$ and torques $\mathbf{T}_i(t) = \sum_{j\neq i}^{N} T_{ij}(\mathbf{r}_i(t), \mathbf{r}_j(t))$ depend on positions and relative angles of all spheres at the time t. However, in our implementation the sum over all spheres N is greatly reduced with the aid of neighbor lists [148]. The forces between pairs are treated with a model commonly used in granular physics [59, 151].

When a sphere overlaps with another body, it experiences a repulsive spring force $\mathbf{F}_\mathrm{n} = -k_\mathrm{n}\boldsymbol{\delta}_\mathrm{n}$, where k_n is the spring constant (see Fig. 4.6). The vector $\boldsymbol{\delta}_\mathrm{n}$ measures the overlap distance and always points towards the collision partner along the normal vector $\mathbf{n}$ of both colliding surfaces. While in contact, the relative displacement $\boldsymbol{\delta}_\mathrm{t}$ in tangential direction $\mathbf{t} \perp \mathbf{n}$ results in an elastic force $\mathbf{F}_\mathrm{t} = -k_\mathrm{t}\boldsymbol{\delta}_\mathrm{t}$ and torque $\mathbf{T} = R\mathbf{n}\times\mathbf{F}_\mathrm{t}$, where k_t is the tangential spring constant. The frictional force generated by the tangential shift $\boldsymbol{\delta}_\mathrm{t}$ depends on the relative rotation of both spheres and requires special treatment. When contact is established the tangential overlap $\boldsymbol{\delta}$ is incremented by computing

$$\boldsymbol{\delta}_\mathrm{t}(t+\Delta t_\mathrm{MD}) = \boldsymbol{\delta}_\mathrm{t}(t) + \mathbf{U}_\perp(t)\Delta t_\mathrm{MD}, \tag{4.39}$$

where $\mathbf{U}_\perp$ again denotes the tangential relative velocity of both spheres. To prepare the next iteration, one has to rotate the tangential spring into the actual tangential plane,

since the frame of reference of the contact may have rotated by updating the positions of the spheres. This correction is done by

$$\boldsymbol{\delta}_{\mathrm{t}}^{\mathrm{new}} = f[\boldsymbol{\delta}_{\mathrm{t}}^{\mathrm{old}} - \mathbf{n}(\mathbf{n} \cdot \boldsymbol{\delta}_{\mathrm{t}}^{\mathrm{old}})], \tag{4.40}$$

where the length of $\boldsymbol{\delta}_{\mathrm{t}}$ is preserved by an appropriate scaling factor f. We employ Coulomb's law of friction

$$|\mathbf{F}_{\mathrm{t}}| \leq \mu |\mathbf{F}_{\mathrm{n}}|, \tag{4.41}$$

with μ the dimensionless friction coefficient. As soon as the tangential force $|\mathbf{F}_{\mathrm{t}}|$ exceeds the value of $\mu|\mathbf{F}_{\mathrm{n}}|$, the particles start sliding and the tangential spring is adjusted to a length consistent with Coulomb's condition, so that

$$\boldsymbol{\delta}_{\mathrm{t}}(t + \Delta t_{\mathrm{MD}}) = -\frac{1}{k_{\mathrm{t}}} \mu |\mathbf{F}_{\mathrm{n}}(t)| \mathbf{t}(t). \tag{4.42}$$

In the simulation the spring constants k_{n} and k_{t} should be tuned such that the overlaps $\delta_{\mathrm{n}} \ll R$ and $\delta_{\mathrm{t}} \ll R$ are small compared to the sphere size in order to resemble nearly hard spheres.

4.3 Mapping between the Physical and Coarse-Grained System

The ultimate goal of our MPCD implementation is to correctly describe physical phenomena observed in experiments. For a coarse-grained solver such as MPCD it is important to include all the time and length scales relevant to a colloidal suspension. However, correctly resolving the relaxation time of a fluid molecule $\tau_{\mathrm{f}} \approx 10^{-14}$s as well as the diffusive time $\tau_{\mathrm{D}} \approx 10^{0}$s of a colloidal particle, requires a simulation to distinguish between durations separated by 14 orders of magnitude. Here, compromises must be made. Nevertheless, a successful mapping is possible and profits from expressing the physical properties of interest in dimensionless parameters such as the Reynolds number, Mach number, Péclet number, and Schmidt number.

Schmidt number

When modeling a liquid it is important that the momentum transport within the fluid is dominated by inter-particle collisions rather than by kinematics. This is best quantified by the Schmidt number

$$\mathrm{Sc} = \frac{\nu}{D_{\mathrm{f}}}, \tag{4.43}$$

where D_{f} is the fluid particle self-diffusion coefficient and proportional to $D_{\mathrm{f}} \propto \Delta t$ [152]. For a gas, momentum transport is mainly governed by mass diffusion so that $\mathrm{Sc} \approx 1$, while for larger Schmidt numbers $\mathrm{Sc} \gg 1$ the dynamics shows collective behavior reminiscent of that of a liquid. In MPCD this can only be achieved by choosing small time steps Δt, which simultaneously ensures large viscosities ν and a small self-diffusion coefficients D_{f}. In our simulations the Schmidt number is typically $\mathrm{Sc} \gtrsim 25$, which is sufficient for the problems we study.

Mach number

The Mach number measures the ratio

$$\mathrm{Ma} = \frac{v}{c}, \tag{4.44}$$

between the speed of the solvent or colloidal flow v and the speed of sound c. The Mach number measures compressibility effects [153] and in contrast to the Schmidt number directly depends on the flow velocity. The speed of sound in water at room temperature measures $c \approx 1481\text{m/s}$ and is by far not attainable as flow speed in micro flow experiments. As a consequence, under normal conditions the solvent can be safely assumed as incompressible. On the other hand, to mimic a fluid with equal density, the coarse grained solver MPCD uses a much lower number density of fluid particles with much higher masses m. This implies that the speed of sound c is much lower in the coarse grained system, which is calculated from Eq. (3.84). There exists evidence that compressibility effects typically scale with Ma^2 [153], so that for most applications it is sufficient to limit the simulations to $\text{Ma} \lesssim 0.2$ [49].

In our implementation we set $k_\text{B}T = 1$ and $m = 1$, so that the speed of sound calculated from Eq. (3.84) is $c^{2\text{D}} \approx 1.41b/t_0$ in two dimensions or $c^{3\text{D}} \approx 1.29b/t_0$ in three, respectively. Consequently, when running a simulation, it is always checked that the flow speed v_0 in the center of the channel does not exceed $v_0 \lesssim 0.2c$ to minimize compressibility effects.

Reynolds number

The Reynolds number has been discussed in chapter 2 and 3. It measures the relative strength of inertial forces when compared to viscous forces. For a particle it is defined by

$$\text{Re}_a = \frac{va}{\nu}, \tag{4.45}$$

where we denote by a the radius of a suspended colloid.

We can also define a channel Reynolds number for the flow through the channel with width w

$$\text{Re}_w = \frac{v_0 w}{\nu_\text{bulk}}, \tag{4.46}$$

where v_0 denotes the maximum velocity in the center. We emphasize that the bulk viscosity ν_bulk is a sensitive function of the colloidal packing fraction ϕ. In the conducted simulations we typically use dense suspensions with packing fractions $\phi > 0.30$ so that usually $\nu_\text{bulk} \gg \nu$.

In real-world experiments on microfluidic flow, Re does typically not exceed 10^{-4}, rendering inertial forces insignificant. In order to keep Re small in a MPCD simulation, one must either choose small particle sizes a or w, or use small flow velocities v. The former are limited by discretization effects occurring at $a \lesssim 2b$ [49]. Since simulation time is important we aim on having large flow velocities v that do not violate $\text{Ma} \lesssim 0.2$ and are still well within the Stokes regime. To simulate Stokes flow the parameters are typically chosen to keep $\text{Re} \lesssim 0.2$ [49].

Péclet number

Finally, the Péclet number compares convective transport to diffusive transport. A colloidal particle of radius a in flow of speed v diffuses the distance of its radius after the time $\tau_D = a^2/D$, with D the self-diffusion coefficient of the colloid. It is transported by flow over the same distance after the time $\tau_v = a/v$. The Péclet number is then calculated by

$$\text{Pe} = \frac{\tau_D}{\tau_v} = \frac{va}{D}. \tag{4.47}$$

Brownian fluctuations are expected to be less important if $\text{Pe} \gg 1$. In this regime hydrodynamics is dominant and MPCD generates data that is less noisy. When studying

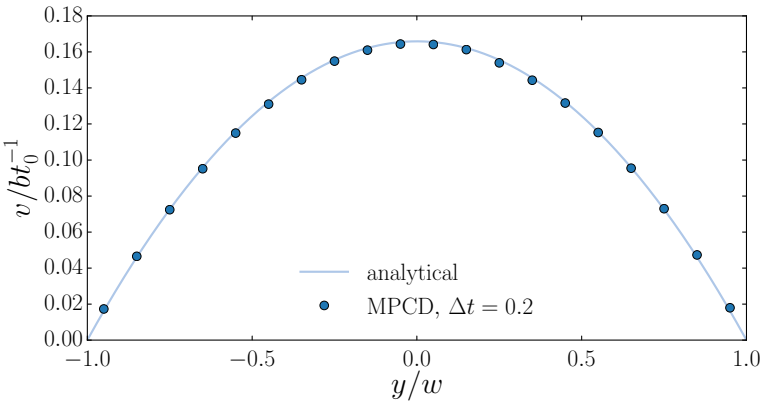

Figure 4.7: Parabolic flow between two infinite plates generated by MPCD in three dimensions using following parameters: $n = 10$, $\Delta t = 0.2$, $\sigma = 0.001$ and $w = 10b$. For comparison the analytical result is displayed using the predicted viscosity calculated from Eq. (4.13) and (4.14).

non-equilibrium phenomena the Péclet number is typically large, e.g. $\mathrm{Pe} \approx 50 - 500$ in the experiment on shear-induced size segregation [58].

In MPCD, Pe can be tuned by varying the flow speed v, which is however restricted by limitations given by Re and Ma number. Increasing the size a of the particle is numerically expensive when keeping the ration a/w constant and simultaneously increases the particle Reynolds number Re_a. Another way to increase Pe is to decrease the diffusion coefficient D defined by the Einstein relation Eq. (3.53). This is best be done by increasing the number density n of fluid particles per collision box. In consequence, the dynamic viscosity η increases and the colloid interacts with a larger number of fluid particles, which reduces fluctuations and thus its diffusivity.

4.4 Transport Coefficients

Now that we have established the frame conditions to model microfluidic flow with the aid of MPCD, we want to confirm the analytically known result for channel flow (see Sect. 3.1.3) in absence of colloidal particles. This setup together with Eq. (3.27) can then be used to exactly measure the viscosity ν of the fluid for various parameters. Secondly, we want to measure the diffusion coefficient D of suspended particles inside an open box. For this purpose we numerically integrate the velocity autocorrelation function introduced in Sect. 3.2.3.

4.4.1 Computation of viscosity

In Sect. 3.1.3 we saw that a constant pressure gradient $\sigma = |\boldsymbol{\nabla} p|/\rho$ along a channel with walls separated by the distance $2w$ generates a Poiseuille flow that obeys

$$v(y) = \frac{\sigma}{2\nu}(w^2 - y^2), \tag{4.48}$$

with the maximum velocity $v_0 = \sigma w^2/2\nu$ in the center of the flow. We can confirm the parabolic flow profile in Fig. 4.7 using our implementation. Also, a good quantitative agreement is obtained when compared to the analytical known result of the Navier-Stokes equation (4.48) using the viscosity predicted by Eq. (4.13) and (4.14). In this

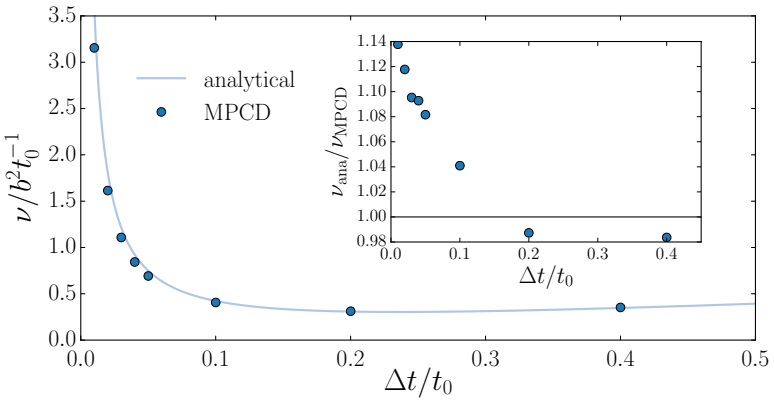

Figure 4.8: Measurement of the viscosity of a MPCD fluid in three dimensions for various time step lengths Δt and for $n = 10$. For comparison the analytical result is displayed using the predicted viscosity calculated from Eq. (4.13) and (4.14). The inset shows the relative deviation between analytical and measured viscosities.

setup we can measure the viscosity of the MPCD fluid by generating a Poiseuille flow and measuring the velocity v_0 in the center of the channel. Then, by rewriting Eq. (4.48) we find

$$\nu_{\mathrm{MPCD}} = \frac{\sigma w^2}{2v_0}. \tag{4.49}$$

In Fig. 4.8 we compare the measured viscosities ν_{MPCD} to the analytical prediction $\nu_{\mathrm{ana}} = \nu_{\mathrm{kin}} + \nu_{\mathrm{col}}$ and also display the ratio $\nu_{\mathrm{ana}}/\nu_{\mathrm{MPCD}}$. We notice that for small Δt the viscosity increases, which is desirable for our application. When compared with the analytical prediction ν_{ana} the ratio $\nu_{\mathrm{ana}}/\nu_{\mathrm{MPCD}}$ becomes larger for smaller time steps up to 14% for $\Delta t = 0.01$. In doing so, the analytical predictions overestimates the MPCD viscosity. The reason for this is the unmet assumption of molecular chaos, which was made when deriving Eq. (4.13)-(4.14). For small Δt, fluid particles interact with neighboring fluid particles over several consecutive collision steps due to their small mean free path, even though grid shift is enabled. This causes correlations similar to those experienced by stochastic rotation dynamics [139, 154]. Taking this into account, we measure the viscosity directly by utilizing Eq. (4.49) for all our simulations.

4.4.2 Diffusion coefficient

In order to estimate the Péclet number for colloids in flow, we need to know the diffusion coefficient D. To calculate the diffusion coefficient with the aid of the Einstein relation Eq. (3.53), requires knowledge of the friction coefficient ζ, which depends on viscosity and in two dimensions even on the Reynolds number (see Sect. 3.1.5). To avoid uncertainties, the diffusion coefficient D is best directly computed from either the mean square displacement at large times like in Eq. (3.47) or more elegantly with the velocity autocorrelation function introduced in Sect. 3.2.3, which is defined by

$$C(\tau) = \langle \mathbf{v}(t) \cdot \mathbf{v}(t+\tau) \rangle. \tag{4.50}$$

The diffusion coefficient is then found by integrating over τ [compare with Eq. (3.52)], so that [99, 115]

$$D = \frac{1}{d} \int_0^\infty \mathrm{d}\tau \, C(\tau). \tag{4.51}$$

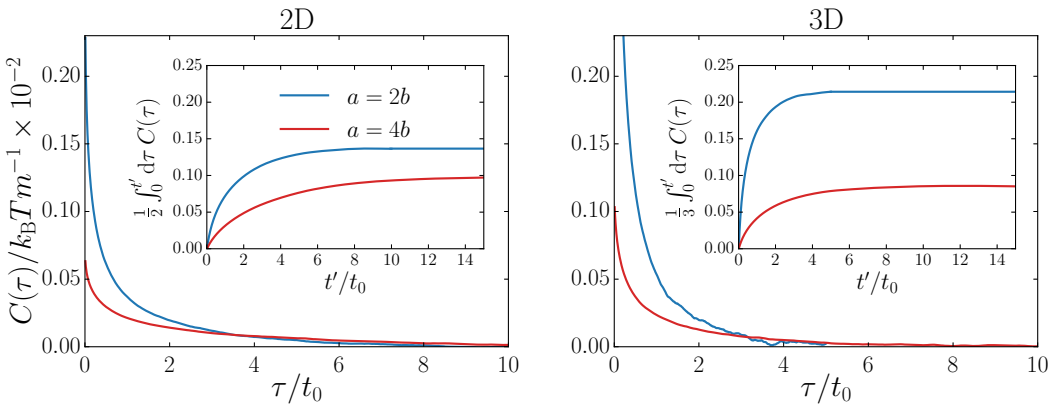

Figure 4.9: Velocity autocorrelation function for a single particle of size $2b$ and $4b$ in a periodic box of length $l = 20a$ in two ($n = 50$) and three ($n = 10$) dimensions with time step $\Delta t = 0.01$. The inset shows the integration of the function with respect to the upper integration limit t'.

In Fig. 4.9 the velocity autocorrelation functions are shown for a single colloid suspended in a bulk MPCD fluid with periodic boundary conditions in all spatial dimensions and length of $l = 20a$. We compute the velocity autocorrelation function for colloids of size $a = 2b$ and $a = 4b$ as well as in two and in three dimensions. The velocity autocorrelation function completely decays and its integration displayed in the inset saturates after approximately $t \approx 15t_0$. After this time the colloids have completely lost memory of their initial velocity. By assuming $D(t' = 15t_0) \approx D(t' = \infty)$, the diffusion coefficients can be taken off the insets of Fig. 4.9. For larger colloids, D is smaller in two and three dimensions. In three dimensions the ratio between the diffusion coefficient for radius $2b$ and $4b$ is roughly 2 as predicted by the Stokes formula (3.32) together with the Einstein relation (3.53). In two dimensions the translational friction ζ, determined in Eq. (3.36), exhibits only weak dependence on the size of the sphere. This is attributed to the infamous Stokes paradox (Sect. 3.1.5). In Fig. 4.9 left, the paradox is reflected by a lower ratio of D for differently sized spheres.

4.5 Parallelization with Open-MP

OpenMP is an application programming interface for shared memory multiprocessing [155, 156]. It consists of a set of compiler directives and library routines that allow to access and use multiple cores of a processor during run time. OpenMP is well suited for parallelizing loops, for which the individual iterations are independent of each other. The tasks are then divided among multiple so-called threads, for which each corresponds to a single processor core. The sequential part of the code is executed by a master thread, which forks into multiple threads just before a parallel region is entered as can be seen in Fig. 4.10. When all the iterations within the parallel region are completed, the master thread leads to the next parallel region while the remaining threads are on stand by.

In the implementation used throughout this work, parallel regions are used around the streaming and collision step. The streaming step is treated within a *for*-loop over all fluid particles executing the steps described in Sect. 4.1.1. When using OpenMP, the single iterations of the loop are dynamically distributed over all available threads. Similarly, the positions and velocities of the colloids are updated within a parallelized *for*-loop. The colloidal interactions are computed pairwise so that the i-th colloid needs

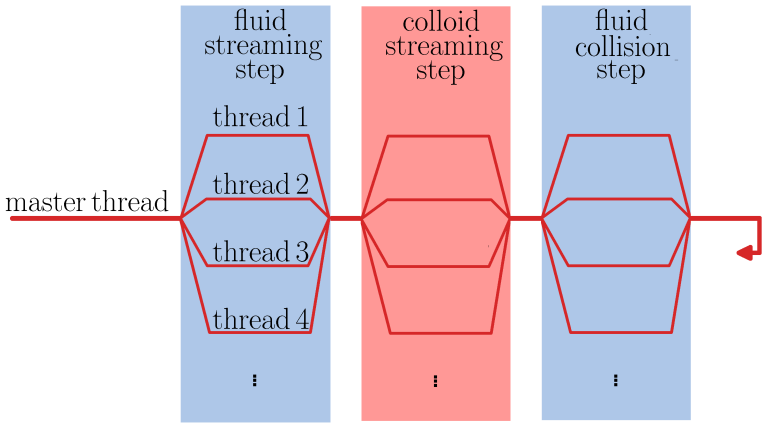

Figure 4.10: Schematic representation of the parallelization of the program code during one iteration step. The master thread computes the serial part of the program and forks into multiple threads when entering a parallelized region.

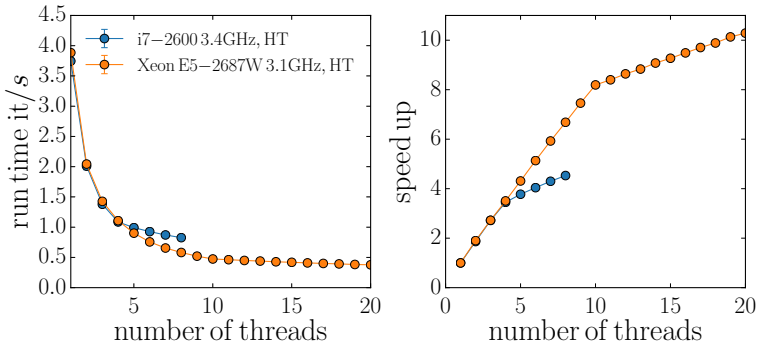

Figure 4.11: Benchmark of two processors using OpenMP with respect to the number of threads. Hyper threading (HT) is enabled. Left: runtime for one iteration of simulating a periodic channel of length $l = 12000b$, width $2w = 50b$, fluid density $n = 25$ and 21886 suspended colloids using the linear spring model in two dimensions. Right: relative speedup when compared to the run time of only one single thread.

only to check for collisions with partners j, for which $j > i$ holds. To ensure that multiple threads do not simultaneously write on the same memory block, locks are used, which allow access of designated memory address only one at a time. Each thread generates random numbers from a different pseudo random number generator of periodicity 2^{128}. Experience has shown that the streaming and collision step of the MPCD fluid require approximately 95% of the runtime. Consequently, most optimization has been dedicated towards the respective program parts.

In Fig. 4.11 we check run time and speed up of our MPCD realization with respect to the number of utilized threads. We consider two processors architectures, which have been used throughout this work to simulate colloidal flow. The first is an Intel core i7 clocked with 3.4GHz and 8MB cache memory. The processor has 4 physical cores and supports hyper threading (HT). HT generates for each physical core two virtual cores, which share the workload in parallel applications if possible. This is especially useful when much memory needs to be shifted meanwhile one physical core would stay idle. The second processor is a Xeon E5 with 10 physical cores (HT) at 3.1GHz and with 30MB cache. The first processor type was mainly used to generate results presented in

this thesis.

A theoretical perfect parallelization would result in a linear increase of the speedup over number of threads with a slope equal to 1. In reality this is of course impossible to attain as some program parts remain to be executed in serial and threads might be waiting for each other to finish. Nonetheless, we find for both processor types under consideration a clear linear behavior with slope ≈ 0.82 up to a number of threads equal to the number of physical cores. For larger number of threads, HT still generates a speed up equal to a slope of ≈ 0.2. As a result, our implementation of MPCD benefits from HT as with 4 physical cores a speed up of roughly ≈ 4.5 and with 10 physical cores a speed up of roughly ≈ 10.3 can be achieved.

5 Hydrodynamic Segregation in a Bidisperse Colloidal Suspension

The results presented in the following chapter are based on the publication [A].

In this chapter we finally want to put our implementation of MPCD to use in order to validate the results against experimental data and obtain further insight into the governing physics. In chapter 2, we presented experiments showing that colloids in dense suspension exhibit shear-induced migration towards regions of low viscous shear attributed to irreversible binary particle interactions [21–23, 64]. Inside a microchannel this area is the channel center, which accumulates particles [24–27]. Moreover, in dense bidisperse colloidal suspensions under pressure driven flow it was shown that the same mechanism leads to a segregation of large particles towards the center of a microchannel and the suspension partially demixes [58].

To develop a more thorough theoretical understanding of these effects we present results on hydrodynamic segregation in binary colloidal dispersions using MPCD. As argued in the previous chapter, this method is very suitable for simulating micron sized particles in flow because it combines the effects of hydrodynamic interactions and thermal motion.

For reasons of numerical efficiency most of the simulations for the parameter studies were conducted in two dimensions. However, in section 3.1.5 it was shown that the hydrodynamic friction coefficient ζ_{drag} in two dimensions depends only weakly on particle size a, in contrast to linear in three dimensions. This undoubtedly effects the qualitative diffusive behavior in polydispersed suspensions when comparing two and three dimensions. In this chapter a binary suspension of particles with size ratio two is used. Consequently, for some parameters simulations were conducted in three dimensions in order to not overlook the effect of spatial dimensionality on the results.

Additionally, a phenomenological model for the particle currents based on the work of Leighton and Acrivos [64] and Phillips et al. [22] is formulated. Using a single fit parameter for the collective diffusivity of the colloids, this theory predicts steady-state density profiles across the channel. Firstly, this theory will be evaluated against profiles generated by monodisperse suspensions and secondly against profiles generated by binary suspensions. A detailed parameter study on how Péclet number and density composition of the two species affect the steady-state density profiles will be presented and discussed.

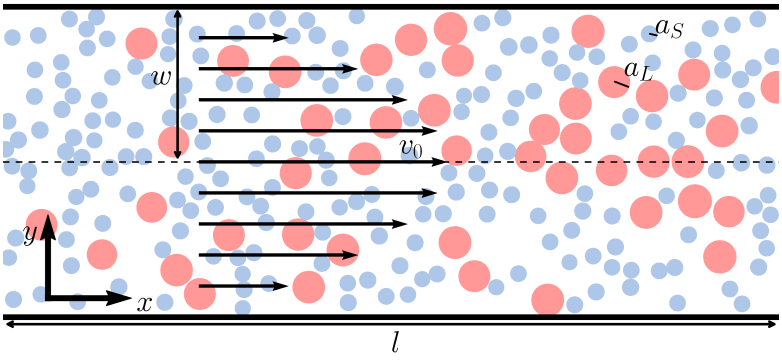

Figure 5.1: Channel geometry of width $2w$ and length l. Channel walls are at $y/w = 1$ and $y/w = -1$ and periodic boundary conditions in x-direction apply. A pressure driven Poiseuille flow with flow speed v_0 in the center is initiated. A bidisperse colloidal suspension develops a non-uniform density profile and distorts the parabolic flow profile. For three-dimensional channels also periodic boundary conditions in z-direction apply.

5.1 Setup and Parameters

We know from Sect. 2.1 that colloids move at vanishing Reynolds numbers. In order to mimic a highly viscous fluid with multi-particle collision dynamics we need to set a small collision time step (see Fig. 4.3). In our simulations the time step between collisions was chosen to be as small as $\Delta t = 0.01 t_0$, with $t_0 = \sqrt{mb^2/k_\mathrm{B}T}$ in two and three dimensions. In this regime, momentum exchange is mainly governed by the collision step, which yields a liquid like character [49] and simulations are performed in the Stokes regime at low Reynolds numbers, such that $\mathrm{Re} = v_0 \rho w/\eta$ does not exceed ca. 0.2. Here w is half the channel width and v_0 is the maximum velocity of the Poiseuille flow generated by a constant pressure gradient ∇p along the channel (see Fig. 5.1). To evaluate Re, the bulk viscosity η of the dense colloidal suspensions simulated in this work has been used. The channel walls obey the no-slip boundary condition and are implemented according to Sect. 4.2.1.

The average fluid particle number density is $\rho = 10/b^3$ in 3D, and $\rho = 50/b^2$ in 2D. Single colloidal spheres and disks performing Brownian motion in the fluid have roughly the same diffusion coefficients D with these parameters, since the number of fluid particles interacting with the colloid is roughly the same, $2\pi a \rho_{2\mathrm{D}} \approx 4\pi a^2 \rho_{3\mathrm{D}}$.

Interactions between colloids within the suspensions are resolved using the event driven molecular dynamics simulation introduced in Sect. 4.2.2. This method treats the colloids as hard and generates elastic collisions without slip that conserve energy and translational as well as angular momentum following Ref. [157]. This direct colloid-colloid contact but also thermal motion break the kinematic reversibility of the Stokes equations and enable cross-streamline migration in our simulations.

The Péclet number $\mathrm{Pe} = v_\mathrm{D} a/D$ introduced in Sect. 2.1, quantifies the relevance of the thermal motion of a colloid of radius a compared to its drift motion with velocity v_D. From the phenomenological model proposed by Leighton and Acrivos [64] (Eq. 2.3 in Sect. 2.2) we can roughly estimate the drift velocity in the lateral channel direction as $v_0 a^2/w^2$ so that the Péclet number used in the following becomes

$$\mathrm{Pe} = \frac{a^3}{w^2}\frac{v_0}{D}\,. \tag{5.1}$$

To initiate a simulation, binary mixtures of neutrally buoyant colloidal particles with

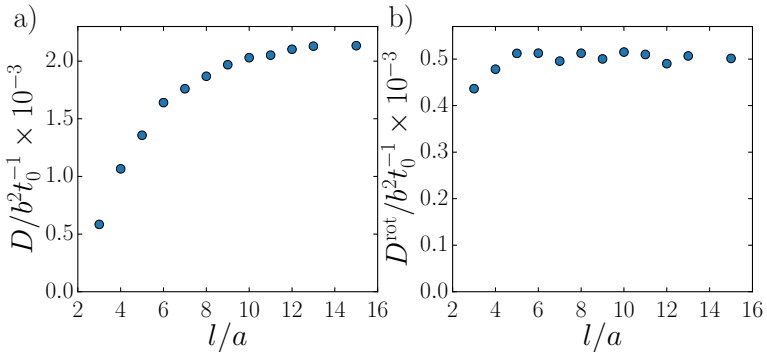

Figure 5.2: a) Translational and b) rotational diffusion coefficient for a single colloid in a periodic cubic box of length l computed with aid of the velocity autocorrelation function (see Sect. 4.4.2). Particle size is $a = 2b$, time step $\Delta t = 0.01t_0$ and density $\rho = 10m/b^3$.

respective mean radii a_S for the small and a_L for the large particles are placed inside the microchannel with an initial homogeneous distribution as displayed in Fig. 5.1. The colloidal radii for both species are generated from respective narrow Gaussian distributions with standard deviations $\sigma_i = 0.02a_i$ with $i = L, S$ in order to prevent crystallization. A pressure gradient implemented by a constant force acting on each fluid particle then drives the solvent out of equilibrium and the steady-state concentration profile of the colloids are monitored. Periodic boundary conditions apply in flow direction as well as in z-direction for the three-dimensional case to mimic the large channel aspect ratio of the experiments reported in Ref. [58].

We always choose the channel half width w as $w = 20a_S$. The length of a two-dimensional channel is $l = 100a_S$ and for three-dimensional channels $l = 20a_S$. In the latter case, the height of the simulation box along the z-direction typically is $h = 20a_S$. Periodic boundaries produce infinite mirror images of colloidal particles at distance $\pm l$, $\pm 2l$, etc., which may cause finite size effects. In order to show that the finite size effects generated by relatively short channel in three dimensions are negligible, we plot translational and rotational diffusion coefficient D and D^{rot} for a single colloid inside a periodic cubic box of length l in Fig. 5.2. Finite size effects are strong for small l especially for translational diffusion but reach a constant value at roughly $l \gtrsim 10a$. Rotational diffusion reaches a constant value at much smaller box sizes.

All parameters and transport coefficients in MPCD units are summarized in table 5.1.

In order to determine smooth density and velocity profiles along the y-axis from discrete colloidal values, we employed kernel density estimation using Epanechnikov kernel functions [158] $k(y)$. Summation over all colloids N yields a smooth lateral profile.

$$F(y) = \sum_{i=1}^{N} f_i k_i(y) = \sum_{i=1}^{N} f_i \frac{3}{4\epsilon^3} \left(\epsilon^2 - (y - y_i)^2\right) H(\epsilon - |y - y_i|) \tag{5.2}$$

Here H is the Heaviside step function. To evaluate the respective density or velocity profiles, one takes for f_i either $1/N$ or the velocity component v_x^i of particle i. For the kernel width we chose $\epsilon = 0.005w$ so that packing effects were clearly resolved. Densities of the large and small particles were determined by replacing N by their respective numbers N_L and N_S. Finally, to obtain the final profiles, time averages of $F(y)$ were taken after the system had reached steady state.

The number of colloidal disks in the two-dimensional case spans between 200 and

parameter	2D	3D
m	1	1
b	1	1
$k_\mathrm{B}T$	1	1
Δt	$0.01t_0$	$0.01t_0$
ρ	$50m/b^2$	$10m/b^3$
a_S	$2b$	$2b$
a_L	$4b$	$4b$
w	$40b$	$40b$
l	$200b$	$40b$
ν	$3.22b^2/t_0$	$3.15b^2/t_0$
D_S	$0.00137b^2/t_0$	$0.00214b^2/t_0$
D_L	$0.000973b^2/t_0$	$0.000852b^2/t_0$

Table 5.1: Overview of the MPCD simulation parameters and transport coefficients in units of fluid-particle mass m, collision box length b, and temperature $k_\mathrm{B}T$ for the simulations in two and three dimensions.

600 with up to 8×10^5 fluid particles. In the three-dimensional channel the number of colloidal spheres varies between 200 and 1000 with up to 1.2×10^6 fluid particles in a single simulation. Given the generally slow dynamics of shear-induced migration, we use the program interface OpenMP (see Sect. 4.5) to execute simulations on 4 to 8 Intel i7 cpu cores (HT) simultaneously.

5.2 Phenomenological Theory

We now develop a phenomenological theory to describe shear-induced segregation of bidisperse colloidal suspensions in a Poiseuille flow. As reviewed in Sect. 2.2, such a segregation cannot be explained by purely hydrodynamic forces due to the kinematic reversibility of the governing Stokes equations. In a careful study Leighton and Acrivos proposed surface roughness and the resulting irreversible particle interactions, as they call them, as the major cause for the observed shear migration [19]. They developed an understanding for the resulting particle drift motion, which was put into a phenomenological theory by Phillips *et al.* [22] and later generalized by Pesche *et al.* [85] to bidisperse suspensions with a large size difference between the two particle species. In the following we review the main ideas for the phenomenological theory and develop our own approach for bidisperse suspensions in order to explain our numerical results.

Two colloids in a Poiseuille flow either form bound states or during collision move on swapping trajectories where they exchange their lateral positions [159]. When moving on different sides of the centerline, they even perform cross-swapping trajectories where the center of mass just crosses the centerline [159]. However, real shear-induced migration does not occur. According to Leighton and Acrivos [19], to observe migration towards lower shear rate $\dot{\gamma} := |\partial v_x/\partial y|$, two colloidal particles have to encounter in an irreversible collision, where they move away from each other. So they perform cross-streamline displacements of the order of particle size a. The frequency of collisions in a sheared suspension with volume fraction $\phi := V_\mathrm{sph}c$ scales with $\phi\dot{\gamma}$. Here, c is the number particle density and V_sph the volume of a sphere or the area of a disk. Now, the collision frequency across the particle radius varies as $a\nabla\phi\dot{\gamma}$ and colloids migrate towards regions of low shear rate with a drift velocity v_D proportional to $-a^2\nabla(\phi\dot{\gamma})$.

Furthermore, the shear viscosity is a sensitive function of density. As a result, one can show that in a spatially varying viscosity field, the displacements towards a region of higher viscosity are smaller [19]. So the effective displacement in an irreversible collision scales as $a^2\nabla\eta/\eta$. Together with the collision frequency this gives a drift velocity v_D proportional to $-a^2\phi\dot{\gamma}\nabla\eta/\eta$.

5.2.1 Monodisperse suspension

Based on the above arguments, Phillips *et al.* formulated the constitutive equation for the particle current J as the sum of drift (ϕv_D) and diffusional currents:

$$J = -\phi\left(K_c a^2\nabla(\phi\dot{\gamma}) + K_\eta a^2\phi\dot{\gamma}\frac{\nabla\eta}{\eta}\right) - D_\mathrm{C}\nabla\phi \tag{5.3}$$

In the following, we only consider one-dimensional shear migration in y-direction and ∇ then means $\partial/\partial y$. The positive phenomenological parameters K_c and K_η are of order one and can be obtained in experiments and simulations. The last term on the right-hand side describes thermal collective diffusion and D_C is the collective diffusivity, also referred to as down-gradient diffusivity. Typically, close to the channel walls the shear rate $\dot{\gamma}$ is large and dominates over collective diffusion, whereas at the centerline $\dot{\gamma}$ is zero and also D_C becomes important. We will use this to make predictions for the density profile at the channel walls and around the centerline.

In steady state, $J = 0$ and using $\nabla\eta = \nabla\phi\partial\eta/\partial\phi$, Eq. (5.3) can be rewritten as

$$\phi^2 K_c a^2\nabla\dot{\gamma} = -\left[\phi\dot{\gamma}a^2\left(K_c + K_\eta\phi\frac{1}{\eta}\frac{\partial\eta}{\partial\phi}\right) + D_\mathrm{C}\right]\nabla\phi. \tag{5.4}$$

The term on the left side drives shear migration by transporting particles from regions of high shear to low shear rate. All terms on the right side effectively are diffusion terms and tend to homogenize the density profile but with different significance across the channel width. We identify two regions with different governing terms.

Close to the wall: $\phi\dot{\gamma}a^2 \gg D_\mathrm{C}$

In the vicinity of the wall the terms in Eq. (5.4) linear in $\dot{\gamma}$ dominate over D_C and Eq. (5.4) becomes

$$\phi\nabla\dot{\gamma} \approx -\dot{\gamma}\nabla\phi - \frac{K_\eta}{K_c}\phi\dot{\gamma}\frac{\nabla\eta}{\eta}. \tag{5.5}$$

This equation can directly be integrated using $\nabla f/f = \nabla\ln f$. We arrive at an implicit equation for the lateral profile of the particle density, written here for positive y,

$$\frac{\phi(y)}{\phi(w)} = \frac{\dot{\gamma}(w)}{\dot{\gamma}(y)}\left(\frac{\eta(\phi(w))}{\eta(\phi(y))}\right)^{\frac{K_\eta}{K_c}}, \tag{5.6}$$

with $\phi(w)$ and $\dot{\gamma}(w)$ evaluated directly at the wall. In the Poiseuille flow $\dot{\gamma}$ decreases away from the wall and thereby drives a particle current towards the centerline so that ϕ increases. The accompanying increase in viscosity initiates a particle current towards the wall, which ultimately stabilizes the density profile. To see this behavior in Eq. (5.6), we rewrite it as

$$\dot{\gamma}(y)\phi(y)\eta(\phi(y))^{K_\eta/K_c} \equiv \text{const.} \tag{5.7}$$

The density ϕ always has to increases towards lower shear rate, since η is a monotonically increasing function in ϕ.

Close to the channel center: $\phi\dot{\gamma}a^2 \ll D_\mathrm{C}$

Now, collective thermal diffusion in Eq. (5.4) becomes the leading term close to the channel center for two reasons. First, the shear rate approaches zero at $y = 0$ and second, the collective diffusion constant D_c increases with colloidal density, especially near random close packing [160]. So, Eq. (5.4) approximates the density gradient as

$$\nabla\phi \approx -K_c a^2 \phi^2 \frac{\nabla\dot{\gamma}}{D_\mathrm{C}}. \tag{5.8}$$

Since $\nabla\phi \propto -\nabla\dot{\gamma}$, we again find an enrichment of particles in the low-shear region, only this time balanced by collective thermal diffusion.

In summary, in the steady state of a monodisperse suspension, the particle density or volume fraction ϕ increases monotonically away from the channel walls towards the centerline in the direction of decreasing shear rate $\dot{\gamma}$. Since the shear rate is zero in the channel center, here the highest concentration occurs.

5.2.2 Extension to a bidisperse suspension

We generalize the phenomenological theory to a bidisperse colloidal suspension with particle radii a_1 and a_2. The shear-induced drift velocity resulting from collisions between particles of the same type i is determined as before, only the radius and volume fraction are replaced by the respective quantities for species i, a_i and ϕ_i. Particles of different type also collide and we expect the resulting drift velocity of species i to be written as

$$v_D^{(i)} = A_{ij}[K_c\nabla(\phi_j\dot{\gamma}) + K_\eta\phi_j\dot{\gamma}\nabla\eta/\eta]\,, \tag{5.9}$$

where Einstein's convention for summing over repeated indices is used. The coupling matrix $\mathbf{A}$ contains geometrical factors, which for collisions between particles of the same type are $A_{ii} = a_i^2$, as before.

For collisions between particles of different type, we argue as follows. The frequency, with which a colloid of type i colloids with a colloid of type j is proportional to $\dot{\gamma}$ times the number of type-j colloids in the collision volume $\propto(a_i + a_j)^d$. Therefore,

$$f_{ij} \propto c_j\dot{\gamma}(a_i + a_j)^d \propto \phi_j\dot{\gamma}\left(1 + \frac{a_i}{a_j}\right)^d, \tag{5.10}$$

where we used $c_j a_j^d \propto \phi_j$. At the instant of a collision, the colloids are separated by the distance $a_i + a_j$ and they rotate about the common center of mass [19], with respective distances l_i and l_j from the particle centers, which obey

$$l_i a_i^d = l_j a_j^d\,. \tag{5.11}$$

The distance Δd_i that particle i migrates during an irreversible collision scales like l_i,

$$\Delta d_i \propto l_i = l_i\frac{a_i + a_j}{l_i + l_j} = \frac{a_i + a_j}{1 + \left(\frac{a_i}{a_j}\right)^d}\,, \tag{5.12}$$

where we used Eq. (5.11). Now, the collision frequency along the y direction varies as $(a_i + a_j)\nabla f_{ij}$ giving rise to the drift velocity $v_D^i \propto \Delta d_i(a_i + a_j)\nabla f_{ij}$. Comparison with Eq. (5.9) then allows to identify the components of the coupling matrix $\mathbf{A}$ as

$$A_{ij} = \frac{(a_i + a_j)^2}{2^{d+1}}\frac{\left(1 + \frac{a_i}{a_j}\right)^d}{1 + \left(\frac{a_i}{a_j}\right)^d}. \tag{5.13}$$

The denominator 2^{d+1} is introduced in order to have $A_{ii} = a_i^2$ as in the monodisperse case.

Now, Eq. (5.3) can be generalized to obtain an expression for the particle current J_i of type i as the sum of drift ($\phi_i v_D^{(i)}$) and diffusional currents:

$$J_i = -\phi_i A_{ij} \left(K_c \nabla(\phi_j \dot{\gamma}) + K_\eta \phi_j \dot{\gamma} \frac{\nabla \eta}{\eta} \right) - D_{\mathrm{C}}^{ij} \nabla \phi_j. \tag{5.14}$$

The collective diffusion matrix $\mathbf{D}_{\mathrm{C}}$ couples a non-uniform ϕ_j to a particle current of type i and should be positive definite. Approximations for its components are proposed in the following subsection.

From here on, we denote the smaller species with the subscript S and the larger with L. We again look at the density profiles in steady state ($J_S = 0$ and $J_L = 0$) and consider the two limiting cases close to either the channel walls or the centerline. To compare $\dot{\gamma}\mathbf{A}$ and $\mathbf{D}_{\mathrm{C}}$ to each other, we introduce an appropriate norm $|\ldots|$.

Close to the wall: $\dot{\gamma}|\mathbf{A}| \gg |\mathbf{D}_{\mathrm{C}}|$

Close to the wall the diffusional current is neglected, meaning $v_D^{(i)} = A_{ij}[K_c \nabla(\phi_j \dot{\gamma}) + K_\eta \phi_j \dot{\gamma} \nabla \eta / \eta] = 0$. Since $\mathbf{A}$ is an invertible matrix for $a_S \neq a_L$, the trivial solution is

$$\mathbf{0} = \begin{pmatrix} K_c \nabla(\phi_S \dot{\gamma}) + K_\eta \phi_S \dot{\gamma} \frac{\nabla \eta}{\eta} \\ K_c \nabla(\phi_L \dot{\gamma}) + K_\eta \phi_L \dot{\gamma} \frac{\nabla \eta}{\eta} \end{pmatrix}. \tag{5.15}$$

Integration then yields the same solutions for ϕ_S and ϕ_L as in Eq. (5.6). This means that in the vicinity of the wall $\phi_S \propto \phi_L$ and equally $\nabla \phi_S \propto \nabla \phi_L$,. The densities for both species increase towards low-shear regions as in the monodisperse case.

Close to the channel center: $\dot{\gamma}|\mathbf{A}| \ll |\mathbf{D}_{\mathrm{C}}|$

Close to the channel center, thermal collective diffusion dominates and we we obtain the following system of equations

$$\begin{pmatrix} D_{\mathrm{C}}^{SS} & D_{\mathrm{C}}^{SL} \\ D_{\mathrm{C}}^{LS} & D_{\mathrm{C}}^{LL} \end{pmatrix} \begin{pmatrix} \nabla \phi_S \\ \nabla \phi_L \end{pmatrix} = -K_c \nabla \dot{\gamma} \begin{pmatrix} A_{SS}\phi_S^2 + A_{SL}\phi_S\phi_L \\ A_{LL}\phi_L^2 + A_{LS}\phi_S\phi_L \end{pmatrix}, \tag{5.16}$$

which, by multiplying from the left with the inverse collective diffusion tensor $\mathbf{D}_{\mathrm{C}}^{-1}$, becomes:

$$\begin{pmatrix} \nabla \phi_S \\ \nabla \phi_L \end{pmatrix} = \frac{-K_c \nabla \dot{\gamma}}{\det \mathbf{D}_{\mathrm{C}}} \begin{pmatrix} D_{\mathrm{C}}^{LL} & -D_{\mathrm{C}}^{SL} \\ -D_{\mathrm{C}}^{LS} & D_{\mathrm{C}}^{SS} \end{pmatrix} \begin{pmatrix} A_{SS}\phi_S^2 + A_{SL}\phi_S\phi_L \\ A_{LL}\phi_L^2 + A_{LS}\phi_L\phi_L \end{pmatrix} \tag{5.17}$$

We now see that a new class of solutions is possible. At equal concentrations but for different radii the coefficients of the matrix $\mathbf{A}$ behave as $A_{LL} > A_{SS}$, $A_{SL} \approx A_{LS}$, whereas the elements of the diffusion tensor obey $D_{\mathrm{C}}^{LL} < D_{\mathrm{C}}^{SL}$ and $D_{\mathrm{C}}^{SS} > D_{\mathrm{C}}^{LS}$ as seen from the model developed in the following subsection. This ultimately means that $\nabla \phi_L \propto -\nabla \dot{\gamma}$ and at the same time $\nabla \phi_S \propto -\nabla \phi_L$. Both species therefore demix in the channel center, with the larger species enriching the center and the smaller species pushed away from it. Interestingly, our observation is in accordance with experiments conducted by Semwogerere and Weeks [58].

5.2.3 Model for collective diffusion

Diffusion in a dense binary suspension of differently sized hard spheres is highly complex given hydrodynamic interactions between the particles and the relevance of excluded volume. Approximate models to accurately capture collective diffusion are scarce and often only hold in the limit of $a_S/a_L \ll 1$ or in strong dilution [161, 162]. We present here a simplified approach to calculate the diffusion coefficients in the high-density limit.

The collective diffusion coefficient D_C describes the diffusive relaxation of spatial inhomogeneities in a colloidal suspension at long wavelengths with $ak \ll 1$. For a monodisperse suspension the collective diffusivity obeys

$$D_\mathrm{C} = S^{-1} D_\mathrm{c.o.m.} = S^{-1} \lim_{t\to\infty} \frac{1}{2dt} \langle \mathbf{R}(t)^2 \rangle, \tag{5.18}$$

where the static structure factor $S = ck_\mathrm{B}T\kappa_T$ is proportional to the isothermal compressibility κ_T and the particle density c of the suspension [163, 164]. The static structure factor for a binary suspension in 2D was approximated by Boublík [165] and reads

$$S(\phi) = \frac{(1-\phi^2)}{1-\phi(1-\gamma)}, \tag{5.19}$$

with

$$\gamma = \frac{(c_S a_S + c_L a_L)^2}{c_S a_S^2 + c_L a_L^2} \tag{5.20}$$

and $\phi = \phi_i + \phi_j$. The approximative equation for a 3 dimensional mixture was proposed by [166] and reads

$$S(\phi) = \frac{(1-\phi^4)}{(1+2\phi)^2 - \Delta}, \tag{5.21}$$

with

$$\begin{aligned} \Delta = {} & \frac{3x(1-x)\phi(1-\alpha)^2}{x+(1-x)\alpha^3} \times \\ & \left((2+\phi)(1+\alpha) + \frac{3\phi\alpha}{x+(1-x)\alpha^3}((1-x)\alpha^2 + x) \right), \end{aligned} \tag{5.22}$$

where $\alpha = a_S/a_L$, $\phi = \phi_S + \phi_L$ and $x = c_S/(c_S + c_L)$. The remaining coefficient $D_\mathrm{c.o.m.}$ in Eq. (5.18) describes the center-of-mass diffusion of N particles in d dimensions and $\mathbf{R}(t) = \sum_{i=1}^{N} [\mathbf{r}_i(t) - \mathbf{r}_i(0)]/N$ is the center-of-mass displacement. $D_\mathrm{c.o.m.}$ contains all the dynamic information of the colloidal suspension and becomes the single-particle diffusivity D_0 in the dilute limit.

If hydrodynamics is included, $D_\mathrm{c.o.m.}$ decays fast in the dilute limit and slowly in the dense limit, when increasing the density [160]. Therefore, in dense suspensions S^{-1} becomes the leading factor in Eq. (5.18). It strongly depends on density, tending to infinity as the suspension approaches close packing density ϕ_rcp [160], while changes in $D_\mathrm{c.o.m.}$ are less pronounced. For our dense systems, we therefore assume a functional behavior of the form

$$D_\mathrm{C}(\phi) \approx \widetilde{D}_0 S^{-1}(\phi), \tag{5.23}$$

in which $\widetilde{D}_0 = K_d D_0$ is constant in ϕ and $0 < K_d < 1$ is a fitting parameter. The behavior of Eq. (5.23) is plotted in Fig. 5.3 for the case of two dimensions.

Then, species i diffuses along its own density gradient $\nabla\phi_i$ with the diffusivity

$$D_\mathrm{C}^{ii}(\phi) = \widetilde{D}_0^i S^{-1}(\phi), \tag{5.24}$$

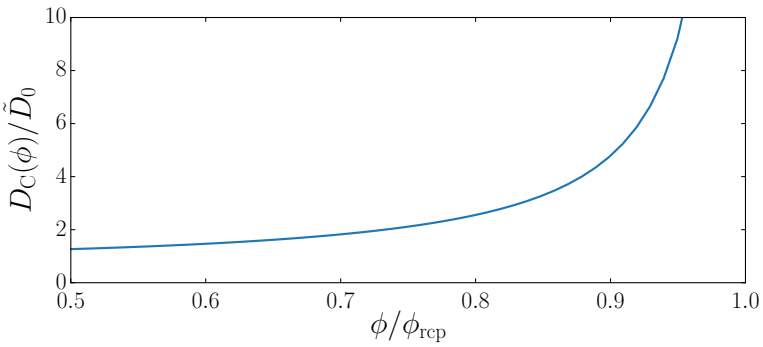

Figure 5.3: Collective diffusivity D_C of a binary suspension at equal concentration $c_L = c_S$ and size ratio $a_L/a_S = 2$ as a function of packing fraction ϕ according to Eq. (5.23) in two dimensions.

where again we use $\widetilde{D}_0^i = K_d D_0^i$. The single-particle diffusivities D_0^i obey the Stokes-Einstein relation so that $D_0^i/D_0^j = a_j/a_i$.

The non-diagonal elements of $\mathbf{D}_C$ are obtained by a simple volume-exclusion approach [162]. We formulate an effective volume fraction ϕ_i^* of colloidal species i, which accounts for the fact that the volume occupied by species j reduces the total volume available to species i,

$$\phi_i^* = \frac{\phi_i}{1-\phi_j}. \tag{5.25}$$

We assume that species i, in the presence of species j, diffuses along its own effective gradient, so that the concentration current can be written as

$$J_i = D_C^{ii} \nabla \phi_i^*. \tag{5.26}$$

In the absence of a gradient, $\nabla\phi_i = 0$, the diffusive current J_i is solely caused by density inhomogeneities of species j. Substituting Eq. (5.25) into Eq. (5.26), yields

$$J_i = D_C^{ii} \frac{\phi_i}{(1-\phi_j)^2} \nabla \phi_j \tag{5.27}$$

and we can now identify the non-diagonal diffusion coefficient as

$$D_C^{ij} = D_C^{ii} \frac{\phi_i}{(1-\phi_j)^2}. \tag{5.28}$$

5.2.4 Modeling the simulated density profiles

We use the phenomenological theory to replicate the density profiles determined in our MPCD simulations, which we will present in Secs. 5.3 and 5.4. To complete the theory, we use an empirical relation for the shear viscosity in colloidal suspensions, which was suggested in Ref. [167] following the formulation of Krieger and Dougherty [168]. It describes the divergence of the viscosity as maximum colloidal packing is approached:

$$\eta(y) = \eta_0 \left(1 - \frac{\phi(y)}{\phi_M}\right)^{-2}. \tag{5.29}$$

Here ϕ_M is the maximum area or volume coverage of random close packing. For monodisperse systems, it is calculated to be 0.82 in two dimensions [169], as compared to 0.64 in three dimensions [170]. We used the same values for our binary mixtures, which was

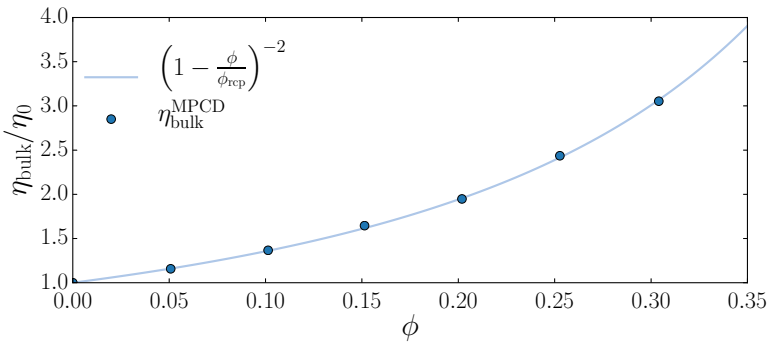

Figure 5.4: Measured viscosity with aid of Eq. (4.49) in a 3D MPCD simulation containing a suspension of volume fraction ϕ. Particle sizes are $a = 2b$, time step $\Delta t = 0.01 t_0$ and density $\rho = 10m/b^3$.

adequate within the accuracy of our simulations. In Fig. 5.4 the formula Eq. (5.29) compares well to the viscosities measured in the MPCD channel (see Sect. 4.4.1) with respect to the volume fraction ϕ of the suspended particles.

Together with the relations for the diffusivities and the viscosity, we now have a closed system of (differential) equations, which we can solve numerically using a finite difference scheme. With the particle currents from Eq. (5.14) we formulate the continuity equation for colloidal species i,

$$\frac{\partial \phi_i}{\partial t} = -\frac{\partial J_i}{\partial y}\,. \tag{5.30}$$

We integrated it using a 4^{th} order Runge-Kutta scheme until steady state of the density profiles was reached. For the form of the steady state profiles only the ratios K_η/K_c and K_d/K_c are relevant. The value for $K_\eta/K_c = 1.51$ was adopted from the fits to experiments conducted in a Couette flow by Phillips et al. [22]. Although based on three-dimensional experiments, comparison with our data from the two-dimensional simulations indicated that the same ratio K_η/K_c can be used for the disks as well as for the spheres.

The factor K_d in the diffusivities was the only fitting parameter we chose freely to replicate the density profiles determined in our MPCD simulations. We calculated the single particle diffusivities by employing the Stokes-Einstein relation $D_0^i = k_{\mathrm{B}}T/6\pi\eta a_i$, where we used the measured shear viscosity of the pure MPCD fluid in table 5.1. For all simulations in the 3D channel we set $K_d/K_c = 0.61$. For all simulations in the 2D channel we set $K_d/K_c = 7.46$. Consequently, the ratio K_c/K_d comparing the relevance of shear migration to diffusion is larger in three dimensions. This is very likely, considering the difference in collision partners of a single particle in two and three dimensions. In the latter case, the additional dimension allows for more collision partners and hence for stronger shear migration.

5.3 Results in two-dimensional Channels

We start by investigating the pressure-driven flow of a bidisperse colloidal suspension in a two-dimensional microchannel. Since simulations are not as computationally expensive as their three-dimensional counterparts, we can indulge in a more thorough parameter analysis. The capital letter subscripts S and L again account for quantities of the smaller and larger particles, respectively. The respective particle sizes are $a_L/w = 0.1$ and $a_S/w = 0.05$, in all cases.

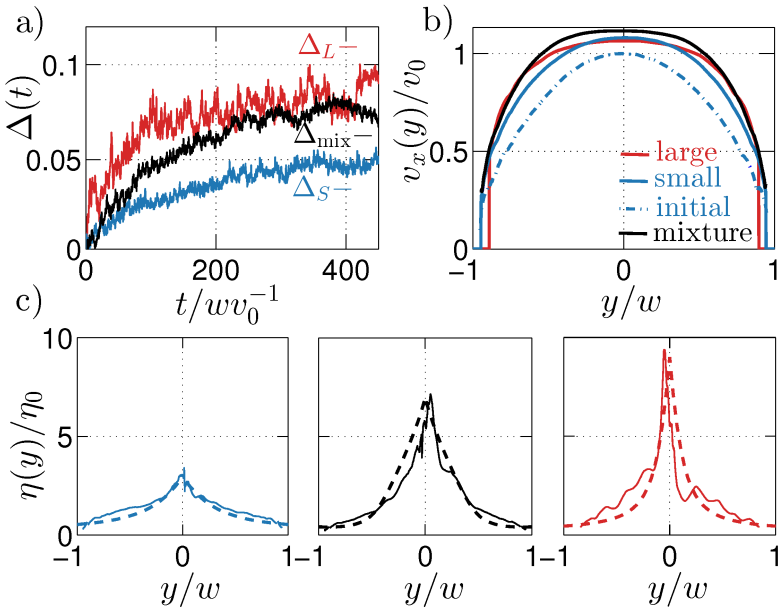

Figure 5.5: (a): Evolution parameter Δ plotted over time t for monodisperse suspensions of large (Δ_L, red) and small (Δ_S, blue) colloids as well as a mixture (Δ_{mix}, black) with $\overline{\phi}_L/\overline{\phi}_S = 1$. The overall area fraction is $\overline{\phi} = 0.5$. The same color code also applies to (b) and (c). (b): Steady-state velocity profiles $v_x(y)$ of the colloids compared to the parabolic flow profile of the initially uniform suspension of the small species (dot-dashed line). (c): Steady-state profiles of shear viscosity η, obtained from data in (b) by use of Eq. (5.33) (solid line), and from the analytical model using Eq. (5.29) (dashed).

First, we monitor the temporal evolution of the colloidal density towards steady state, then we illustrate the steady-state flow and viscosity profiles, and finally extensively discuss the particle number densities c_i for either species across the channel, which we normalize so that $\int c_i \mathrm{d}y = 2w$.

5.3.1 Evolution of density profiles

We quantify the developing inhomogeneities in the density by an evolution parameter

$$\Delta(t) = \frac{\int_{-w}^{w} \mathrm{d}y \, [c(y,t) - c(y,0)]^2}{\int_{-w}^{w} \mathrm{d}y \, [c(y,0)]^2} \, . \tag{5.31}$$

Here c is the total density either of a monodisperse or a bidisperse suspension. When $\Delta(t)$ fluctuates about a constant value, steady state is reached. For each simulation run, it is simply determined by visual inspection of $\Delta(t)$.

Figure 5.5(a) plots the temporal evolution of $\Delta(t)$ for monodisperse suspensions of small (Δ_S, blue) and large (Δ_L, red) colloids, as well as their mixture (Δ_{mix}, black) at a composition $\overline{\phi}_L/\overline{\phi}_S = 1$. Here, $\overline{\phi}_i$ means mean area fraction and the overall area fraction for both species together is $\overline{\phi} = \overline{\phi}_S + \overline{\phi}_L = 0.5$. The dynamics of shear migration clearly is slow given the long axial distances d the colloids in the center travel before $\Delta(t)$ saturates and the steady state profiles emerge: for suspensions of large particles we find that the steady state has fairly developed at $d_L \approx 100w$, whereas small particles need longer distances with $d_S \approx 400w$. The lateral particle currents in the channel scale with $J \propto a^2$, so that the larger species will tend to establish steady-state profiles faster than the smaller species in quantitative agreement with our simulations since

$a_L/a_S = 2$. However, the Péclet number defined in Eq. (5.1) scales roughly as $\mathrm{Pe} \propto a^3$ in two dimensions, given the weak dependence of D_0^i on a_i due to the Stokes paradox [171] (Sect. 3.1.5). Consequently, the stronger lateral drift of large colloids results in more inhomogeneous profiles compared to the smaller species as $\Delta_L > \Delta_S$ shows, in particular for $t \to \infty$.

The corresponding steady-state density profiles for monodisperse (top, middle) and bidisperse (bottom) suspensions are shown in the right column of Fig. 5.6. In all cases the total density in the channel center is enriched. In case of a mixture at equal composition, the colloidal species partially demix favoring the larger species in the center. We will discuss them in more detail below.

5.3.2 Steady-state flow and viscosity profiles

In Fig. 5.5 (b) we show the axial velocity profiles of the colloids. As the colloids deplete from the wall and migrate towards the center, the initially parabolic flow profiles deform and flatten in the channel center as illustrated in Fig. 5.5 (b). For comparison, we plot the profile of the initially uniform suspension of small particles. The steady-state velocity is always higher than the one of the initially uniform suspensions, which we explain below.

The solid lines in Figure 5.5 (c) illustrate profiles of the shear viscosity η determined from our MPCD-simulation data for the colloid velocities $v_x(y)$ in steady state. We use the Stokes equation,

$$\frac{\partial}{\partial y}\eta\dot{\gamma} = -f\,, \tag{5.32}$$

where f is the applied constant pressure gradient and shear rate $\dot{\gamma} = \partial v_x/\partial y$. Straightforward integration yields an expression for the shear viscosity,

$$\eta(y) = -\frac{fy}{\dot{\gamma}(y)}\,, \tag{5.33}$$

plotted as solid line in Fig. 5.5 (c).

The dashed lines are predictions based on Eq. (5.29) using the steady-state density profiles of the analytical model, which we show as dashed lines in the right column of Fig. 5.6. The symbol η_0 denotes the shear viscosity of a uniform colloidal suspension at $\overline{\phi} = 0.5$ calculated according to the empirical formula of Eq. (5.29). The predictions of the analytical model compare nicely with the results from our simulations, especially for the maximum value and width of the peak. In all cases, the viscosity η/η_0 drops below 1 in the vicinity of the wall and reaches a maximum in the center, the value of which depends on the local area fraction. This behavior explains the formation of the plug flow since the sharp increase of viscosity slows down the colloids the closer they are at the center. Due to the region with $\eta/\eta_0 < 1$, the colloidal plug glides more easily along the wall, which gives the steep increase of the flow profile at the wall and the overall larger velocities compared to a uniform suspension.

Furthermore, the peak in the viscosity profiles in Fig. 5.5 (c) is much more pronounced for the large compared to the small colloids. We note that already individual large colloids are more strongly slowed down compared to small colloids at the same location in a Poiseuille flow since they pose more resistance to the fluid flow. This is also stated in Faxén's law [3]. In addition, also the particle density of larger colloids is higher in the center (see Fig. 5.6, right column). Altogether, this qualitatively explains the pronounced difference in the viscosity profiles.

Interestingly, the differences in the flow profiles of Fig. 5.5 (b) are more subtle. For larger colloids the plug flow is more developed compared to small colloids due to

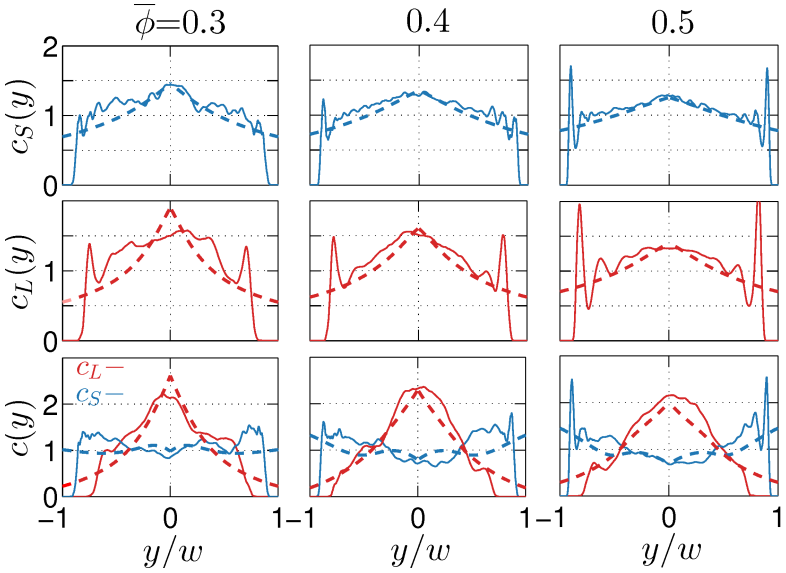

Figure 5.6: Steady-state density profiles c_i of monodisperse (top and middle) and bidisperse (bottom row) suspensions at $\overline{\phi}_L/\overline{\phi}_S = 1$. Total area fraction $\overline{\phi}$ increases from left to right. Particle sizes are $a_L/w = 0.1$ and $a_S/w = 0.05$. The solid lines correspond to MPCD simulations, the dashed lines are determined from the phenomenological theory. The Péclet number for the small particles is $\mathrm{Pe}_S \approx 1$.

the larger viscosity peak. In case of a mixture, higher center velocities compared to monodisperse systems occur. The large colloids strongly enrich the center (see Fig. 5.6, right column, bottom), whereas the small colloids are more pushed towards the wall. Still, the absolute density of the latter is smaller than for a pure monodisperse dispersion of the same total volume fraction. So, in the mixture the viscosity at the wall is also smaller and the colloidal plug as a whole can slide more easily along the wall resulting in the increased center velocity.

5.3.3 Steady-state density profiles

We now discuss the profiles of the particle densities for the large and small colloids either in the monodisperse or in the bidisperse suspension. Each density plot shows the results of the MPCD simulations (solid line) and the phenomenological theory (dashed line), where the densities are normalized such that $\int c_i \mathrm{d}y = 2w$. In the MPCD simulations thermal motion and interparticle interactions give rise to stochastic fluctuations in the density profiles. In order to minimize these density fluctuations around the steady-state profiles, time averages were taken.

From left to right in Fig. 5.6, we vary the mean area fraction $\overline{\phi} = \overline{\phi}_S + \overline{\phi}_L$ from 0.3 to 0.5. For the monodisperse suspensions in the top and middle row, we find a clear enrichment in the channel center for both species. The enrichment decreases with increasing mean area fraction since already in the center one approaches random close packing and additional particles at increasing $\overline{\phi}$ more and more fill up the space between the walls and centerline. Thereby, the peak in the density profile decreases. However, the absolute value of the area fraction in the center, given by $\phi \propto \overline{\phi}c$, still increases towards random close packing. The overall tendency of the profiles is well predicted by our phenomenological theory, although, especially for the large species we notice a more convex shape of the density profiles in the center, which is not captured by our model. Presumably, for the small species the continuum approximation is better valid and our

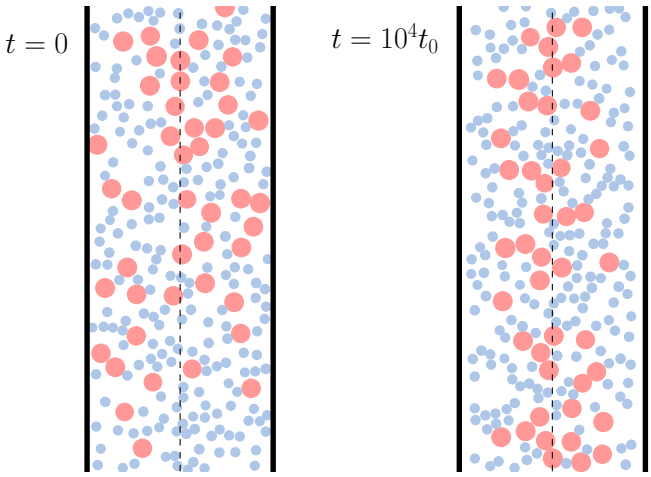

Figure 5.7: View of the 2D channel with a binary suspension of $\overline{\phi} = 0.3$, $\overline{\phi}_L/\overline{\phi}_S = 1$ and $a_L/a_S = 2$ at different times. Left: immediately after start of the simulation at $t = 0$. Right: after steady-state has been reached at $t = 10^4 t_0$.

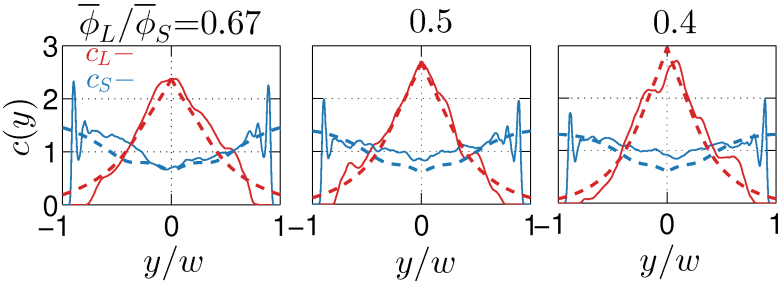

Figure 5.8: Steady-state density profiles c_i of bidisperse suspensions with varying ratio of mean area fractions $\overline{\phi}_L/\overline{\phi}_S$. Other parameters are $\overline{\phi} = 0.5$, $a_L/w = 0.1$, $a_S/w = 0.05$, and $\mathrm{Pe}_S \approx 1$ for the smaller species. The solid lines correspond to MPCD simulations and the dashed lines are determined from the phenomenological theory.

phenomenological model fits better.

The MPCD simulations clearly reveal packing effects close to the confining walls of the channel. The disks form a layered structure indicated by the peaks in the density. Accordingly, the first peak is at a distance a_i from the wall and further peaks appear as the mean area fraction is increased. Generally, the oscillations are stronger for the large species, because scaled by the disk size, they are confined in a more narrow channel.

The mixture with equal mean area fractions for both particles species, $\overline{\phi}_S = \overline{\phi}_L$, exhibits segregation of the smaller colloids away and of the larger colloids towards the channel center in agreement with the solution discussed for Eq. (5.17), where collective diffusion drives the small particles outwards (see also Fig. 5.7). However, in contrast to our discussion of the profiles at the wall following Eq. (5.15), the density c_S decreases away from the wall. If we compare shear driven migration and diffusion close to the channel walls, we find $K_c a_S^2 \dot{\gamma} \phi_S / K_d D_0^S \approx 3$. This implies that the approximation of neglecting thermal diffusion at the walls is not possible for small colloids. In contrast, the density profiles in three dimensions presented in Sec. 5.4.2 but also the experimental profiles of Ref. [58] are in agreement with this approximation. Finally, we also find that in steady state the large particles are barely found in close contact with the channel walls.

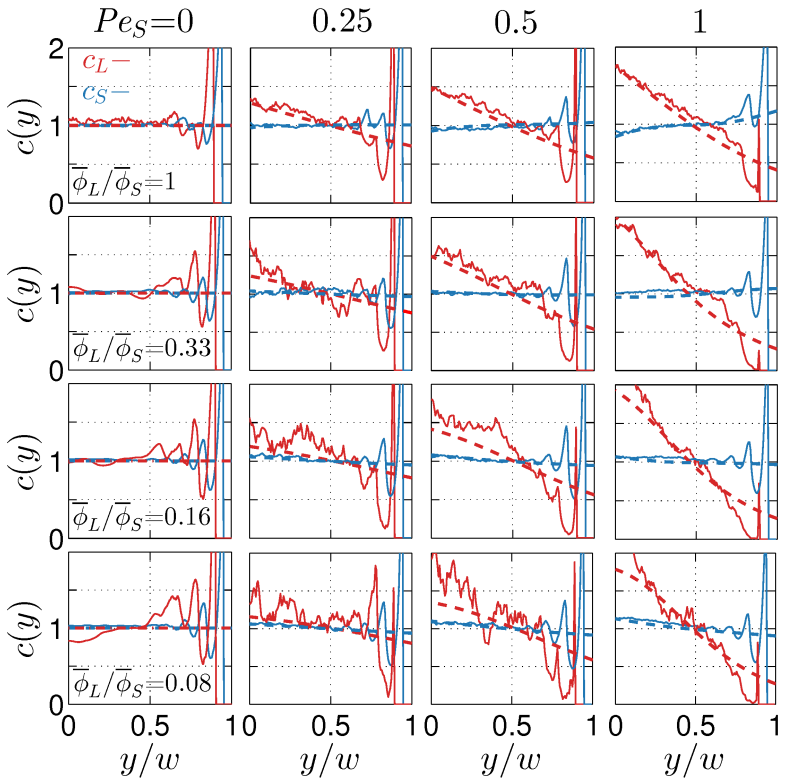

Figure 5.9: Steady-state density profiles c_i of bidisperse suspensions for decreasing ratio of mean area fractions $\overline{\phi}_L/\overline{\phi}_S$ from the top to bottom and increasing Péclet number Pe_S of the small species from left to right. Other parameters are $\overline{\phi} = 0.5$, $a_L/w = 0.1$ and $a_S/w = 0.05$. The solid lines correspond to MPCD simulations and the dashed lines are determined from the phenomenological theory.

Next, we vary the ratio of mean area fractions, $\overline{\phi}_L/\overline{\phi}_S$, keeping the total area fraction constant at $\overline{\phi} = 0.5$. The profiles are plotted in Fig. 5.8 with the area fraction of the large species compared to the one of the smaller species decreasing from left to right from 0.67 to 0.4. In all cases, the large species prevails its dominance in the channel center, although greatly outnumbered by the smaller species. The central peak in c_L becomes more pronounced with decreasing $\overline{\phi}_L/\overline{\phi}_S$, since the few large colloids can all accumulate close to the center. In contrast, the small colloids are less displaced to the walls with decreasing $\overline{\phi}_L/\overline{\phi}_S$ since the large colloids leave more space for them. Peak values and tendencies in the numerical data are well predicted by the phenomenological model.

In order to obtain a complete picture for the steady-state density profiles, we plot them in Fig. 5.9 for increasing Péclet number Pe_S of the smaller colloid species by adjusting the central flow speed v_0. In addition, results for even smaller ratios $\overline{\phi}_L/\overline{\phi}_S$ are shown. The profiles are illustrated in one half of the channel at mean area fraction $\overline{\phi} = 0.5$.

Again, the large species is enriched in the center for all cases with $\mathrm{Pe}\neq 0$. The concentration in the center increases with $\mathrm{Pe}\neq 0 \propto v_0 \propto \dot{\gamma}$ and for decreasing $\overline{\phi}_L/\overline{\phi}_S$. The profiles of the small particles deviate little from the uniform distribution since the Péclet number is one at most, meaning that thermal collective diffusion is always important. At the highest Péclet number the profile switches from a slight depletion in the center to an enrichment when decreasing $\overline{\phi}_L/\overline{\phi}_S$ from one to 0.08, where 48 small

colloids per one large colloid occupy the channel. At this ratio the small colloids converge towards the density profiles of the monodisperse suspension.

The simulated profiles are overall well described by the phenomenological theory. In particular, the behavior of the small colloids with decreasing $\overline{\phi}_L/\overline{\phi}_S$ is captured. For small ratios $\overline{\phi}_L/\overline{\phi}_S$ the peak of the large particles are somewhat underestimated. In case of zero applied flow or zero Péclet number the constant equilibrium densities are obtained. However, for decreasing ratio $\overline{\phi}_L/\overline{\phi}_S$, the layering of the large particles at the channel walls becomes more pronounced and a tendency to accumulate at the walls is visible. This should be due to depletion forces that large particles experience in a suspension of small particles [172]. Already at the Péclet number $\mathrm{Pe}_L \approx 2.5$ of the large particles (second column in Fig. 5.9), the trend is reversed and shear-induced migration to the center prevails.

5.4 Results in a three-dimensional Channels

We expand our system into the third dimension by studying the flow of colloidal spheres with mean volume fraction $\overline{\phi}$ between two parallel plates. Monodisperse disks in two dimensions can be packed much closer than spheres, as the random-close packing fractions mentioned in Sec. 5.2.4 show, $\phi_{\mathrm{M}}^{2D} = 0.82$ and $\phi_{\mathrm{M}}^{3D} = 0.64$, and the ratio is $\phi_{\mathrm{M}}^{3D}/\phi_{\mathrm{M}}^{2D} = 0.78$. To be able to compare to the two-dimensional simulations conducted at $\overline{\phi} = 0.5$, most of the simulations in three dimensions were conducted at $\overline{\phi} = 0.35$.

If not stated otherwise, particle sizes again are $a_S = 0.05w$ and $a_L = 0.1w$. As before, we start by analyzing the temporal evolution of the particle density towards steady state, where we then monitor flow and viscosity profiles. Finally, for various sets of parameters we present density profiles normalized as before so that $\int c_i \mathrm{d}y = 2w$. Throughout this section we discuss differences to the two-dimensional simulations.

5.4.1 Evolution of density profiles

We evaluate the temporal evolution of the density profiles with the same order parameter $\Delta(t)$ as in Sec. 5.3.1. Figure 5.10(a) plots $\Delta(t)$ versus time for monodisperse suspensions of small (Δ_S, blue) and large (Δ_L, red) colloids, as well as their mixture (Δ_{mix}, black) at equal volume fractions $\overline{\phi}_L/\overline{\phi}_S = 1$. We notice that the required time for the evolution to the steady state profiles is comparable to the one for the disks. The large particles rapidly establish steady state after traveling roughly a distance $d_L \approx 100w$, whereas for the small particles Δ_S converges only slowly towards its asymptotic value and reaches it after a distance of roughly $d_S \approx 500w$.

The asymptotic values of Δ for $t \to \infty$ certainly depend on the fact that colloids pack differently in two and three dimensions. However, we notice that the difference in density inhomogeneities between small and large spheres is more pronounced in three compared to two dimensions. Presumably because single particle diffusion in two dimensions scales only weakly in particle size a_i, as a consequence of the Stokes paradox [171], whereas in three dimensions it scales like $1/a_i$ and therefore is weaker for larger particles. Consequently, Péclet numbers here are $\mathrm{Pe}_S \approx 1$ and $\mathrm{Pe}_L \approx 16$, as opposed to $\mathrm{Pe}_S \approx 1$ and $\mathrm{Pe}_L \approx 10$ in two dimensions.

In case of the mixture the properties of the two species contribute so that we find $\Delta_S < \Delta_{\mathrm{mix}} < \Delta_L$. The entrance length d of the binary suspension roughly measures $d \approx 400$.

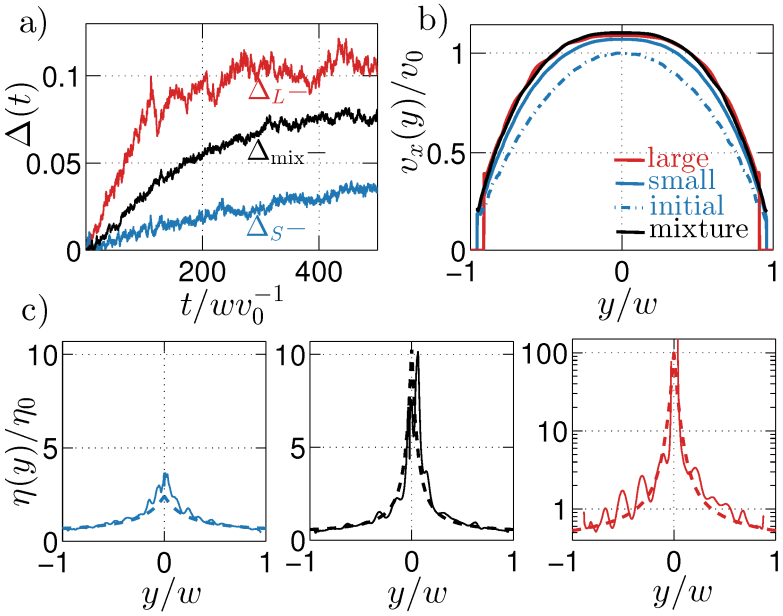

Figure 5.10: (a): Evolution parameter Δ plotted over time t for monodisperse suspensions of large (Δ_L, red) and small (Δ_S, blue) colloids as well as a mixture ($\Delta_{\rm mix}$, black) with $\overline{\phi}_L/\overline{\phi}_S = 1$. The overall volume fraction is $\overline{\phi} = 0.35$. The same color code also applies to (b) and (c). (b): Steady-state velocity profiles $v_x(y)$ of the colloids compared to the parabolic flow profile of the initially uniform suspension of the small species (dot-dashed line). (c): Steady-state profiles of shear viscosity η, obtained from data in (b) by use of Eq. (5.33) (solid line), and from the analytical model using Eq. (5.29) (dashed). Note the logarithmic scale for the red curve.

5.4.2 Steady-state flow and viscosity profiles

In Fig. 5.10(b) we plot the axial velocity profiles and compare them with the parabolic flow field of the initially uniform suspension of the small species. Qualitative agreement with the disks is obtained as the steady-state distributions of the spherical particles also induces a plug flow. The same reasons provided in Sec. 5.3.2 apply here. However, the plug flows are not as pronounced as in Fig. 5.5(b). Presumably, since the colloids in three dimensions occupy less space than the fluid when compared to two dimensions as the following ratios demonstrate: $\overline{\phi^{\rm 3D}}/(1-\overline{\phi^{\rm 3D}}) = 0.54 < \overline{\phi^{\rm 2D}}/(1-\overline{\phi^{\rm 2D}}) = 1.0$. Furthermore, the two-plate geometry might also play a role. It allows the colloids to move side wise in the shear plane so that the plug flow is less pronounced. Finally, the flow profiles of the large-particle suspension and the mixture are identical, in contrast to the results in two dimension.

The solid lines in Fig. 5.10(c) illustrate profiles of the shear viscosity η calculated from Eq. (5.33) with the simulated colloid velocities $v_x(y)$ from Fig. 5.10(b). The dashed lines again are predictions using the density profiles from our phenomenological theory in the empiric formula (5.29) for $\eta(\phi)$. The respective profiles for the monodisperse suspensions are shown in Fig. 5.12 and for the mixture in Fig. 5.14, lower left. The relation between the shape of the flow and the viscosity profiles was already discussed in Sec. 5.3.2.

Also in three dimensions, our phenomenological model provides predictions that quantitatively agree with the simulated data. This supports our assumption that the shear viscosity of the mixture can also be approximated by the empiric formula for $\eta(\phi)$

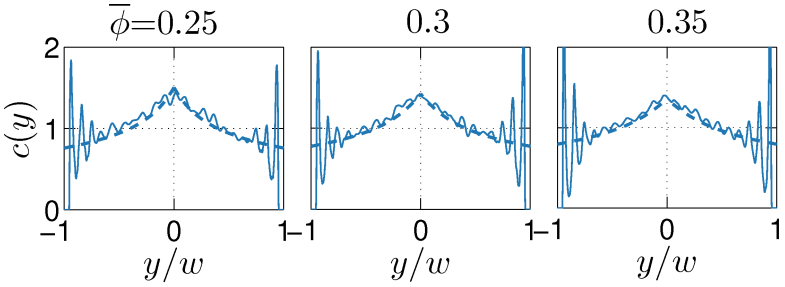

Figure 5.11: Steady-state density profiles c of monodisperse suspensions with particle size $a/w = 0.05$. Total volume fraction $\overline{\phi}$ increases from left to right. The solid lines correspond to MPCD simulations, the dashed lines are determined from the phenomenological theory. The Péclet number is Pe ≈ 1.

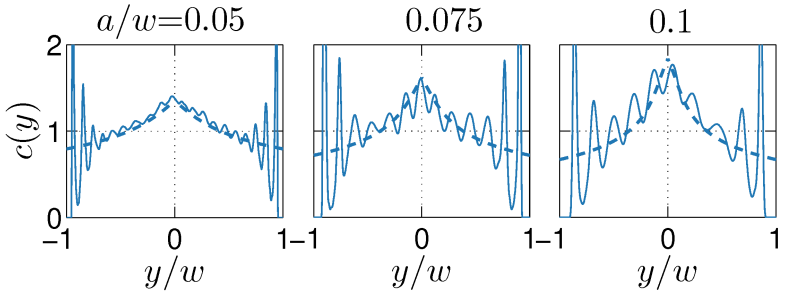

Figure 5.12: Steady-state density profiles c of monodisperse suspensions with volume fraction $\overline{\phi} = 0.35$. Particle size a/w increases from left to right. The solid lines correspond to MPCD simulations, the dashed lines are determined from the phenomenological theory. The Péclet number from left to right is Pe ≈ 1, 5, and 16.

using $\phi = \phi_S + \phi_L$. As discussed before, quantitative differences between the two colloidal species are more distinct than in two dimensions. Whereas small spheres as well as the mixture show similar behavior as the disks, the large colloids approach random close packing in the center, which results in the strong increase of $\eta(y)$ to ca. $100\eta_0$, where η_0 is the reference viscosity of the uniform suspension at the same mean volume fraction $\overline{\phi} = 0.35$. The oscillations in the solid line are caused by slight undulations in the flow profile of Fig. 5.10(c) and ultimately by the strong oscillations in the corresponding density profile of Fig. 5.12, left, which are due to layer formation.

5.4.3 Steady-state density profiles

We now present the density profiles determined either from the MPCD simulations (solid line) or the phenomenological theory (dashed line).

In Fig. 5.11, we increase the mean volume fraction from $\overline{\phi} = 0.25$ to 0.35 for the suspension of the small colloids. As in two dimensions, we find a clear enrichment of particles in the channel center. With increasing mean volume fraction $\overline{\phi}$, the density peak relative to the uniform particle distribution decreases since colloids cannot pack more densely in the center than random close packing. Finally, apart from the layering of the colloids close to the walls, the phenomenological theory reproduces the profiles very well, also in the following Fig. 5.12.

We vary the particle size a of the monodisperse suspension in Fig. 5.12 at total

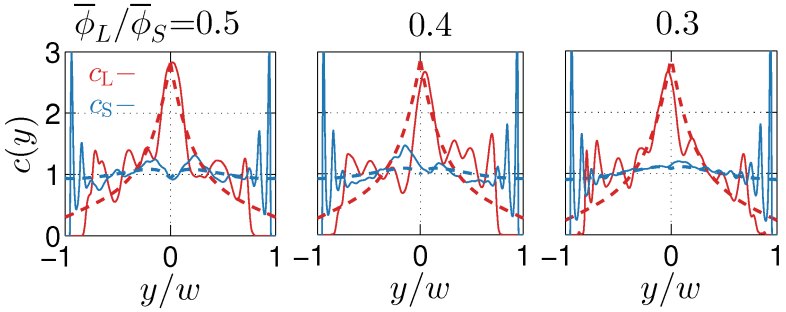

Figure 5.13: Steady-state density profiles c_i of bidisperse suspensions with varying ratio of mean volume fractions $\overline{\phi}_L/\overline{\phi}_S$. Other parameters are $\overline{\phi} = 0.35$, $a_L/w = 0.1$, $a_S/w = 0.05$, and $\mathrm{Pe}_S \approx 1$ for the smaller species. The solid lines correspond to MPCD simulations and the dashed lines are determined from the phenomenological theory.

volume fraction $\overline{\phi} = 0.35$. Shear migration more strongly enriches the larger colloids in the channel center since shear-induced drift dominates over diffusion as documented by the strong size dependence of the Péclet number, $\mathrm{Pe} \propto a^4$. Note that the number of oscillation peaks in all three cases is the truncated integer value of w/a; that is from left to right in Fig. 5.12, we observe 20, 13, and 10 peaks in the density profiles. In equilibrium at zero flow ($v_0 = 0$), the oscillations in the channel center vanish for all three particle sizes. Obviously, flow induces layering in the center, which is particularly pronounced for the large particle species. Interestingly, in two dimensions we do not observe pronounced layering close to the channel center. So, we expect sheared disks to jam more easily than sheared spheres, which use the additional dimension to order in layers parallel to the shear plane and thereby reduce viscous shear stress. This also explains the more pronounced plug shape of the flow profiles in two dimensions [see Fig. 5.5(b)] compared to the three-dimensional counterparts in Fig. 5.10(b).

In Fig. 5.13 we show density profiles for mixtures consisting of both particle species with respective radii $a_S/w = 0.05$ and $a_L/w = 0.1$ at different volume compositions. The corresponding profiles of the two-dimensional channel are plotted in Fig. 5.8. The large particles tend to form layers towards the wall. However, the profiles exhibit stochastic irregularities due to the relatively small number of large particles used in the simulations to determine $c_L(y)$. For example, at equal composition $\overline{\phi}_L/\overline{\phi}_S = 1$, one large sphere occupies the same space as 8 small spheres. The statistics worsens further with decreasing $\overline{\phi}_L/\overline{\phi}_S$. However, the overall shape of the profiles emerge.

The profiles of the large particles do not vary so much with $\overline{\phi}_L/\overline{\phi}_S$ in contrast to the two-dimensional case. The large particles show a pronounced enrichment in the center and are depleted from the wall. However, the region where they clearly demix from the small particles is more narrow. The small colloids also behave differently compared to two dimensions. The ratio of shear-induced migration to diffusion becomes $K_c a_S^2 \dot{\gamma} \phi_S / K_d D_0^S \approx 12$ and is by a factor of four larger compared to the ratio found for colloidal disks. The approximation of neglecting diffusion close to the walls is therefore justified and the density increases when going away from the wall, as predicted from Eq. (5.15). Furthermore, for $\overline{\phi}_L/\overline{\phi}_S \gtrsim 0.4$ the density profiles of the small colloids show a dip, although not very pronounced. However, this unimposing characteristic is also visible in the experiments in Ref.[58] and, furthermore, predicted by our phenomenological model as discussed after Eq. (5.17). Ultimately, the dip vanishes at $\overline{\phi}_L/\overline{\phi}_S \lesssim 0.3$. In total, our phenomenological theory very well describes all these features.

Finally, in Fig. 5.14 we compare two mixtures with size ratio $a_L/a_S = 1.5$ (top) and

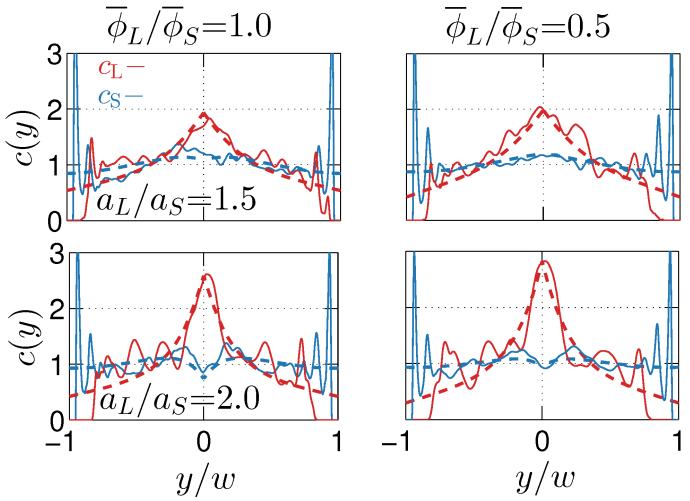

Figure 5.14: Steady-state density profiles c_i of two mixtures with different ratios of particle size ratio: $a_L/a_S = 1.5$ (top row) and $a_L/a_S = 2.0$ (bottom row) at two composition values $\overline{\phi}_L/\overline{\phi}_S$. Mean volume fraction is $\overline{\phi} = 0.35$ and $\mathrm{Pe}_S \approx 1$ for the small species with radius $a_S/w = 0.05$. The solid lines correspond to MPCD simulations and the dashed lines are determined from the phenomenological theory.

$a_L/a_S = 2$ (bottom) at compositions $\overline{\phi}_L/\overline{\phi}_S = 1$ (left) and $\overline{\phi}_L/\overline{\phi}_S = 0.5$ (right). Clearly, demixing is less pronounced for the smaller size ratio. At equal composition we also find a smaller peak in the profile of the larger particles. The phenomenological theory also catches the observed size dependence and thereby confirms the major structure of the coupling matrix $\mathbf{A}$ with its geometrical factors.

5.5 Summary and Conclusion

We compared a phenomenological model for shear-induced migration in colloidal dispersions to simulation data for hard spheres suspended in the MPCD fluid and flowing through two- and three-dimensional microchannels. MPCD is a mesocale particle-based simulation technique for solving Navier-Stokes equations and fully incorporates thermal fluctuations. Our phenomenological theory introduces drift or migration currents due to a gradient in the particle collision frequency as well as a spatially varying viscosity and it also includes collective diffusion. Our model extends work by Phillips et al. [22] to bidisperse suspensions of Brownian particles. Provided that the approximations for the collective diffusion tensor and shear viscosity are still valid, the model can be extended to n-species systems.

Collective diffusion in our phenomenological model is necessary to generate density profiles where large particles segregate in the center of a microchannel whereas small particles are depleted. Such segregation patterns are also observed in a model based on stress and energy equipartition [88] and in dry granular flow [173], where collective diffusion is not of thermal origin. In particular, the theoretical work of Ref. [174] on dry granular matter, sliding in a vertical chute, shows similarities but also differences to our work. Generally, all particles tend to migrate to the center of the channel. At relatively low volume fractions, large particles segregate more strongly in the center and smaller particles show layering at the walls similar to Fig. 5.14 (bottom, left). At higher particle packing this segregation trend reverses.

Interestingly, we are able to reproduce viscosity and density profiles of the MPCD

simulations from our phenomenological equations using only one fit parameter for all different cases studied in two and three dimensions. We achieved a good agreement for the shape of the profiles and the range of density values.

In monodisperse suspensions particles enrich in the center of a microchannel due to shear migration. Comparing viscosity, flow, and density profiles in two and three dimensions, we noticed stronger differences between small and larger spheres as compared to small and large disks with the same size ratio. Also, in three dimensions viscous shear in the pressure driven flow induces layering of the particles throughout the channel width, which is absent in two dimensions. We argued that the additional spatial dimension enables layer formation and thereby reduces shear stress. For binary colloidal mixtures we observed that the larger particle species enriches the center. In two dimensions the smaller species is depleted from the center and the density grows steadily towards the channel walls, which can only be explained by taking into account collective diffusion even close to the wall, where shear-induced migration is strong. The effect of depletion decreases with mean composition $\overline{\phi}_L/\overline{\phi}_S$. In three dimensions the densities of both species grow from the wall towards the center. A narrow depletion dip of the smaller species occurs in the center at ratios of mean volume fractions $\overline{\phi}_L/\overline{\phi}_S \gtrsim 0.4$. This subtle detail is predicted by our phenomenological theory and observed in experiments of Ref. [58]. We attribute the qualitatively different behavior between disks and spheres to the fact that in two dimensions shear-induced migration compared to collective diffusion is less effective than in three dimensions.

In three dimensions our phenomenological model and the MPCD simulations show good agreement with the experimental observations by Semwogerere and Weeks [58] in a bidisperse suspension at composition $\overline{\phi}_L/\overline{\phi}_S \approx 1$, mean volume fraction $\overline{\phi} \approx 0.35$, and particle size ratio $a_L/a_S \approx 2$. Both densities increase away from the wall, whereas in the center the large colloids strongly concentrate and the small colloids are depleted as argued in Sec. 5.2.2. However, the authors also reported that the smaller species dominates the channel center at $\overline{\phi}_L/\overline{\phi}_S \approx 0.4$, which we do not observe neither in theory nor in our simulations. To our knowledge, there is no model, which captures this effect so far.

The behavior of dense colloidal suspensions in microfluidic flow is determined by confinement and structure formation. Further increasing the density of monodisperse suspensions flowing inside a microchannel, yields novel dynamic effects such as oscillations in flow speed and colloidal jamming [44, 45]. In the next chapter we will extend our simulations into this regime and aim on contributing to their theoretical understanding.

6 Self-Organized Velocity Pulses of Dense Colloidal Suspensions

The results presented in the following chapter are based on the manuscript [B].

In this chapter we deepen our understanding of pressure driven colloidal flow in the densely packed regime. In Sect. 2.3.2 we showed that pressure driven flow of dense colloidal suspensions through microchannels produces regular and irregular oscillations in flow speed [44, 45]. In the presented works, these effects are connected with jamming and the formation of force chains [31]. Prerequisites for the existence of force chains are frictional contacts between particles. Over the past years research has stressed the necessity for frictional contacts to explain discontinuous shear thickening [40–42], jamming [6] and shear migration [57, 65].

In the following we again utilize the MPCD method to simulation low-Reynolds-number flow. We combine it with a linear spring model including friction [59], in order to simulate jamming and effectively embed a large number of colloidal particles. The general setup is similar to that in the previous chapter with one major difference. The mean packing fraction of the colloids within the channel is near the random close packing density. The random close packing density is an empirical parameter used to quantify the maximum packing density objects can obtain when packed randomly [170]. For mono dispersed disks it is around $\phi = 0.82$ [175], but may vary within confinements [176]. An important implication of this is that while shear induced migration still exists, its effect on the lateral density distribution is minimal. The reason for this is twofold. On the one hand the collective diffusion coefficient D_c, which governs down-gradient diffusion, is strong in very dense suspensions [160] (see also Fig. 5.3). On the other hand, the colloidal flow profile is rather flat and the colloids therefore exhibit only weak shear stress and mainly between the first colloidal layers at the channel wall.

Density inhomogeneities in flow direction are still produced due to the possibility of colloidal jamming. Jams locally arrest the flow and give rise to rarefaction waves. These waves experience fast dynamics when compared to shear induced migration. While for shear migration particle fluxes scale with the shear rate $\propto v_0 a/w$, for colloidal jamming they scale with the flow velocity $\propto v_0$ along the channel. In consequence, shorter run times allow for simulations on larger scale.

With our model we are able to produce velocity pulses that travel upstream of the channel and we show that the properties are very similar to those observed in the ex-

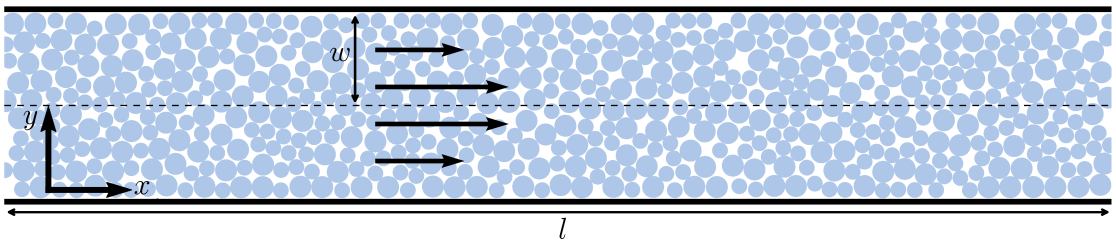

Figure 6.1: Channel geometry of width $2w$ and length l. Channel walls are at $y/w = 1$ and $y/w = -1$ and periodic boundary conditions in x-direction apply. A constant pressure gradient σ drives a binary suspension out of equilibrium. While the ratio between channel width w and particle size a is correctly displayed, the channel length l is typically much larger.

periment by Isa *et al.* [44]. With increasing colloid density, these pulses emerge first as solitary jams and later as regular pulse trains. At the highest simulated density we observe unstable solitary pulses in the colloidal flow similar to experimental observations [45]. We present a thorough parameter study on how friction and mean packing density effect the formation of these pulses. Moreover, a newly formulated nonlinear continuum model that reproduces the flow instabilities from our simulations is presented and analyzed using the tools of nonlinear dynamics (Sect. 3.4).

6.1 Setup and Parameters

We simulate pressure driven flow of a very dense colloidal suspension inside a channel of width $2w$ in two dimensions as illustrated in Fig. 6.1. The colloidal suspension is modeled as a binary mixture of disks with neutral buoyancy and with radii $a/w = 0.084$ and 0.118. Both species are generated at equal number and have a size ratio of 1.4 in order to prevent crystallization [176].

In a first attempt the colloidal interactions were resolved using event driven molecular dynamics (Sect. 4.2.2). However, in the random close packing regime this model exposed two major drawbacks. The first concerns numerical efficiency. The model leaps chronologically to the next collision and then updates the subsequent events according to the new velocities. Consequently the model is inherently serial and does not profit much from parallelization. At intermediate densities as in the previous chapter ($\overline{\phi} \approx 0.5$), this has no tremendous consequence because the runtime is dominated by the MPCD streaming and collision step. In the dense regime ($\overline{\phi} \gtrsim 0.75$), where jamming occurs, the hard spheres might find themselves in high frequency collision chains, which notably increase the runtime. Secondly and more importantly, the model only allows for a single contact between two colloids at one time independent of how large the system is. Consequently and because the colloids have a thermal velocity, kinetic arrest can not be captured by this model.

All this can be remedied by using a "soft" particle model using repulsive forces instead of instantaneously resolved translational and rotational momentum exchanges. Therefore, the frictional contacts of a colloid with the wall and other colloids are treated with the linear spring model presented in Sect. 4.2.3. The model is commonly used in granular physics [59, 151] and utilizes Coulombs law of friction Eq. (4.41), with the dimensionless friction coefficient μ. In order to mimic nearly hard particles, we choose the linear spring constant k in normal and tangential direction to be large, such that

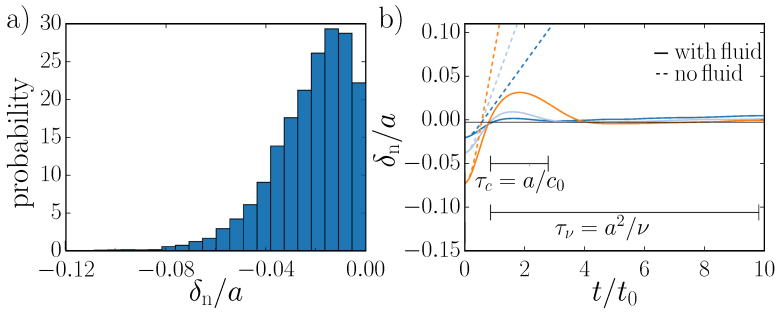

Figure 6.2: a) Time averaged probability distribution of overlaps in units of colloidal radius. Simulation parameters are like in Tab. 6.1 with $\overline{\phi} = 0.75$. b) Dynamics of two colloidal disks suspended in quiescent MPCD fluid with viscosity $\nu = 2.1b^2/t_0$ (solid line) and in vacuum (dashed line) for various initial overlaps δ_n.

$k_n = k_t = 2500k_BT/b^2$. A constant pressure gradient $\sigma = -\nabla p = 1.25k_BT/b^3$ is then applied to drive the fluid out of equilibrium. In order to show that the collisions between colloids are nearly hard and behave overdamped as required in the limit of low Reynolds numbers, we refer to Fig. 6.2. The results represent a simulation with typical parameters for this chapter. In Fig. 6.2 a) we present the time averaged distribution of overlaps in normal direction in units of colloidal radius a and with a mean packing density of $\overline{\phi} = 0.75$. The bulk of the penetrations is about $1-2\%$ deep. Less than 10% of the contacts overlap as deep as $> 0.04a$. In Fig. 6.2 b) we show the dynamics of two colloids for various initial overlap distances δ_n, with fluid and in absence of the fluid. While on short time scales both setups produce a repelling outward push, the setup with the MPCD fluid recovers damping on time scales larger than the sonic speed time scale $\tau_c = a/c_0$, with c_0 the speed of sound of the MPCD fluid defined in Eq. (3.84). The time τ_c is required for the fluid particles to react and equilibrate density changes over length scales of size a. On the viscous time scale $\tau_\nu = a^2/\nu$ the collision is completely damped.

If not otherwise specified, the MPCD parameters used throughout this chapter are summarized in Tab. 6.1.

As we have seen in the previous chapter, densely packed particles experience high hydrodynamic friction quantified by the bulk viscosity ν_{bulk} (see Fig. 5.4). In this chapter we use densities around the random close packing density, at which the bulk viscosity diverges to infinity. As a result we are able to choose a slightly larger time step $\Delta t = 0.02t_0$ for numerical speed and still maintain low channel Reynolds numbers $\text{Re}_w \lesssim 0.2$ (compare Eq. (4.46)). Simultaneously, it can be expected that single particle diffusion becomes irrelevant so that we place our simulations in the high-Péclet number regime.

In order to be able to observe several velocity pulses in the channel, we choose a channel length as long as $l/w = 480$ and implement periodic boundary conditions in flow direction, i.e. x-direction. Since the interesting variations of colloidal velocity $v(x)$ and local area fraction $\phi(x)$ occur along this direction, we average them over the channel cross section, using

$$\psi(t,x) = \frac{1}{2w}\int_{-w}^{w} \psi(t,x,y)\,\mathrm{d}y, \tag{6.1}$$

with $\psi = \{v, \phi\}$. In order to determine ϕ locally, we use a Voronoi tessellation for the colloidal packing [177].

parameter	value
m	1
b	1
$k_\mathrm{B}T$	1
Δt	$0.02t_0$
ρ	$25m/b^2$
a	$2.1b$ and $2.94b$
k_n	$2500k_\mathrm{B}T/b^2$
k_t	$2500k_\mathrm{B}T/b^2$
σ	$1.25k_\mathrm{B}T/b^3$
w	$25b$
l	$12000b$
ν	$1.98b^2/t_0$
$\overline{D}$	$0.00411b^2/t_0$

Table 6.1: Overview of the MPCD simulation parameters and transport coefficients in units of fluid-particle mass m, collision box length b, and temperature $k_\mathrm{B}T$.

The high mean packing fractions $\overline{\phi} > 0.7$ are obtained by randomly placing up to 23000 initially pointlike colloids in the channel. Iteratively, they are expanded in size and the overlaps are removed by the linear spring model in absence of the MPCD fluid until the final colloidal size is reached [178]. Finally, the MPCD fluid is filled into the free space.

6.2 Simulation Results

In the following we present the results of our simulations. Most of the simulations run on either 6 or 8 Intel i7 processor cores and a few on 18 cores from a Xeon E5 processor. All simulation runs use the parallel environment generated by OpenMP introduced in Sect. 4.5.

6.2.1 Observations

Inside a channel using the parameters from Tab. 6.1 at $\overline{\phi} = 0.75$ and with $\mu = 1$, we make the following observations. As soon as the pressure gradient is switched on, the suspension jams at different locations along the channel. Downstream of these jams, colloids can still freely move, which produces a dilute region with increased flow speed because the bulk viscosity decreases. Upstream of the jam, more colloids are accumulated, which increases the size of the jam. As the jam develops it eventually reaches a configuration, in which the rate of downstream outflow of colloids and upstream inflow of colloids equilibrate. The structure then moves with constant velocity c and constant shape upstream of the flow as indicated in Fig. 6.3. At $t = 250t_0$ a rarefaction pulse enters from the right and gradually dissolves the jam upstream. The jammed region is indicated by a dense force chain network spanning across the channel, visualized by the red lines that indicate contact between pairs of colloids. Due to the higher packing density, the flow speed is close to zero and the flow profile flat. At $t = 500t_0$ we observe roughly parabolic flow throughout the section with maximum velocity in the section center. At $t = 750t_0$ the flow jams downstream of the pulse at a sharp transition and becomes flat again. In doing so, the flow diverges at the transition and pushes the

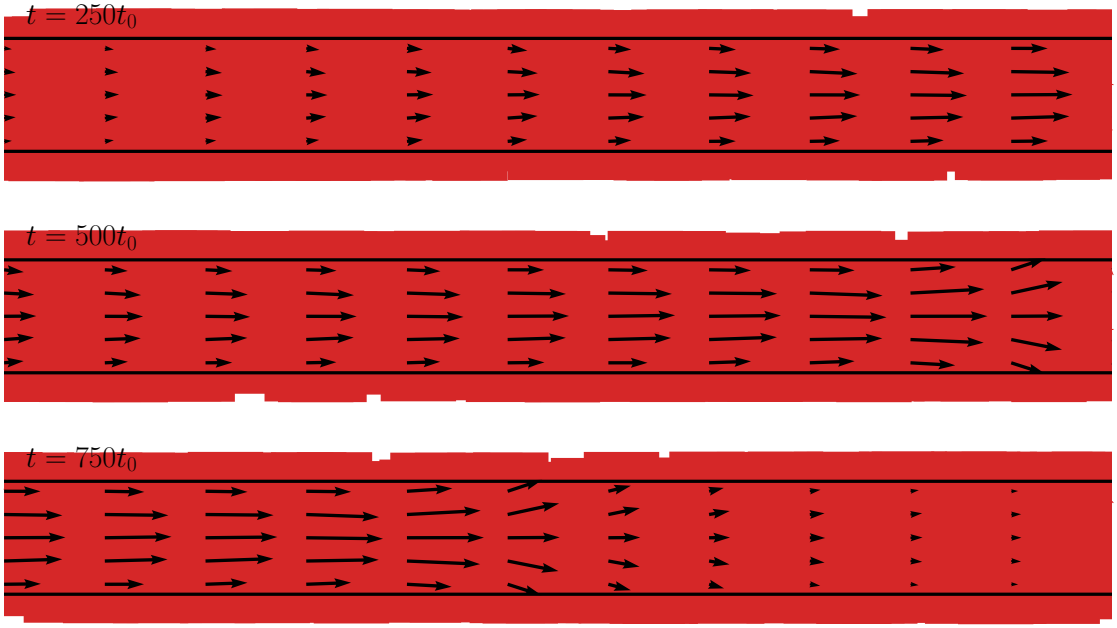

Figure 6.3: Traveling pulse at various times propagating from right to left. Flow is in the opposite direction and indicated by the black arrows. The lateral components of the flow velocity have been amplified by a factor 5 for better visibility. Contacts are indicated by red connecting lines between the colloids, where the line thickness scales linearly with the repulsive normal force $|\mathbf{F}_\mathrm{n}|$.

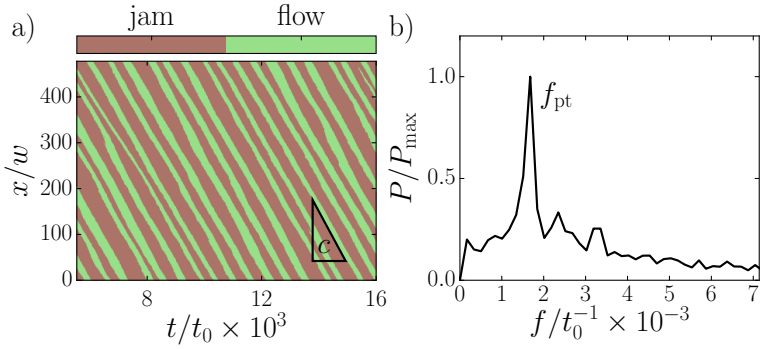

Figure 6.4: Simulation of a pulse train with parameters $\mu = 1$ and $\overline{\phi} = 0.75$. a) Spatio-temporal representation of $v(x,t)$. separated by jammed regions (brown). The velocity pulses are indicated by flowing colloidal regions (green) for mean velocity $\langle v\rangle/v_0 \geq 0.005$ or jammed regions if $\langle v\rangle/v_0 < 0.005$, with $v_0 = v(\overline{\phi} = 0)$ being the velocity in absence of colloidal particles. b) Power spectrum of $v(x,t)$ at a fixed position x. The frequency f_pt corresponds to the periodicity of the pulse train.

colloids to the walls.

Several of these rarefaction waves ultimately self organize into a regularly spaced pulse train, which moves with constant speed c. Fig. 6.4 a) shows how several pulses self-organize into a stable regular pulse train. The resulting traveling pulses are visualized as regularly spaced straight lines in the x,t plane indicating free-flow and jammed regions. The constant slope of these lines represents the propagation speed c, which

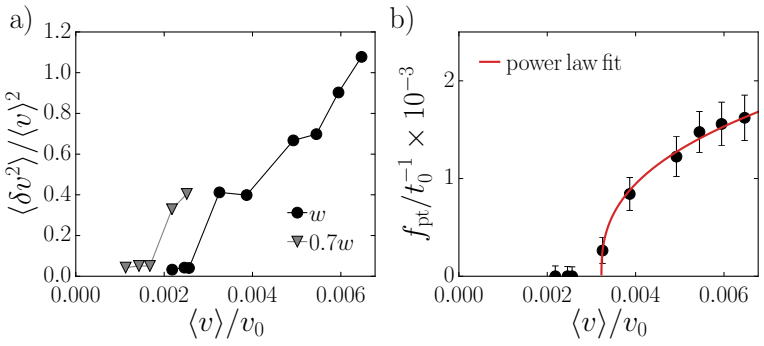

Figure 6.5: Simulation of a pulse train with parameters $\mu = 1$ and $\overline{\phi} = 0.75$ for various driving pressures σ. a) Normalized variance of $v(x,t)$ plotted versus mean flow velocity $\langle v \rangle$ for channels of width w and $0.7w$. b) Pulse train frequency $f_{\rm pt}$ versus mean flow velocity $\langle v \rangle$. Errorbars result from the finite channel length. The full red line is a power-law fit with exponent 0.379 and offset $\langle v \rangle_{\rm thr} = 0.00322 v_0$.

is negative. Moreover, the pronounced peak of the power spectrum of $v(x,t)$ in Fig. 6.4 b) also stresses the regularity of the pulse train. The frequency $f_{\rm pt} = f(P_{\rm max})$ is most represented frequency in the power spectrum and matches the inverse of the time between two pulses of the pulse train.

To quantify the strength of the traveling pulses, we introduce the variance of the flow field $\langle \delta v^2 \rangle / \langle v \rangle^2$, where $\delta v = v - \langle v \rangle$ and $\langle ... \rangle$ denotes the average over x and t. We use the variance of the flow field as an order parameter and want to find at what driving pressures gradients σ flow instabilities arise. Figure 6.5 a) shows that the pulse train emerges at a threshold value of $\langle v \rangle$, which increases with the pressure force σ. The corresponding colloidal Péclet number is large. We find that $\mathrm{Pe} = \langle v \rangle a / \overline{D} \approx 100$, where $\overline{D}$ is the measured average diffusivity of a single colloid of the binary suspension using the velocity auto correlation function inside an unconfined box (see Sect. 4.4.2). The threshold value decreases for a channel of width $2w = 35b$, which suggests that the flow instabilities are a confinement effect.

Moreover, in Fig. 6.5 b) we observe that the frequency $f_{\rm pt}$ of the pulses increase with $\langle v \rangle$, following the power law $f \propto (\langle v \rangle - \langle v \rangle_{\rm thr})^{\beta}$ with $\beta = 0.38$. This all agrees with the experimental findings of Isa *et al.* [44] (see Sect. 2.3.2).

6.2.2 Role of friction and packing density

Similar to discontinuous shear thickening in hard-sphere suspensions, the implemented Coulomb friction plays a decisive role in observing the regular pulse trains. In Fig. 6.6 we show the velocity and density profiles at one fixed position in the channel over time for various friction coefficients μ. Hereby, we also consider results generated by the theoretical value $\mu = \infty$, which simply means that contacts are without any slip. We note that after some initial runtime, equally spaced pulses are present in the cases for $\mu = \infty$ and $\mu = 1$. The peaks are accompanied by rarefaction waves at approximately $\phi \approx 0.6$ and separated by long jams, which nearly arrest the flow. Inside the jams we find a packing density of roughly $\phi \gtrsim 0.8$, which slightly increases with decreasing μ. The jams between the pulses become shorter and the pulses broader with decreasing friction coefficient. In the case of $\mu = 0.5$ the pulse train is frequently interrupted by long-lived phases of free flow.

In Fig. 6.7 a) we can summarize the behavior of the pulses with respect to the friction coefficient μ. We consider the following configurations of friction between colloids and

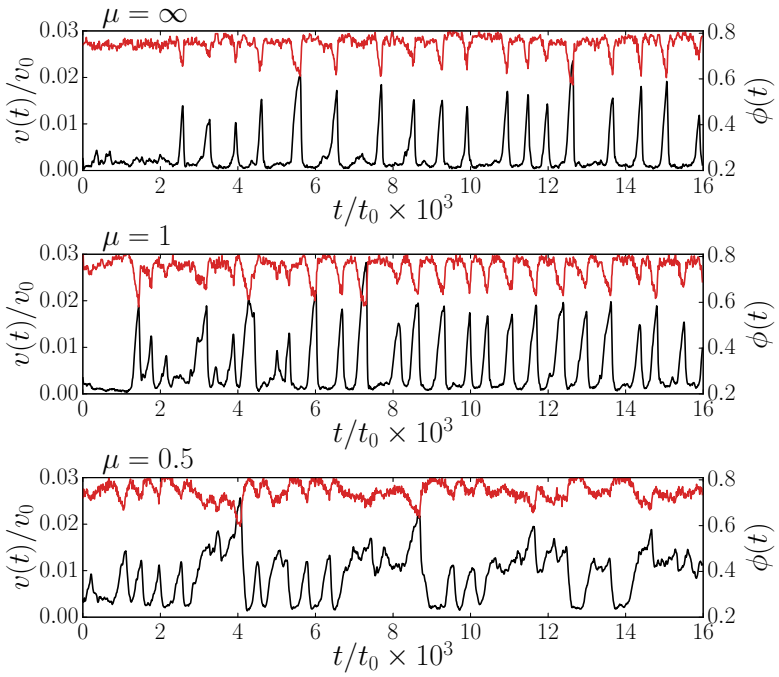

Figure 6.6: Sample profiles at $x = 0$ measured over time t for friction coefficients $\mu = \infty$, $\mu = 1$ and $\mu = 0.5$. Mean packing density is $\overline{\phi} = 0.75$. Red lines denote local packing density ϕ identified by the right axis, black lines denote local velocity v identified by the left axis, respectively.

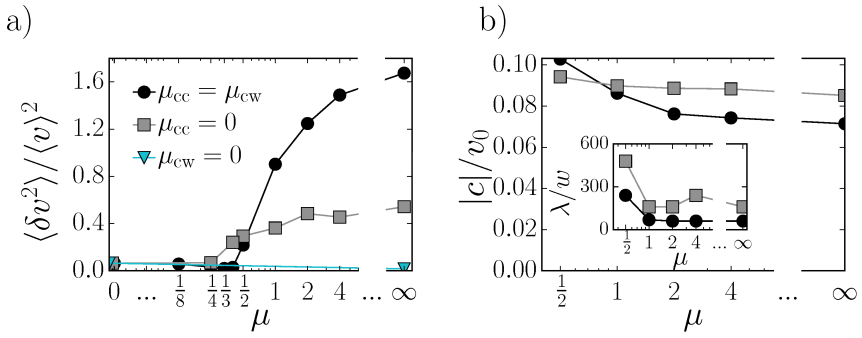

Figure 6.7: a) Pulse strength $\langle \delta v^2 \rangle / \langle v \rangle^2$ and b) pulse speed c plotted versus friction coefficient μ on logarithmic scale and for different friction compositions at $\overline{\phi} = 0.75$. Inset: Distance λ between pulses. Lines connecting the points are a guide to the eye.

between colloids and wall. In the first case, friction between colloids (μ_{cc}) and friction between colloids and wall (μ_{cw}) are equal to μ. In a continuous transition, velocity pulses emerge at $\mu \approx 0.5$ as indicated by a growing order parameter $\langle \delta v^2 \rangle / \langle v \rangle^2$, which increases sharply for larger μ and saturates in the limit $\mu \to \infty$. Note that this increase in $\langle \delta v^2 \rangle / \langle v \rangle^2$ is mainly due to the fact that the distance λ between the traveling pulses sharply decreases as indicated in the inset of Fig. 6.7 b), while the pulse height remains approximately the same as can be observed in Fig. 6.6. If the friction between the colloids is switched off, $\mu_{cc} = 0$, the distance λ is larger (see inset of Fig. 6.7 b)), which explains the overall smaller pulse strength in Fig. 6.7 a). However, more importantly for frictionless walls, $\mu_{cw} = 0$, traveling pulses do not occur even if colloidal friction is

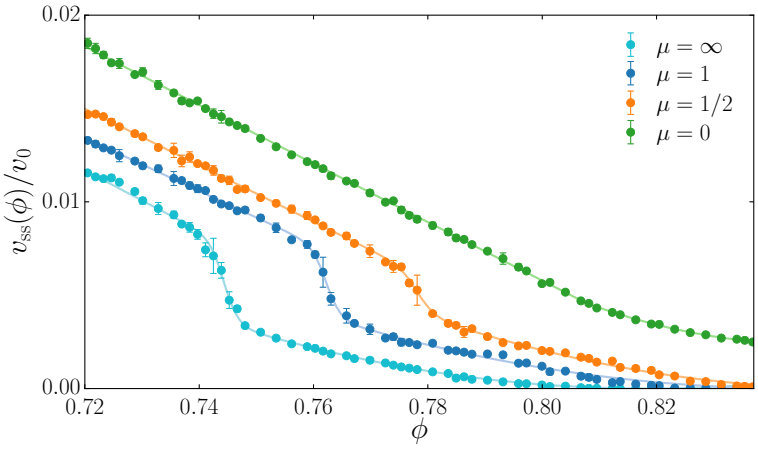

Figure 6.8: Steady-state velocity v_{ss} for various friction coefficients μ. The symbols indicate MPCD-simulation results whereas the solid lines are least-squares fits using Eq. (6.4) and the fitting parameters from Tab. 6.2. Errorbars denote single standard deviation of the mean value from 5 simulation runs.

present. Force chains spanning across the channel cannot form and thus the jammed regions, essential for the pulses to occur, cannot develop. In Fig. 6.7 b) the pulse speed c decreases close to the transition and then stays approximately constant. A similar behavior is observed for the distance λ between the pulses. Moreover, we note that the absolute value of the pulse speed c is roughly one order of magnitude larger than the mean flow speed within the channel. This was also confirmed by Isa [179].

In simulations with sufficiently short channels ($l = 200b$), the colloidal flow remains uniform. Figure 6.8 plots the flow velocity v_{ss} in this steady state versus packing fraction ϕ for different friction coefficients μ. While for zero friction, $\mu = 0$, v_{ss} decreases smoothly towards zero, for finite friction, $\mu > 0$, a jump of v_{ss} occurs at a critical density ϕ_c and one can clearly distinguish between states of free flow and jammed flow. This feature can qualitatively explain the formation of traveling pulses. The colloidal density in the free-flow regime fluctuates locally about its mean value. If such fluctuations exceed ϕ_c, the colloidal flow strongly slows down. Frictional contacts generate force chains, which further arrest the flow as more colloids accumulate upstream of the jam. Downstream, the suspension rarefies as colloids still flow freely. This rarefaction dissolves the force chains and the jammed region moves upstream.

The state diagram in Fig. 6.9 summarizes the behavior in long channels. The colloidal flow is classified as traveling pulses if $\langle \delta v^2 \rangle / \langle v \rangle^2 > 0.1$; otherwise, we refer to it as free flow for mean velocity $\langle v \rangle / v_0 \geq 0.005$ or jammed flow if $\langle v \rangle / v_0 < 0.005$. The region of traveling pulses becomes narrower and shifts to higher densities as the friction coefficient decreases. Larger densities are needed to build up force chains via frictional contacts, while rarefaction pulses cannot develop if the density is too high.

6.2.3 Classes of traveling pulse profiles

Different flow patterns of traveling pulses occur for different mean densities $\overline{\phi}$ as illustrated in Fig. 6.10. At lower densities solitary jams develop. They persist throughout the simulation and the distance between the jammed regions may vary largely. Stable and regular trains of pulses form close to the critical density $\overline{\phi} \approx \phi_c$. Finally, near the boundary to the jammed flow in Fig. 6.9 only weak solitary pulses of finite life time appear throughout the channel as evident by the green stripes, which start or end in the

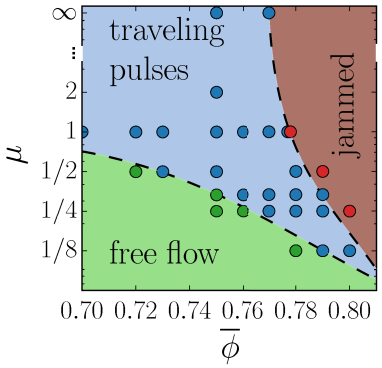

Figure 6.9: State diagram of friction μ versus mean density $\overline{\phi}$ showing jammed, traveling pulses, and free-flow regions. Friction coefficient μ is on logarithmic scale. Dots indicate conducted simulations. The lines separating the flow domains were added by hand.

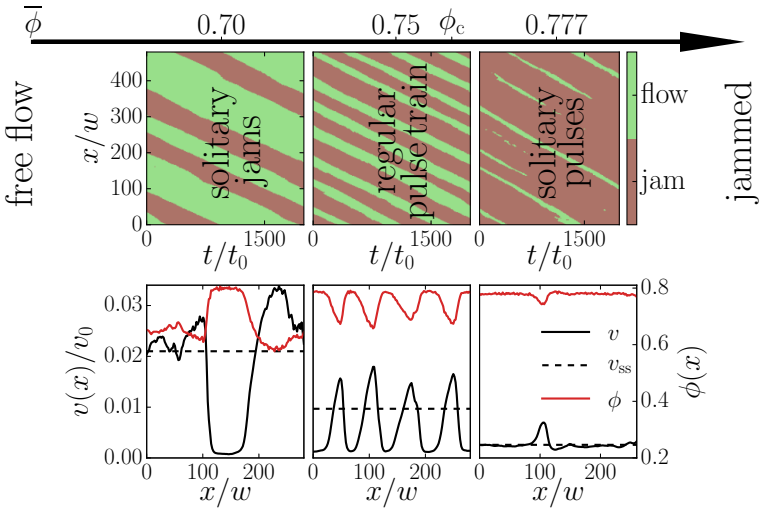

Figure 6.10: Spatio-temporal representation (top) and snapshots (bottom) of flow velocity $v(x)$ and area fraction ϕ for different mean densities $\overline{\phi}$ at $\mu = 1$. The dashed lines indicate the steady-state velocity v_{ss} at the respective mean packing density $\overline{\phi}$.

jammed flow region. Interestingly, Campbell and Haw [45] made a similar observation in an experiment on dense colloidal flow into a channel with converging cross section (see Sect. 2.3.2). They found that by slightly increasing the colloidal volume fraction, periodic oscillations in flow speed measured at the channel inlet transformed into transient pulses separated by irregular long-lived jams.

6.3 Continuum Model

In the following we present a phenomenological theory, which is able to explain and mimic our numerical results. It is motivated by continuum traffic-flow models that capture the formation of shock fronts [33], density autosolitions, and periodic density modulations [180–182].

6.3.1 Governing equations

The colloidal area fraction ϕ obeys the one-dimensional continuity equation, where the current density J includes a drift and diffusion term:

$$\frac{\partial \phi}{\partial t} + \frac{\partial J}{\partial x} = 0 \quad \text{with} \quad J = v\phi - D\frac{\partial \phi}{\partial x}. \tag{6.2}$$

Here, D represents the collective diffusivity, which is assumed constant.

For the colloidal flow velocity we use Newton's equation. From the steady-state velocity v_{ss} plotted in Fig. 6.8 we extract a density-dependent friction coefficient $\xi(\phi) = \sigma/v_{\mathrm{ss}}(\phi)$ that combines the effect of shear viscosity and colloidal contact friction. The unsteady flow velocity then obeys

$$\frac{\mathrm{d}v}{\mathrm{d}t} = \frac{\partial v}{\partial t} + v\frac{\partial v}{\partial x} = \sigma - \xi(\phi)v, \tag{6.3}$$

where we divided by the mass density. Note that Eq. (6.3) is not derived in the limit of low Reynolds numbers by not omitting the nonlinear convective part $v\frac{\partial v}{\partial x}$. However, we will see that the convective part becomes insignificant in the regime, where we observe our traveling pulses. For $\xi(\phi) = \sigma/v_{\mathrm{ss}}(\phi)$ we use an analytic function, which we obtain by fitting the data for $v_{\mathrm{ss}}(\phi)$ in Fig. 6.8. We fit our data for $v_{\mathrm{ss}}(\phi)$ by choosing a linear decline to the left of ϕ_{c} and a quadratic decay towards zero to the right of ϕ_{c}. The jump in between both regimes is fitted with a hyperbolic tangent $\tanh[(\phi_{\mathrm{c}} - \phi)/\Delta\phi]$, where $\Delta\phi$ controls its width. The fitting function then reads

$$\begin{aligned} v_{ss}^{\mathrm{fit}}(\phi) = \Delta v \left[1 + \tanh\left(\frac{\phi_{\mathrm{c}} - \phi}{\Delta\phi}\right)\right] \\ + \begin{cases} e_1 + e_2\phi & \text{if } \phi < \phi_{\mathrm{c}} \\ e_3(\phi - \phi_{\mathrm{q}})^2 & \text{if } \phi \geq \phi_{\mathrm{c}} \end{cases}. \end{aligned} \tag{6.4}$$

The fitting parameter e_3 can be eliminated by requiring that linear and quadratic part of v_{ss}^{fit} connect at ϕ_{c}, which gives $e_3 = (e_1 + e_2\phi_{\mathrm{c}})/(\phi_{\mathrm{c}} - \phi_{\mathrm{q}})^2$. The remaining parameters are determined using least-squares fits and are compiled in Tab. 6.2 for various friction coefficients μ.

	$\mu = \infty$	$\mu = 1$	$\mu = 1/2$	$\mu = 0$
Δv	0.0489	0.0413	0.0247	0.0005
$\Delta\phi$	0.00247	0.0025	0.00312	0.00233
ϕ_{c}	0.744	0.762	0.778	0.808
e_1	2.82	2.56	2.78	2.90
e_2	-3.68	-3.24	-3.45	-3.53
ϕ_{q}	0.819	0.845	0.854	0.846

Table 6.2: Fitting values of $v_{\mathrm{ss}}(\phi)$ for various friction coefficients μ.

Finally, the system Eq. (6.2) and (6.3) can be normalized by introducing characteristic time $\tau = \left(D/\sigma^2\right)^{1/3}$ and length $\eta = \left(D^2/\sigma\right)^{1/3}$. We rewrite the variables by performing $t/\tau \to t$, $x/\eta \to x$, $v\tau/\eta \to v$ and $\xi\tau/ \to \xi$ in order to obtain

$$\frac{\partial \phi}{\partial t} + \frac{\partial \phi v}{\partial x} = \frac{\partial^2 \phi}{\partial x^2} \tag{6.5}$$

$$\frac{\partial v}{\partial t} + v\frac{\partial v}{\partial x} = 1 - \xi(\phi)v. \tag{6.6}$$

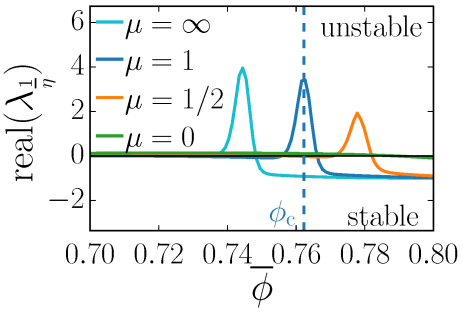

Figure 6.11: Real part of the eigenvalue $\lambda_{\frac{1}{\eta}}$ with respect to mean packing fraction $\overline{\phi}$ with $\xi(\phi)$ sampled for various μ.

6.3.2 Linear stability analysis

We now conduct a stability analysis of the Eqs. (6.5)-(6.6) in order to investigate, for which parameters the trivial solution $\phi(x,t) = \overline{\phi}$ and $v(x,t) = \overline{v} = 1/\xi(\overline{\phi})$, which represents homogeneous flow, is stable. We linearize Eq. (6.5) and (6.6) around the homogeneous solution, $\phi = \overline{\phi} + \delta\phi$ and $v = \overline{v} + \delta v$, and neglect higher-order terms, so that we obtain

$$\frac{\partial \delta\phi}{\partial t} = -\overline{\phi}\frac{\partial \delta v}{\partial x} - \frac{1}{\xi}\frac{\partial \delta\phi}{\partial x} + \frac{\partial^2 \delta\phi}{\partial x^2}, \tag{6.7}$$

$$\frac{\partial \delta v}{\partial t} = -\frac{1}{\xi}\frac{\partial \delta v}{\partial x} - \frac{1}{\xi}\left.\frac{\mathrm{d}\xi}{\mathrm{d}\phi}\right|_{\overline{\phi}} \delta\phi - \xi\delta v. \tag{6.8}$$

We substitute the following plane-wave ansatz: $\delta\phi = \phi_k \exp(ikx - \lambda_k t)$ and $\delta v = v_k \exp(ikx - \lambda_k t)$, which represents an oscillating harmonic perturbation of the system around $(\overline{\phi}, \overline{v})$. Here λ_k denotes an eigenvalue with the dimension of a frequency and with respect to wavelength k. Writing the linearized equations in matrix form, we then find

$$\lambda_k \begin{pmatrix} \delta\phi \\ \delta v \end{pmatrix} = \begin{pmatrix} -ik\frac{1}{\xi} - k^2 & -ik\overline{\phi} \\ -\frac{1}{\xi}\left.\frac{\mathrm{d}\xi}{\mathrm{d}\phi}\right|_{\overline{\phi}} & -\xi - ik\frac{1}{\xi} \end{pmatrix} \begin{pmatrix} \delta\phi \\ \delta v \end{pmatrix}. \tag{6.9}$$

By defining $\lambda_k^* = \lambda_k + ik\frac{1}{\xi}$, we can simplify the equations to

$$\lambda_k^* \begin{pmatrix} \delta\phi \\ \delta v \end{pmatrix} = \begin{pmatrix} -k^2 & -ik\overline{\phi} \\ -\frac{1}{\xi}\left.\frac{\mathrm{d}\xi}{\mathrm{d}\phi}\right|_{\overline{\phi}} & -\xi \end{pmatrix} \begin{pmatrix} \delta\phi \\ \delta v \end{pmatrix}. \tag{6.10}$$

The eigenvalues λ_k can then be computed from Eq. (3.93), and read

$$\lambda_k^* = \frac{-k^2 - \xi}{2} \pm \sqrt{\left(\frac{-k^2 - \xi}{2}\right)^2 - \xi k^2 + ik\frac{\overline{\phi}}{\xi}\left.\frac{\mathrm{d}\xi}{\mathrm{d}\phi}\right|_{\overline{\phi}}}. \tag{6.11}$$

In Fig. 6.11 we find the stability analysis for perturbations with wavelength equal to our characteristic length so that $k = 1/\eta$. The result suggests that the trivial homogeneous solution becomes linearly unstable close to the critical density ϕ_c for $\mu > 0$. Beyond ϕ_c the suspension is jammed and a homogeneous flow profile stable against perturbations. In the case of $\mu = 0$ the eigenvalue is close to zero for most packing fraction, which makes any statement on stability difficult. Since no traveling pulses were observed for $\mu = 0$ in our simulation, we can conclude that the instability is not strong and localized enough to trigger pulse formation.

6.3.3 Traveling wave equations

Next, we want to analyze in what shape the instabilities arise. In doing so, we search for traveling wave solutions of the form $\phi(z)$ and $v(z)$ with $z = x - ct$ and where c is the dimensionless propagation speed of the traveling wave. Using this ansatz and the chain rule, we can rewrite the equations and obtain for Eq. (6.5)

$$\frac{\mathrm{d}}{\mathrm{d}z} \underbrace{\left[\phi(v-c) - \frac{\mathrm{d}\phi}{\mathrm{d}z}\right]}_{\text{flux in co-moving frame}} = 0. \tag{6.12}$$

Eq. (6.12) demands that the sum of diffusive flux and convective flux relative to c, need to be constant along z. After integration we denote this constant q and yield the traveling wave equations (TWE) for our system

$$\frac{\mathrm{d}\phi}{\mathrm{d}z} = (v-c)\phi - q \tag{6.13}$$

$$\frac{\mathrm{d}v}{\mathrm{d}z} = \frac{1-\xi(\phi)v}{v-c} \quad \text{with} \quad c \neq v. \tag{6.14}$$

The equations (6.13)-(6.14) form a closed set of non-linear ordinary differential equations with respect to a spatial coordinate z. They define a set of trajectories in the ϕ,v phase space that can be obtained by numerical integration.

We can use Eq. (6.13) to derive an expression for the pulse speed c. Imagine a jammed region traveling along an infinitely long channel with mean area fraction $\overline{\phi} < \phi_\mathrm{c}$. Within the jam the density is $\phi_\mathrm{j} > \phi_\mathrm{c}$ and the particles creep with a velocity v_j. At infinity as well as at the peak value in the jam, the derivative of ϕ vanishes and thus in both cases one can write $q = [v_\mathrm{ss}(\overline{\phi}) - c]\overline{\phi} = (v_\mathrm{j} - c)\phi_\mathrm{j}$. This yields an expression for the pulse speed,

$$c = \frac{\phi_\mathrm{j} v_\mathrm{j} - \overline{\phi} v_\mathrm{ss}(\overline{\phi})}{\phi_\mathrm{j} - \overline{\phi}} \approx -\frac{\overline{\phi}}{\phi_\mathrm{j} - \overline{\phi}} v_\mathrm{ss}(\overline{\phi})\,. \tag{6.15}$$

To arrive at the second equation, we used $v_\mathrm{j} \ll v_\mathrm{ss}$ and $\phi_\mathrm{j} \approx \overline{\phi}$. Now, since $0 < (\phi_\mathrm{j} - \overline{\phi})/\overline{\phi} \ll 1$ in our simulations, Eq. (6.15) confirms our findings that the pulse speed c is negative and that the pulse always travels against the colloidal flow with a speed much larger than $v_\mathrm{ss}(\overline{\phi})$.

6.3.4 Analysis of the phase portrait

As mentioned above, the equations (6.13)-(6.14) define trajectories in the ϕ,v phase space, which can be drawn for arbitrary starting positions. This geometric representation of the behavior of the system is called phase portrait, which was introduced in Sec. 3.4. Closed trajectories in the ϕ,v phase portrait correspond to periodic traveling wave solutions of the partial differential equations (PDE) (6.5-6.6). We study the behavior in the phase portrait by varying the unknown parameters q and c. We start by determining the Nullclines, from equations (6.13-6.14). In the phase portrait these lines correspond to a zero-growth rate of ϕ or v, respectively. We obtain them by demanding $\mathrm{d}\phi/\mathrm{d}z = 0$ and $\mathrm{d}v/\mathrm{d}z = 0$, which yields

$$v_{N1}(\phi) = \frac{q}{\phi} + c, \tag{6.16}$$

$$v_{N2}(\phi) = \frac{1}{\xi(\phi)} = v_\mathrm{ss}(\phi). \tag{6.17}$$

Only the Nullcline v_{N1} depends on the unknowns q and c, whereas $v_{N2}(\phi)$ is equal to the steady state velocity $v_\mathrm{ss}(\phi)$. Both are plotted in Fig. 6.12.

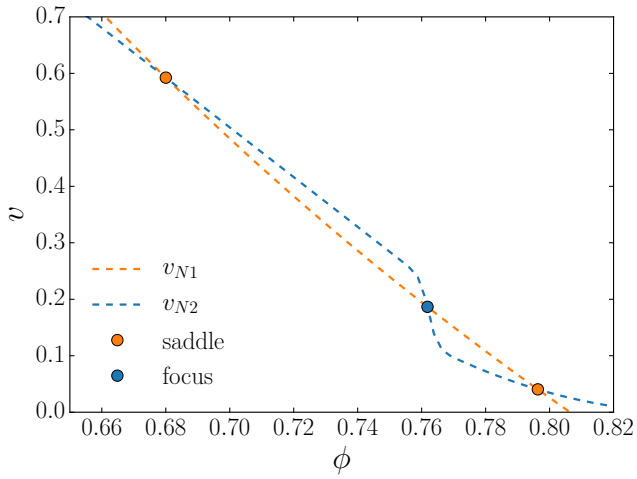

Figure 6.12: Example Nullclines in the ϕ,v plane and their intersection points for one choice of parameters c and q and $\xi(\phi)$ sampled for $\mu = 1$. Parameters are $c = 3$ and $q = -2.6$

Classification of fixed points

The intersections of both Nullclines define fixed points (ϕ_0, v_0). As a result, trajectories in their vicinity approach or leave them at $z \to \pm\infty$. Solutions directly at the fixed points correspond to homogeneous solutions of the PDE ($\phi(x,t) = \phi_0$ and $v(x,t) = v_0$). The Nullcine v_{N1} decays from infinity at $\phi = 0$ to c as ϕ increases. Since $c < 0$ if $v > 0$, it intersects v_{N2} at least once. In fact, for a range of q and c there exist up to 3 fixed points in the system (see Fig. 6.12), for which holds $v_{N1}(\phi_0) = v_{N1}(\phi_0)$. Using Eq. (6.16-6.17) and rearrange, this condition reads

$$q = \phi_0(v_0 - c) \quad \text{with} \quad v_0 = v_{\text{ss}}(\phi_0). \tag{6.18}$$

In order to classify ϕ_0 and v_0, we linearize Eqs. (6.13) and (6.14) around $\phi = \phi_0 + \delta\phi e^{\lambda z}$ and $v = v_0 + \delta v e^{\lambda z}$. This first order approximation of the equations allows to study the behavior of trajectories close to the fixed points by calculating the eigenvalues λ (compare Sect. 3.4.2). In matrix form the equations reduce to the eigenvalue problem

$$\lambda \begin{pmatrix} \delta\phi \\ \delta v \end{pmatrix} = \begin{pmatrix} v_0 - c & \phi_0 \\ -\frac{v_0}{v_0 - c} \left.\frac{\mathrm{d}\xi}{\mathrm{d}\phi}\right|_{\phi_0} & \frac{-\xi(\phi_0)}{v_0 - c} \end{pmatrix} \begin{pmatrix} \delta\phi \\ \delta v \end{pmatrix}. \tag{6.19}$$

The eigenvalues are determined by Eq. (3.93) and read

$$\lambda_{1/2} = \frac{1}{2}\left(v_0 - c - \frac{\xi(\phi_0)}{v_0 - c}\right) \pm \sqrt{\frac{1}{4}\left(v_0 - c - \frac{\xi(\phi_0)}{v_0 - c}\right)^2 + \xi(\phi_0) - \frac{v_0\phi_0}{(v_0 - c)} \left.\frac{\mathrm{d}\xi}{\mathrm{d}\phi}\right|_{\phi_0}}. \tag{6.20}$$

In analogy to the stability analysis of dynamic systems, positive real parts of the eigenvalues $\lambda > 0$ correspond to trajectories leaving the fixed point as perturbations $\delta\phi e^{\lambda z}$ and $\delta v e^{\lambda z}$ will grow along positive z. Contrary, negative real parts will result in trajectories approaching the fixed points at $z = \infty$. Complex eigenvalues correspond to spiraled trajectories centered at the fixed point. In our 2 dimensional system two eigenvalues $\lambda_{1/2}$ are associated with each fixed point (ϕ_0, v_0), which allows for different combinations illustrated in Fig. 6.13.

In Fig. 6.14 left, the different classes of fixed points are shown for the our system dependent on wave speed c and their location ϕ_0 on the phase portrait. In this case the

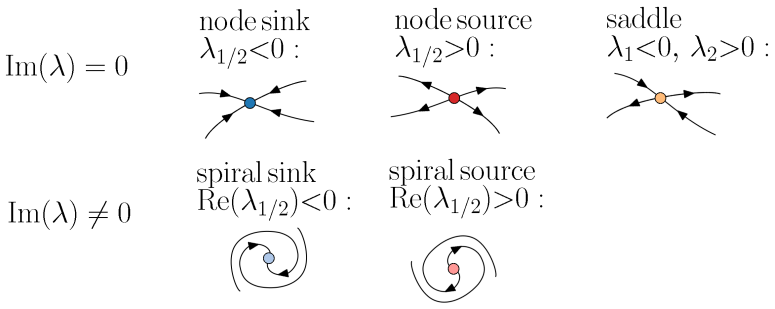

Figure 6.13: Classification of the fixed points in a 2 dimensional system with schematic trajectories.

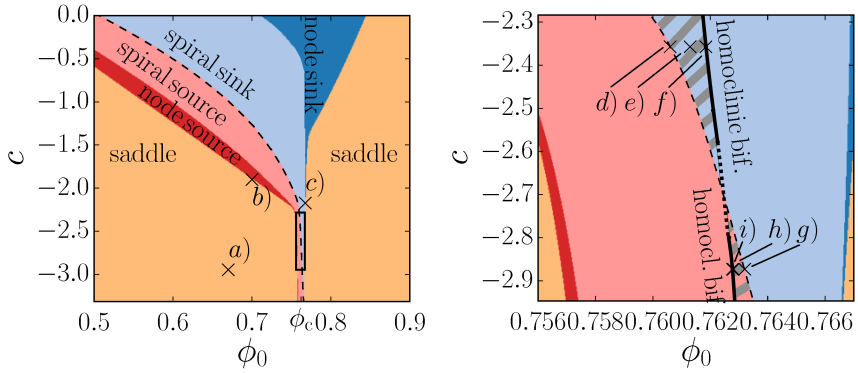

Figure 6.14: Left: Classification of the fixed points of the system (6.13) and (6.14) using Eq. (6.20) for $\xi(\phi)$ sampled for $\mu = 1$. The dashed line indicates a Hopf bifurcation at the fixed point. Right: Zoomed in box view. In the striped areas limit cycles exist. Solid black line corresponds to a homoclinic bifurcation. Sample plots of phase portraits a)-l) below.

parameter q is exchanged for the parameter ϕ_0, the location of a fixed point, by using Eq. (6.18). Now, for each point on (c, ϕ_0) one can draw a phase portrait. Moving along the parameter space (c, ϕ_0) the property of a fixed point might vary as it changes sign or becomes complex. That change of properties of fixed points is commonly referred to as local bifurcation, which alter the qualitative behavior of the system drastically where ever they occur (see Sect. 3.4.3). Different kinds of bifurcation that can be observed in our dynamical system will be discussed below.

In Fig. 6.12 we showed a configuration with 3 fixed points. However, not for all choices of (c, ϕ_0) there will be 3 fixed points in the system. For example, the phase portrait at a) has only one fixed point as show in Fig. 6.15a), which can be identified as a saddle. This fixed point inherits a repelling and attractive manifold so that all trajectories arrive from infinite values and thrive to infinite values of v and ϕ, which can not correspond to a physical trajectory. As a result, in the case of only one fixed point, no steady state traveling wave solutions exist, but the trivial homogeneous solution at the fixed point.

Phase portraits with two fixed points exist only in cases of both Nullclines crossing at one point and being tangent at another point as illustrated in Fig. 6.15b) and c). This is exactly the case along the border line between saddle and sink as well as between saddle and source, where two fixed points collide in Fig. 6.14 left. This is known as a saddle-node bifurcation, which is characterized by one of the eigenvalues λ becoming zero

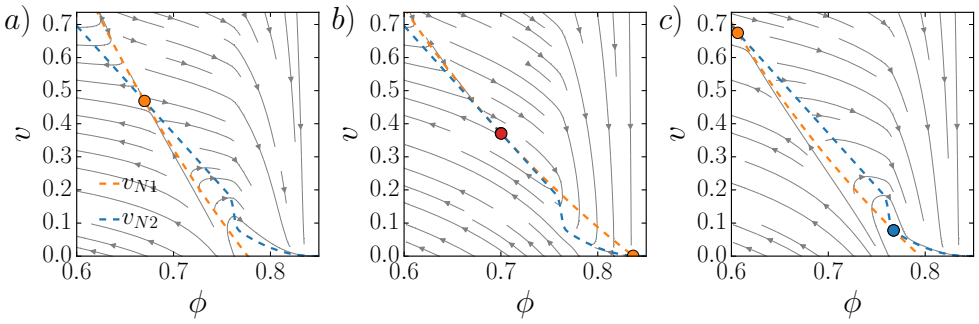

Figure 6.15: Example phase portraits for cases of one or two fixed points.

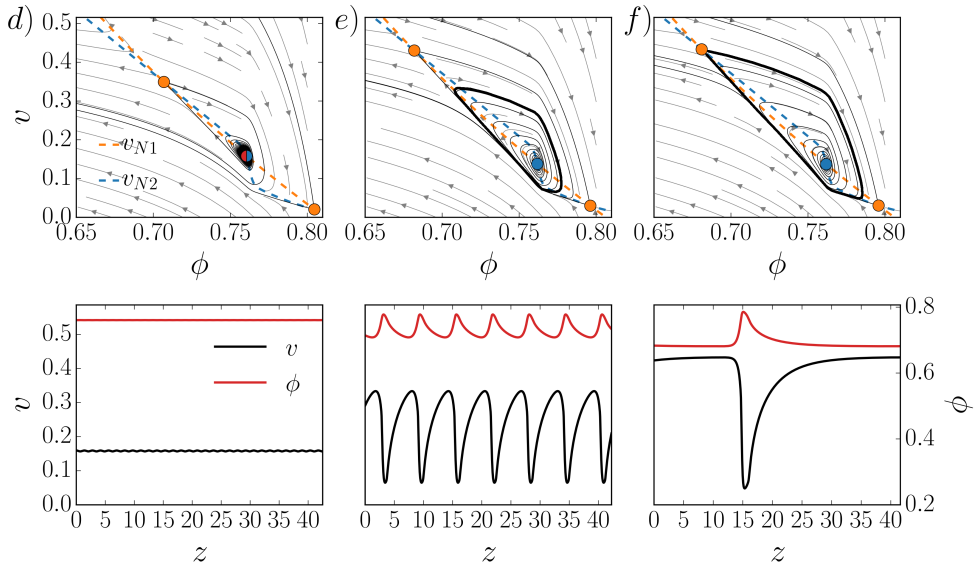

Figure 6.16: Example phase portraits and profiles between a subcritical Hopf bifurcation and a homoclinic bifurcation.

(see Sect. 3.4.3). The second fixed point is a saddle. Along the lines of the saddle-node bifurcation, closed trajectories were not found by us.

If the Nullclines intersect in three points, the fixed point located in between the others becomes either a node or a spiral. For large enough $|c|$, this fixed point is located close to the critical density ϕ_c of the system, as can be seen from Fig. 6.14 left. The two other fixed points are saddles and are located on the free flow branch and on the jammed flow branch of $v_{eq}(\phi)$ as in Fig. 6.12.

As introduced in Sect. 3.4.3, we speak of a Hopf bifurcation, when the eigenvalues of a fixed point cross the complex plane imaginary axis, that is when a focus sink becomes a focus source or vice versa along the dashed line in Fig. 6.14. The parameters, for which the Hopf bifurcation occurs can be found analytically from Eq. (6.20) by demanding that the real part of λ vanishes:

$$v_0 - c - \frac{\xi(\phi_0)}{v_0 - c} = 0 \quad \text{and} \quad \xi(\phi_0) - \frac{v_0 \phi_0}{(v_0 - c)} \left.\frac{\mathrm{d}\xi}{\mathrm{d}\phi}\right|_{\phi_0} < 0. \tag{6.21}$$

At a Hopf bifurcation a small-amplitude limit cycle appears around the focus. A limit cycle in our system Eq. (6.13-6.14) corresponds to a periodic and in z stationary solution of a traveling wave.

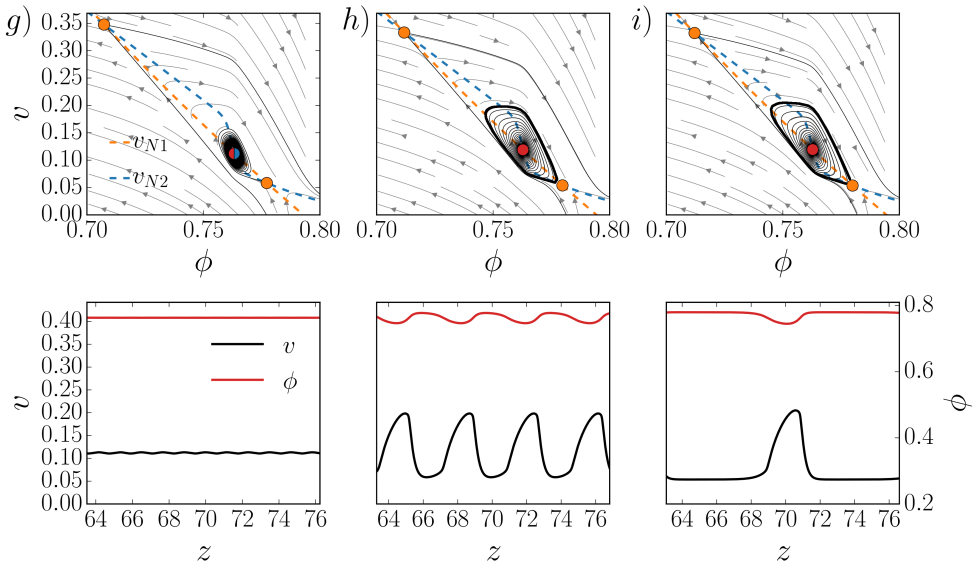

Figure 6.17: Example phase portraits and profiles between a supercritical Hopf bifurcation and a homoclinic bifurcation.

The striped area in Fig. 6.14 right, marks the parameter space, where a limit cycle occurs. The area is bounded by the Hopf bifurcation on one side, where the limit cycle emerges, and by a homoclinic bifurcation on the other side, where the limit cycle has grown to a size that it collides with one of the saddles. At the homoclinic bifurcation the limit cycle becomes a homoclinic orbit with period infinity. Beyond the homoclinic bifurcation the limit cycle no longer exists.

Noteworthy is that the fixed point ϕ_0, for which limit cycles exist swaps from a focus sink to a focus source as $|c|$ is increased. As a result, the subcritical Hopf bifurcation becomes supercritical as $|c|$ is increased (see Sect. 3.4.3). Numerically it is challenging to obtain limit cycles close to this transition, because the real part of the eigenvalues is close to zero and trajectories converge only very slowly to the limit cycle. We mark this area with the dotted line in Fig. 6.14 right.

Phase portraits plotting trajectories, fixed points and nullclines can be found in Fig. 6.16 and 6.17. Arrows on the trajectories point towards direction of positive z. Limit cycles are highlighted with a thicker line. The limit cycles are plotted with respect to z on the bottom of the respective phase portrait.

In Fig. 6.16 *d*) and Fig. 6.16 *g*), the fixed point ϕ_0 lies directly on the Hopf bifurcation, which marks the birth of a small amplitude limit cycle. As the absolute value of the real part of ϕ_0 increases, amplitude and period of the limit cycle grow as displayed in *e*) and *h*). Further increasing the absolute value of the real part leads the limit cycle to touch a saddle point, which marks the homoclinic bifurcation. In Fig. 6.16 *f*), the limit cycle collides with the saddle point located on the free flow branch of v_{ss}. At larger values of $|c|$ in Fig. 6.17 *i*) however, the limit cycle collides with the saddle point located on the jammed flow branch of v_{ss}.

6.3.5 Modeling traveling pulses

Finally, we use our findings from the phase portrait analysis to model the different type of rarefaction pulses illustrated in Fig. 6.10. In Fig. 6.18 c) we plot the different types of traveling waves that we observed in our MPCD simulations. The respective parameters ϕ_0 and c, are indicated by the markers *I-III* in Fig. 6.18 a). The subcritical Hopf

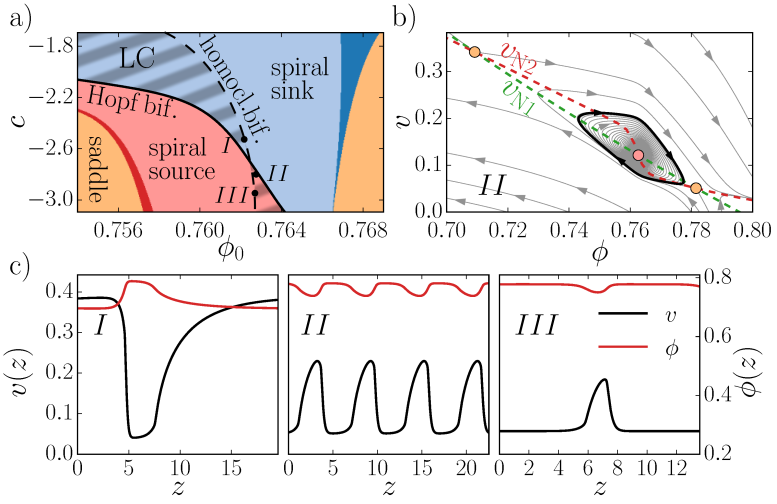

Figure 6.18: a) Classification of fixed points in the c, ϕ_0 plane for Eqs. (6.13-6.14) using $v_{ss} = \xi^{-1}$ for $\mu = 1$. Within the striped area limit cycles (LC) exist. b) Phase portrait for $q = 2.228$ and $c = -2.8$ showing a limit cycle that corresponds to periodic pulse train. The nullclines v_{N1}, v_{N2} intersect in three fixed points classified by the color code of a). c) Flow velocity v and packing density ϕ profiles generated by closed orbits in the phase portrait for parameters marked with *I-III* in a).

bifurcation results in a periodic orbit that, if increased further touches the saddle on the free flow branch of $v_{ss}(\phi)$. The respective homoclinic orbit can be interpreted as a solitary traveling jam with propagation speed c. The profile resembles that of the traveling jam presented in Fig. 6.10. It captures well the features of a wide jam with a gradual unjamming front downstream and a sharp jamming front upstream. The profile of the periodic orbit in Fig. 6.18 b), occurring between Hopf and homoclinic bifurcation, represents the solution of a regular pulse train in our MPCD simulations. At the largest pulse speeds c, the Hopf bifurcations become supercritical and the periodic orbit collides with the saddle located at the jammed branch of $v_{ss}(\phi)$. This results in a homoclinic orbit that resembles a solitary traveling pulse, similarly to the one observed in Fig. 6.10

Noteworthy is that because we find our simulated traveling pulses in the regime, where $|c| \gg v$, we can place our phenomenological model in the low Reynolds number regime. This is best seen in Eq. (6.3), where the nonlinear term gives rise to v in the denominator $v - c$ in Eq. (6.14). As we restrict our analysis in Fig. 6.18 to the case of large pulse velocities in accordance with our simulations and the experiments, the nonlinear convective term in Eq. (6.3) has little to no effect on our results.

6.4 Summary and Conclusion

The numerical model using MPCD and a frictional spring model between the colloids, reproduces all features of the experimental counterpart including traveling pulse trains or rarefaction pulses moving upstream. It identifies a transition between free and jammed flow due to force chains spanning the channel cross section as the crucial reason for the formation of flow instabilities. They include solitary jams, regular pulse trains, and solitary pulses, which set in with increasing density, wall-colloid friction, and flow velocity. A nonlinear phenomenological model, which we analyzed with methods from nonlinear dynamics to identify traveling wave solutions, is able to describe all the traveling pulse profiles from our simulations. Thereby, we identify periodic orbits in the phase portrait

as periodic pulse trains in our simulations. Solitary pulses or jams can be identified as homoclinic orbits in the traveling wave equations. The findings are a good example of how the unifying idea of jamming determines the complex flow of dense colloidal systems. Our insights may help in eliminating unwanted nozzle clogging in industrial processing [183, 184], by either decreasing packing density, wall friction or flow speed.

7 Conclusions

We employed the mesoscale simulation method of multi-particle collision dynamics to simulate the pressure driven flow of dense colloidal suspensions inside a channel in two and three dimensions. To solve the Navier-Stokes equations including thermal noise, the method generates a flow field using pointlike fluid particles, which perform alternating streaming and collision steps. The collision step conserves translational and angular momentum as well as temperature using the Andersen thermostat for the collision rule. To place passive particles into the flow, we combined MPCD with two models commonly used in simulating granular matter. These models implement hard frictional contacts between the colloids. The first method is based on an event-driven molecular dynamics approach and was used for intermediate packing densities. In this model, collisions are scheduled into a queue and the collisions are resolved elastically and instantaneously. The second model uses linear spring forces to generate normal and tangential forces between the colloids that obey Coulomb's law of friction. At the cost of making the particles "soft", this model was very fast in the densely packed regime, where it was applied. Moreover, in contrast to the event-driven approach, it allows for simulating force chains and jamming.

Previous experimental work on pressure-driven colloidal flow in microchannels showed that particles migrate towards the channel center. The authors argued that this mechanism emerges from interactions between sheared colloidal particles that lead to an irreversible separation from each other orthogonal to the shear due to frictional contacts. By using a binary suspension of particle species with different sizes, it was found that the particles demix, favoring the larger species in the channel center. Based on these findings, we presented a detailed parameter study on how binary colloidal suspensions demix in the center of a microchannel. We also found that the larger species enriches the center while the smaller species is driven towards the channel walls. We found this to be true in two and in three dimensions as well as for a wide range of parameters, such as size ratio, mean packing fraction, Péclet number, and concentration ratio. Using our simulation results, we extended an existing phenomenological model of shear-induced migration to account for binary suspensions. Thereby, we introduced collective diffusivity into the model, which predicts locally the down-gradient diffusion of each species. This model gave good predictions, on which species enriches the center as well as the strength of segregation. Additionally, it was able to detect the fine differences of the profiles between two and three dimensions. For three dimensions, shear migration usu-

ally developed stronger segregation, which we attributed to a larger number of collisions between the colloids. Our model can easily be extended to more than two species when the respective closure relations are known. The conclusions drawn from our model can help to overcome undesired demixing inside channel geometries. On the other hand, it can support the industrial application of shear-induced segregation for micro-filtration.

In the last part of this thesis, we presented results on suspensions near random close packing. Our simulations were motivated by the experimental observations of regular and irregular velocity oscillations inside microchannels. These oscillation emerged at a threshold value of the applied pressure gradient and were attributed to colloidal jamming by the authors. Using a combination of MPCD and the linear-spring model with Coulomb friction for colloidal interactions, we were able to simulate jamming inside the channel. Upon formation of a jam, colloids still freely move downstream of the jam, thus producing a section with decreased density. Upstream of the jam, particles accumulate and jam as well. After a short time, this procedure generates velocity pulses traveling upstream, which self-organize to a regular pulse train at intermediate densities. We found that these pulses emerge at a pressure threshold, which decreases for more narrow confinements. In agreement with the experiment, we detected a power-law behavior between pulse frequency and mean flow velocity. Additionally, we identified friction between channel walls and colloids as a requirement for jamming and velocity oscillations to occur. By tuning the mean packing fraction inside the channel we observed different traveling structures. The suspensions exhibit solitary traveling jams, well below the critical density, at which particles jam. Above the critical density, the suspension is mainly jammed and exhibits solitary traveling pulses, which we found to be unstable.

We were able to explain the variety of the traveling pulses with a newly formulated phenomenological model. The model consists of a conservation law for mass and Newton's equation of motion with friction. The expression for the friction was obtained by fitting measured flow velocities inside a short channel for various packing densities. The profiles were generated from stationary solutions of the traveling wave equations. Hereby, a limit cycle in the phase portrait corresponds to a periodic pulse train, which compared nicely to our simulations. Also homoclinic cycles could be generated by the model, which captured the features of our simulated solitary jams or pulses. The findings demonstrate how the unifying idea of jamming determines the complex flow of dense colloidal systems. They suggest that repulsive walls, that reducing colloid-wall friction, packing fraction, or flow speed prevent colloidal jamming. These insights may help in addressing unwanted channel or nozzle clogging in industrial processing.

Bibliography

[1] W. B. Russel, D. A. Savelle, and W. R. Schowalter. *Colloidal Dispersion*. Cambridge University Press, 1981.

[2] P. N. Pusey. *Colloidal suspensions. In Liquids, freezing and glass transition (ed. J. P. Hansen, D. Levesque, and J. Zinn-Justin), Elsevier, Amsterdam*, page 765, 1991.

[3] J. K. Dhont. *An introduction to dynamics of colloids*. Elsevier, 1996.

[4] J. C. Conrad, S. R. Ferreira, J. Yoshikawa, R. F. Shepherd, B. Y. Ahn, and J. A. Lewis. *Curr. Opin. Colloid Interface Sci.*, 16:71, 2011.

[5] R. G. Winkler, D. A. Fedosov, and G. Gompper. *Curr. Opin. Colloid Interface Sci.*, 19:594, 2014.

[6] M. D. Haw. *Phys. Rev. Lett.*, 92:185506, 2004.

[7] M. T. Roberts, A. Mohraz, K. T. Christensen, and J. A. Lewis. *Langmuir*, 23: 8726, 2007.

[8] A. Bricard, J. Caussin, N. Desreumaux, O. Dauchot, and D. Bartolo. *Nature*, 503: 95, 2013.

[9] H. M. Lopez, J. Gachelin, C. Douarche, H. Auradou, and E. Clement. *Phys. Rev. Lett.*, 115:028301, 2015.

[10] T. J. Ober, D. Foresti, and J. A. Lewis. *Proc. Natl. Acad. Sci. USA*, 112:12293, 2015.

[11] J. R. Royer, D. L. Blair, and S. D. Hudson. *Phys. Rev. Lett.*, 116:188301, 2016.

[12] I. R. Peters, S. Majumdar, and H. M. Jaeger. *Nature*, 532:214, 2016.

[13] J. Happel and H. Brenner. *Low Reynolds number hydrodynamics: with special applications to particulate media*. Springer Science & Business Media, 2012.

[14] J. Goyon, A. Colon, G. Ovarlez, A. Ajdari, and L. Bocquet. *Nature*, 454:84, 2008.

[15] P. Chaudhuri, V. Mansard, A. Colin, and L. Bocquet. *Phys. Rev. Lett.*, 109: 036001, 2012.

[16] G. Belfort, R. H. Davis, and A. L. Zydney. *J. Membr. Sci.*, 96:1, 1994.

[17] G. Brans. *Design of membrane systems for fractionation of particle suspensions*. PhD thesis, Wageningen University, 2006.

[18] E. C. Eckstein, D. G. Bailey, and A. H. Shapiro. *J. Fluid Mech.*, 79:191, 1977.

[19] D. Leighton and A. Acrivos. *J. Fluid Mech.*, 181:415, 1987.

[20] F. Gadala-Maria and A. Acrivos. *J. Rheol.*, 24:799, 1980.

[21] J. R. Abbott, N. Tetlow, A. L. Graham, S. A. Altobelli, F. Eiichi, L. A. Mondy, and T. S. Stephens. *J. Rheol.*, 35:773, 1991.

[22] R. J. Phillips, R. C. Armstrong, R. A. Brown, A. L. Graham, and J. R. Abbott. *Phys. Fluids*, 4:30, 1992.

[23] A. W. Chow, S. W. Sinton, J. H. Iwamiya, and T. S. Stephens. *Phys. Fluids*, 6: 2561, 1994.

[24] C. J. Koh, P. Hookham, and L. G. Leal. *J. Fluid Mech.*, 266:1, 1994.

[25] M. Frank, D. Anderson, E. R. Weeks, and J. F. Morris. *J. Fluid Mech.*, 493:363, 2003.

[26] D. Semwogerere, J. F. Morris, and E. R. Weeks. *J. Fluid Mech.*, 581:437, 2007.

[27] C. Gao and J. F. Gilchrist. *Phys. Rev. E*, 77:025301, 2008.

[28] G. Segré and A. Silberberg. *Nature*, 189:209, 1961.

[29] C. Prohm, M. Gierlak, and H. Stark. *Eur. Phys. J. E*, 35:80, 2012.

[30] C. Prohm and H. Stark. *Lab Chip*, 14:2115, 2014.

[31] M. E. Cates, J. P. Wittmer, J. P. Bouchaud, and P. Claudin. *Phys. Rev. Lett.*, 81: 1841, 1998.

[32] E. I. Corwin, H. M. Jaeger, and S. R. Nagel. *Nature*, 435:1075, 2005.

[33] M. J. Lighthill and G. B. Whitham. *Proc. R. Soc. A*, 229:317, 1955.

[34] L. F. Henderson. *Nature*, 229:381, 1971.

[35] D. Helbing and P. Molnar. *Phys. Rev. E*, 51:4282, 1995.

[36] A. Fall, N. Huang, F. Bertrand, G. Ovarlez, and D. Bonn. *Phys. Rev. Lett.*, 100: 018301, 2008.

[37] E. Brown and H. M. Jaeger. *Rep. Prog. Phys.*, 77:046602, 2014.

[38] A. J. Liu and S. R. Nagel. *Nature*, 396:21, 1998.

[39] P. A. Arp and S. G. Mason. *Colloid Interface Sci.*, 61:44, 1977.

[40] E. Brown and H. M. Jaeger. *J. Rheol.*, 56:875, 2012.

[41] Nicolas Fernandez, Roman Mani, David Rinaldi, Dirk Kadau, Martin Mosquet, Hélène Lombois-Burger, Juliette Cayer-Barrioz, Hans J Herrmann, Nicholas D Spencer, and Lucio Isa. *Phys. Rev. Lett.*, 111:108301, 2013.

[42] R. Seto, R. Mari, J. F. Morris, and M. M. Denn. *Phys. Rev. Lett.*, 111:218301, 2013.

[43] C. Heussinger. *Phys. Rev. E*, 88:050201, 2013.

[44] L. Isa, R. Besseling, A. N. Morozov, and W. C. K. Poon. *Phys. Rev. Lett.*, 102: 058302, 2009.

[45] A. I. Campbell and M. D. Haw. *Soft Matter*, 6:4688, 2010.

[46] A. Malevanets and R. Kapral. *J. Chem. Phys.*, 110:8605, 1999.

[47] A. Malevanets and R. Kapral. *J. Chem. Phys.*, 112:7260, 2000.

[48] J. T. Padding and W. J. Briels. *J. Chem. Phys.*, 132:054511, 2010.

[49] J. T. Padding and A. A. Louis. *Phys. Rev. E*, 74:031402, 2006.

[50] M. T. Downton and H. Stark. *J. Phys. Condens. Mat.*, 21:204101, 2009.

[51] G. Gompper, T. Ihle, D. M. Kroll, and R. G. Winkler. *Springer*, 2008.

[52] R. Kapral. *Adv. Chem. Phys.*, 140:89, 2008.

[53] A. Zöttl and H. Stark. *Phys. Rev. Lett.*, 112:118101, 2014.

[54] D. Alizadehrad, T. Krüger, M. Engstler, and H. Stark. *PLoS. Comput. Biol.*, 11: e1003967, 2015.

[55] S. P. Singh, C. Huang, E. Westphal, G. Gompper, and R. G. Winkler. *J. Chem. Phys.*, 14:084901, 2014.

[56] M. Peltomäki and G. Gompper. *Soft Matter*, 9:8346, 2013.

[57] R. J. Phillips, R. C. Armstrong, R. A. Brown, A. L. Graham, and J. R. Abbott. *Phys. Fluids A*, 4:30, 1992.

[58] D. Semwogerere and E. R. Weeks. *Phys. Fluids*, 20:043306, 2008.

[59] S. Luding. *Granular Matter*, 10:235, 2008.

[60] M. Faraday. *Philosophical Transactions of the Royal Society of London*, 147:145, 1857.

[61] A. Einstein. *Annalen der Physik*, 322:549, 1905.

[62] G. G. Stokes. *On the effect of the internal friction of fluids on the motion of pendulums*, volume 9. Pitt Press, 1851.

[63] L. M. Hocking. *J. Eng. Math.*, 7.3:207, 1973.

[64] D. Leighton and A. Acrivos. *J. Fluid Mech.*, 181:415, 1987.

[65] F. R. D. Cunha and E. J. Hinch. *J. Fluid Mech.*, 309:211, 1996.

[66] G. Plantard, H. Saadaoui, P. Snabre, and B. Poulingy. *EPL*, 75:335, 2006.

[67] D. J. Pine, J. P. Gollub, J. F. Brady, and A. M. Leshansky. *Nature*, 438:997, 2005.

[68] D. Steinhauser, S. Köster, and T. Pfohl. *ACS Macro Lett.*, 1:541, 2012.

[69] R. Chelakkot, R. G. Winkler, and G. Gompper. *Europhys. Lett.*, 91:14001, 2010.

[70] S. Reddig and H. Stark. *J. Chem. Phys.*, 135:165101, 2011.

[71] A. M. Slowicka, E. Wajnryb, and M. L. Ekiel-Jezewska. *Eur. Phys. J. E*, 36:31, 2013.

[72] O. B. Usta, D. Perchak, A. Clarke, J. M. Yeomans, and A. C. Balazs. *J. Chem. Phys.*, 130:234905, 2009.

[73] K. Sadlej, E. Wajnryb, and M. L. Ekiel-Jezewska. *J. Chem. Phys.*, 133:054901, 2010.

[74] J. L. M. Poiseuille. *Ann. Sci. Nat.*, 5:111, 1836.

[75] H. Noguchi and G. Gompper. *Proc. Natl. Acad. Sci. U.S.A.*, 102:14159, 2005.

[76] G. Danker, P. Vlahovska, and C. Misbah. *Phys. Rev. Lett.*, 102:148102, 2009.

[77] G. P. Krishnan, S. Beimfohr, and D. T. Leighton. *J. Fluid Mech.*, 321:371, 1996.

[78] Y. Ding and D. Wen. *Powder Technol.*, 149:84, 2005.

[79] P. R. Nott and J. F. Brady. *J. Fluid Mech.*, 275:157, 1994.

[80] J. F. Morris and F. Boulay. *J. Rheol.*, 43:1213, 1999.

[81] R. M. Miller and J. F. Morris. *J. Non-Newtonian Fluid Mech.*, 135:149, 2006.

[82] P. R. Nott, E. Guazzelli, and O. Pouliquen. *Phys. Fluids*, 23:043304, 2011.

[83] D. Lhuillier. *Phys. Fluids*, 21:023302, 2009.

[84] D. M. Husband, L. A. Mondy, E. Ganani, and A. L. Graham. *Rheol. Acta*, 33: 185, 1994.

[85] R. Pesche, G. Bossis, and A. Meunier. *II Nuovo Cimento*, 20:2013, 1998.

[86] M. K. Lyon and L. G. Leal. *J. Fluid Mech.*, 363:57, 1998.

[87] A. Shauly, A. Wachs, and A. Nir. *J. Rheol.*, 42:1329, 1998.

[88] H. M. Vollebregt, R. G. M. van der Sman, and R. M. Boom. *Faraday Discuss*, 158:89, 2012.

[89] Y. Zhao and R. H. Davis. *Chem. Eng. Sci.*, 57:1997, 2002.

[90] J. J. Stickel and R. L. Powell. *Annu. Rev. Fluid Mech.*, 37:129, 2005.

[91] N. J. Wagner and J. F. Brady. *Phys. Today*, 62:27, 2009.

[92] J. M. Brader. *J. Phys.: Condens. Matter*, 22:363101, 2010.

[93] H. A. Barnes. *J. Rheol.*, 33:329, 1989.

[94] J. Bender and N. J. Wagner. *J. Rheol.*, 40:899, 1996.

[95] C. L. M. H. Navier. *M.* Acad. Sci. Inst. France, 6:389, 1822.

[96] L. D. Landau and E. M. Lifshitz. *Course of Theoretical Physics, Vol. 6. Fluid Mechanics.* London, Pergammon, 2nd ed., 1997.

[97] J. Happel and H. Brenner. *Low Reynolds Number Hydrodynamics.* Kluwer, Dordrecht, 1983.

[98] A. T. Chwang and T. Wu. *J. Fluid Mech.*, 67:787, 1975.

[99] J. K. G. Dohnt. *An Introduction to Dynamics of Colloids.* Elsevier, 1996.

[100] D. L. Morris, L. Hannon, and A. L. Garcia. *Phys. Rev. E*, 46:5279, 1992.

[101] M. A. Day. *Erkenntnis*, 33:285, 1990.

[102] T. M. Squires and S. R. Quake. *Rev. Mod. Phys.*, 77:977, 2005.

[103] G. M. Whitesides. *Nature*, 442:368, 2006.

[104] H. Lamb. *Hydrodynamics.* Cambridge Mathematical Library, 1993.

[105] H. Lamb. *Hydrodynamics.* New York: Dover Publications, 1945.

[106] M. Van Dyke. *Perturbation Methods in Fluid Mechanics.* Parabolic Press, 1975.

[107] C. W. Oseen. *Über die Stokes'sche Formel, und über eine verwandte Aufgabe in der Hydrodynamik.* Arkiv för matematik, astronomi och fysik, 1910.

[108] L. D. Landau and E. M. Lifshitz. *Hydrodynamik, Lehrbuch der theoretischen Physik.* Akademie Verlag, 1991.

[109] A. T. Chwang and T. Wu. *J. Fluid Mech.*, 63:607, 1974.

[110] M. Von Smoluchowski. *Annalen der Physik*, 326:756, 1906.

[111] C. W. Gardiner. *Handbook of Stochastic Methods.* Springer, 1985.

[112] L. D. Landau and E. M. Lifshitz. *Statistical Physics, Part 1.* Pergamon Press, 1980.

[113] H. Nyquist. *Phys. Rev.*, 32:110, 1928.

[114] H. B. Callen and T. A. Welton. *Phys. Rev.*, 83:34, 1951.

[115] R. Kubo. *Rep. Prog. Phys.*, 29:255, 1966.

[116] H. Risken. *The Fokker-Planck Equation: Methods of Solution and Application.* Springer, 1996.

[117] W. Demtröder. *Experimentalphysik I.* Springer, 2006.

[118] U. M. Ascher and L. R. Petzold. *Computer Methods for Ordinary Differential Equations and Differential-Algebraic Equations.* Philadelphia: Society for Industrial and Applied Mathematics, 1998.

[119] S. H. Strogatz. *Nonlinear dynamics and chaos.* Addison-Wesley Publishing Company, 1994.

[120] I. Bendixson. *Sur les courbes définies par des équations différentielles.* Acta Mathematica, Springer Netherlands, 1901.

[121] G. D. Smith. *Numerical solution of partial differential equations: finite difference methods.* Oxford University Press, 1985.

[122] O. C. Zienkiewicz, R. L. Taylor, and J. Z. Zhu. *The Finite Element Method: Its Basis and Fundamentals.* Butterworth-Heinemann, 2005.

[123] J. N. Reddy. *An Introduction to the Finite Element Method.* McGraw-Hill, 2006.

[124] J. S. Liu. *Monte Carlo Strategies in Scientific Computing.* Springer Series in Statistics, 2001.

[125] M. E. J. Newman and G. T. Barkema. *Monte Carlo Methods in Statistical Physics*. Oxford University Press, 1999.

[126] D. Wolf-Gladrow. *Lattice-Gas Cellular Automata and Lattice Boltzmann Models*. Springer Verlag, 2000.

[127] H. Huang, M. C. Sukop, and X. Y. Lu. *Multiphase Lattice Boltzmann Methods: Theory and Application*. Wiley-Blackwell, 2015.

[128] K. Schaar, A. Zöttl, and H. Stark. *Phys. Rev. Lett.*, 115:038101, 2015.

[129] M. Peltomäki and G. Gompper. *Soft Matter*, 9:8346, 2013.

[130] K. Schaar, A. Zöttl, and H. Stark. *Phys. Rev. Lett.*, 115:038101, 2015.

[131] D. Alizadehrad, T. Krüger, M. Engstler, and H. Stark. *PLoS Comput. Biol.*, 11: e1003967, 2015.

[132] C. K. Hemelrijk, D. A. P. Reid, H. Hildenbrandt, and J. T. Padding. *Fish and Fisheries*, 16.3:511, 2015.

[133] W. C. Swope, H. C. Andersen, P. H. Berens, and K. R. Wilson. *J. Chem. Phys.*, 76:637, 1982.

[134] N. S. Martys and R. D. Mountain. *Phys. Rev. E*, 59:3733, 1999.

[135] C. J. Horowitz, M. A. Perez-Garcia, J. Carriere, D. K. Berry, and J. Piekarewicz. *Phys. Rev. C*, 70:065806, 2004.

[136] E. Allahyarov and G. Gompper. *Phys. Rev. E*, 66:036702, 2002.

[137] N. Noguchi, N. Kikuchi, and G. Gompper. *Europhys. Lett.*, 78:10005, 2007.

[138] T. Ihle, E. Tüzel, and D. M. Kroll. *Europhys. Lett.*, 73:664, 2006.

[139] E. Tüzel, T. Ihle, and D. M. Kroll. *Math. Comput. Simulat.*, 72:232, 2006.

[140] G. Marsaglia and W. W. Wai Wan Tsang. *J. Stat. Softw.*, 4:8, 2000.

[141] J. F. Ryder. *Mesoscopic Simulations of Complex Fluids*. PhD thesis, University of Oxford, 2005.

[142] T. Ihle and D. M. Kroll. *Phys. Rev. E*, 63:020201, 2001.

[143] T. Ihle and D. M. Kroll. *Phys. Rev. E*, 67:066705, 2003.

[144] I. O. Göthe, H. Noguchi, and G. Gompper. *Phys. Rev. E*, 76:046705, 2007.

[145] N. Noguchi and G. Gompper. *Phys. Rev. E*, 78:016706, 2008.

[146] A. Lamura, G. Gompper, T. Ihle, and D. M. Kroll. *Europhys. Lett.*, 56:319, 2001.

[147] J. T. Padding, A. Wysocki, H. Löwen, and A. A. Louis. *J. Phys. Condens. Matter*, 17:S3393, 2005.

[148] L. Verlet. *Phys. Rev.*, 159:98, 1967.

[149] I. O. Götze and G. Gompper. *Phys. Rev. E*, 82:041921, 2010.

[150] A. Donev, S. Torquato, and F. H. Stillinger. *J. Comput. Phys.*, 202:737, 2005.

[151] P. A. Cundall and O. D. L. Strack. *Geotechnique*, 29:47, 1979.

[152] G. Gompper, T. Ihle, D. M. Kroll, and R. G. Winkler. *Poly. Sci.*, 221:1, 2009.

[153] E. Guyon, J. P. Hulin, L. Petit, and C. D. Mitescu. *Physical Hydrodynamics*. Oxford University Press, Oxford, 2001.

[154] M. Ripoll, K. Mussawisade, R. G. Winkler, and G. Gompper. *Phys. Rev. E*, 72: 016701, 2005.

[155] L. Dagum and R. Menon. *IEEE Comput. Sci. Eng.*, 5:46, 1998.

[156] R. Chandra. *Parallel programming in OpenMP*. Morgan Kaufmann, 2001.

[157] D. J. Tildesley and M. P. Allen. *Computer Simulation of Liquids*. Clarendon, Oxford, 1987.

[158] V. A. Epanechnikov. *Theor. Probab. Appl.*, 14:153, 1969.

[159] S. Reddig and H. Stark. *J. Chem. Phys.*, 138(23):234902, 2013.

[160] E. Falck, J. M. Lahtinen, I. Vattulainen, and T. Ala-Nissila. *Eur. Phys. J. E*, 13: 267, 2004.

[161] O. Annunziata. *J. Phys. Chem. B*, 112:11968, 2008.

[162] A. Vergara, L. Paduano, V. Vitagliano, and R. Sartorio. *J. Phys. Chem. B*, 104: 8068, 2000.

[163] W. B. Russel and A. B. Glendinning. *J. Chem. Phys.*, 72:948, 1981.

[164] P. N. Segré, O.P. Behrend, and P. N. Pusey. *Phys. Rev. E*, 52:5070, 1995.

[165] T. Boublík. *Molec. Phys.*, 29:421, 1975.

[166] N. W. Ashcroft and D. C. Langreth. *Phys. Rev.*, 156:685, 1967.

[167] D. B. Genovese. *Adv. Colloid Interface Sci.*, 171:1, 2012.

[168] I. M. Krieger and T. J. Dougherty. *Trans. Soc. Rheol.*, 3:137, 1959.

[169] J. G. Berryman. *Phys. Rev. A*, 27:1053, 1983.

[170] G. D. Scott and D. M. Kilgour. *J. Appl. Phys.*, 2:863, 1969.

[171] S. Kaplun. *J. Math. Mech.*, 6:595, 1957.

[172] S. Sanyal, N. Easwar, S. Ramaswamy, and A. K. Sood. *Europhys. Lett.*, 18:107, 1992.

[173] Y. Fan. *Shear-induced segregation in dense granular mixtures*. PhD thesis, University of Minnesota, 2011.

[174] Y. Fan and K. M. Hill. *Phys. Rev. Lett.*, 106:218301, 2011.

[175] J. G. Berryman. *Phys. Rev. A*, 27:1053, 1983.

[176] K. W. Desmond and E. R. Weeks. *Phys. Rev. E*, 80:051305, 2009.

[177] Q. Du, V. Faber, and M. Gunzburger. *SIAM Review*, 41:637, 1999.

[178] B. D. Lubachevsky, F. H. Stillinger, and E. N. Pinson. *J. Stat. Phys.*, 64:501, 1991.

[179] L. Isa. *Capillary flow of dense colloidal suspensions.* PhD thesis, University of Edinburgh, 2007.

[180] H. J. Payne. *Transport. Res. Rec.*, 722:68, 1979.

[181] B. S. Kerner and P. Konhauser. *Phy. Rev. E*, 48:R2355, 1993.

[182] B. S. Kerner and P. Konhauser. *Phy. Rev. E*, 50:54, 1994.

[183] J. A. Lewis. *Curr. Opin. Solid State Mater. Sci.*, 6:245, 2002.

[184] I. Zuriguel, D. R. Parisi, R. C. Hidalgo, C. Lozano, A. Janda, P. A. Gago, and D. Maza. *Sci. Rep.*, 4, 2014.